DEFLECTION AND VIBRATION LIMITS FOR

SIMPLY SUPPORTED STEEL BRIDGES

By

SHAKIRA SHELLY BYRD

A thesis submitted to the

Graduate School – New Brunswick

Rutgers, The State University of New Jersey

in partial fulfillment of the requirements

for the degree of

Masters of Science

Graduate Program in Civil and Environmental Engineering

written under the direction of

Hani Nassif

and approved by

_____

_____

_____

New Brunswick, New Jersey

May 2020

ABSTRACT OF THE THESIS

DEFLECTION AND VIBRATION LIMITS FOR

SIMPLY SUPPORTED STEEL BRIDGES

By SHAKIRA SHELLY BYRD

Thesis Director:

Hani Nassif

Deflection and vibration significantly impact the serviceability of bridges. Deflection limits are based on subjective human responses that are not directly related to a bridge's structural integrity or vibration control. Nonetheless, deflection limits are indirectly used to limit bridge vibrations. Over the years, significant changes have occurred in the field of bridge design and construction. Today's bridges are designed with longer spans, stronger materials, and lighter decks, which impact how the bridges respond under different live loads. Five existing bridges will be used to investigate the relationship between deflection and vibration. Each bridge will be modeled using the grillage method and remodeled with adjustments made to the thickness of the deck, concrete density of the deck, and girder size. Lastly, the vibration parameters of the existing bridges and the modified bridges will be compared with current design limits and criteria.

ACKNOWLEDGMENTS

I would like to thank Dr. Hani Nassif, my thesis advisor, for his guidance and support throughout my graduate career at Rutgers University. I would also like to thank all my professors, friends, family, and boyfriend Aaron, for their patience and support while completing my graduate studies.

TABLE OF CONTENTS

ABSTRACT OF THE THESIS ii

ACKNOWLEDGMENTS iii

TABLE OF CONTENTS iv

LIST OF FIGURES viii

LIST OF TABLES xi

CHAPTER 1. INTRODUCTION 1

1.1 Problem Statement 1

1.2 Scope 2

1.3 Organization 3

CHAPTER 2. LITERATURE REVIEW 4

2.1 History of Deflection Limits 4

2.2 Human Response to Vibration 5

2.3 Deflection and Vibration Codes for Bridges 13

2.3.1 AASHTO LRFD and Korean Code 13

2.3.2 Canadian Standards 13

2.3.3 Australian Codes 14

2.3.4 European Codes 14

2.3.5 British Standards 14

CHAPTER 3. GRILLAGE ANALYSIS METHOD 16
3.1 Slab-on-Girder Bridge 16
3.1.1 Longitudinal Elements 17
3.1.2 Transverse Elements 19
3.1.3 Stiffness Matrix 19
3.1.4 Mass Matrix 20
3.1.5 Transformation Matrix 21
3.1.6 Damping Matrix 22
3.1.7 Equivalent Nodal Loads 23
3.1.8 Dynamic Equations 26
3.1.9 Strains and Displacements 26
3.2 Road Roughness Input 28
3.2.1 Generation of Single Road Roughness Profile 28
3.2.2 Generation of Two Correlated Road Roughness Profiles 31
3.2.3 Measurement of Road Roughness Profiles 35
3.3 Vehicle Model 36
3.3.1 Dynamic Properties of Vehicle Components 36
3.3.2 Dynamic Equations of Motion for Vehicle Model 39
3.4 Computer Simulation Program 44
3.4.1 Algorithm 44

3.4.2 Newmark-β method 45

Chapter 4 Model Validation 53

4.1 Introduction 53

4.2 Bridge Site 53

4.3 Data Collection 53

4.3.1 I-287 Plan View Sketches 55

4.3.2 I-287 Senor Details 56

4.4 Testing Vehicle 60

4.5 Diagnostic Testing 60

4.6 Girder Cross-Sectional Properties (Plans) 65

4.7 I-287 Bridge Model 67

4.8 Model Assumptions/Idealizations 68

4.9 Dynamic Model Validation 69

Chapter 5: Parametric Study 71

5.1 Bridges 71

5.1.1 Roadway Data 71

5.1.2 Deflection and Vibration Data 72

5.1.3 Elevation Photos 73

5.1.4 Deck Cross Section Sketches 74

5.1.5 Grillage Models 75

5.2 Test Vehicle 76

5.3 Deck Thickness Data 77

5.4 Concrete Deck Density Data 80

5.5 Girder Size Data 83

CHAPTER 6. CONCLUSIONS AND RECOMMENDATIONS 88

6.1 Summary 88

6.2 Conclusions 89

6.3 Recommendations 89

REFERENCES 90

LIST OF FIGURES

Figure 2.1: The Six Human Tolerance Levels 6

Figure 2.2: Tolerance Levels of Human Reaction to Vibration Amplitude vs. Frequency 7

Figure 2.3: Vertical Vibration Limits for Automobile Passenger Comfort 8

Figure 2.4: Contours of Equal Sensitivity to Vibration 9

Figure 2.5: Human response to Flexibility of Girders 11

Figure 2.6: Maximum Magnitudes of Vertical Accelerations of Bridges 12

Figure 2.7: First Flexural Frequency versus Static Deflection 13

Figure 2.8: First Flexural Frequency versus Static Deflection 14

Figure 2.9: Comparison of Canadian Standards, Australian Code, Wright-Walker Criteria and AASHTO Deflection Limit 15

Figure 3.1: Grillage System for Slab-on-Girder Bridge 48

Figure 3.2: Cross Sectional Properties of Grillage Member 48

Figure 3.3 Local and Global Coordinate System 48

Figure 3.4 Wheel Load Transformation 49

Figure 3.5: Randomly Generated Single Road Roughness Profile 49

Figure 3.6: Road Parameters on an Isotopic Surface 49

Figure 3.7: Truck Mass Distribution 50

Figure 3.8: 3-D Vehicle Model 51

Figure 3.9: Free Cody Diagram of Vehicle Model 51

Figure 4.1: Bridge Plan View 55

Figure 4.2: Installation Plan of Long-Term and Short-Term Sensor 55

Figure 4.3: Detail 1- Location of Long-Term Tilt Meter near Support 56

Figure 4.4: Detail 2- Location of Strain Transducer at 1/4 Span and 3/4 Span 57

Figure 4.5.: Detail 3- Short-Term and Long-Term Sensors at Midspan 58

Figure 4.6: Detail 4-Short-Term Sensors at Midspan 58

Figure 4.7: Sensor Installation and Setup 59

Figure 4.8: I-287 Test Truck 60

Figure 4.9: Diagnostic Load Testing Plan 60

Figure 4.10: Typical Strain Data Results for Sagging Girder 61

Figure 4.11: Typical Strain Data Results for Sagging Girder (B8) 62

Figure 4.12: Typical deflection data from LDV 62

Figure 4.13: Field Photos 64

Figure 4.14: Original Girders (B8-B14) Cross-Sectional Properties 65

Figure 4.15: Widening Stringers (S3 & S4) Cross-Sectional Properties 66

Figure 4.16: I-287 Grillage Output Grid 67

Figure 4.17: I-287 Grillage Grid Properties 67

Figure 4.18: Experimental Strain vs. Grillage Model Strain 69

Figure 4.19: I-287 Grillage Calibrated Results 70

Figure 5.1: Bridge Elevation Views 73

Figure 5.2: Deck Cross Section Sketches 74

Figure 5.3: Grillage Gird Models 75

Figure 5.4: Grillage Test Vehicle (HS20) 76

Figure 5.5: Deck Thickness vs. Max Deflection 78

Figure 5.6: Deck Thickness vs. Absolute Max Acceleration 79

Figure 5.7: Deck Thickness: Deflection vs. Acceleration 79

Figure 5.8: Concrete Deck Density vs. Max Deflection 81

Figure 5.9: Concrete Deck Density vs. Absolute Max Acceleration 82

Figure 5.10: Concrete Deck Density: Deflection vs. Acceleration 82

Figure 5.11: Girder Size vs. Max Deflection 85

Figure 5.12: Girder Size vs. Absolute Max Acceleration 85

Figure 5.13: Span-to-Depth Ratio vs. Max Deflection 86

Figure 5.14: Span-to-Depth Ratio vs. Absolute Max Acceleration 86

Figure 5.15: Girder Size: Deflection vs. Acceleration 87

LIST OF TABLES

Table 2.1: Historic Depth-to-Span Ratios 4

Table 2.2: Peak Acceleration for Human Response to Harmonic Vertical Vibration 9

Table 4.1: Identification of Sensors 54

Table 4.2: Field Notes from Path 1 to Path 3 61

Table 4.3: Results Comparison between Long-Term and Short-Term Strain Sensors 63

Table 5.1: Roadway Data of Bridges 71

Table 5.2: Perceived Deflection and Vibration Data 72

Table 5.3: Deck Thickness (Deflection) Summary 77

Table 5.4: Deck Thickness (Acceleration) Summary 77

Table 5.5: Deck Thickness Average Change Summary 78

Table 5.6: Concrete Deck Density (Deflection) Summary 80

Table 5.7: Concrete Deck Density (Acceleration) Summary 80

Table 5.8: Concrete Deck Density Average Change Summary 81

Table 5.9: Girder Size (Deflection) Summary 83

Table 5.10: Girder Size (Acceleration) Summary 84

Table 5.11: Girder Size Average Change Summary 84

Table 5.12: Girder Size: Span-to-Depth Ratios 84

CHAPTER 1. INTRODUCTION

1.1 Problem Statement

AASHTO recommended the deflection limit L/800 in the 1930s when the Bureau of Public Roads conducted a survey on multiple bridges presumed to have vibrations issues based on subjective human responses (Baker, 1958). AASHTO's deflection limit is based on an irrational railroad specification from the early 1900s used to prevent railcars from derailing under excessive vibrations. Nevertheless, these deflection limits are indirectly used to limit highway bridge vibrations. Currently, multiple state DOTs have proposed deflection limits between L/1600 and L/800 (Roeder, et al, 2004).

Bridge engineers need consistent and reliable specifications to design bridges that are safe, durable, and serviceable. Limiting vibration parameters such as displacement, velocity, acceleration, and frequency can help ensure user comfort. Many regulations have been proposed to help limit human sensitivities to bridge vibrations. Deflection limits are often used to limit vibration because the calculations are easier and more convenient than other parameters.

However, many studies show that humans are more sensitive to acceleration than deflection (Gaunt, 1981). Deflection limits alone are not enough to limit bridge vibrations and ensure human comfort (Wright and Walker, 1971). In 2002, Roeder completed a comprehensive study on live load deflection that concluded that deflection limits do not ensure vibration control; some of the bridges satisfied deflection limits and had poor vibration control, while some of the bridges violated the deflection limit and had good vibration control. In 2007, Wei and Chen

examined concrete-filled tubular arch bridges and found that deflection limits do not limit the perceived vibrations felt by pedestrians. In 2013, Baker concluded that AASHTO's criteria regarding serviceability might not be insufficient in controlling bridge vibrations that impact user comfort.

Limiting a bridge's deflection does not guarantee unpleasant vibrations will not impact users. There needs to be an established criterion that directly controls vibration instead of indirectly using deflections limits.

1.2 Scope

This thesis will investigate the relationship between deflection and acceleration limits. Existing simply supported slab-on-girder bridges will be investigated. Measured field data from one of the bridges will be used to calibrate the bridge-road-vehicle model used in the grillage analysis. The grillage models will keep girder spacings, span lengths, roadway widths, road roughness profiles, and vehicle models constant. This analysis will investigate the relationship between deflection and acceleration limits upon changing the girder sizes, deck thickness, and density of the concrete deck. The girder sizes will be adjusted based on the original designs by under designing them by -10%, -20%, and -30% and then over-designing them by +10%, +20%, and +30%. The thicknesses of the deck will vary from 9 in., 10 in., 11 in., and 12 in. The density of the concrete deck will vary from 145 lbs. /ft^3, 165 lbs. /ft^3, 185 lbs. /ft^3, and 205 lbs. /ft^3. This analysis will highlight the relationship between deflection and acceleration under different conditions without interfering with the deflection limit L/800.

1.3 Organization

This study consists of six chapters as following:

Chapter 1 covers the introduction, including the problem statement, scope, and organization of the thesis.

Chapter 2 covers the literature review, focusing on the theoretical models, experimental data used in previous related studies, and code provisions.

Chapter 3 describes the 3-D grillage model and the algorithm used to describe the bridge-vehicle-road dynamic interaction system.

Chapter 4 details the sample bridges and the method used to calibrate the grillage models.

Chapter 5 covers the parametric study.

Chapter 6 provides conclusions and recommendations.

CHAPTER 2. LITERATURE REVIEW

2.1 History of Deflection Limits

Deflection limits can be traced back to 1871 with the specifications created by the Phoenix Bridge Company, which limited trains traveling 30 mph to 1/1200 of the span length. (Roeder, 2002). In 1905, the American Railway Engineering Association (A.R.E.A) specifications limited span-to-depth ratios to prevent trains from derailing under extreme vibrations. The A.R.E.A limited pony trusses and plate girders to 1/10, and rolled girders and channels to 1/12 to indirectly control vertical vibrations and acceleration. In 1924, A.A.S.H.O (now AASHTO) adopted span-to-depth ratios similar to the A.R.E.A (See Table 2.1).

Association	Year	Trusses	Plate Girders	Rolled Girders
A.R.E.A	1905	1/10	1/10	1/20
	1907	1/10	1/12	1/12
	1919	1/10	1/12	1/15
A.A.S.H.O	1913	1/10	1/12	1/20
	1931	1/10	1/15	1/20
	1935	1/10	1/25	1/25

Table 2.1: Historic Depth-to-Span Ratios

(ASCE, 1958)

In 1930, the Bureau of Public Roads conducted a study with human subjects and found deflections exceeding L/800 created vibrations perceived as unacceptable. Subsequently, in

1936, the live load deflection limit L/800 was adopted. In 1939, the deflection limit L/300 was proposed for overhangs, and in 1960, the deflection limit L/1000 was adopted for pedestrian bridges. The L/1000 limit for pedestrian bridges was established after a wealthy woman complained that a bridge's vibrations awoken her sleeping baby. This complaint sparked immediate action from the state to limit the deflection limits even more for pedestrian bridges (Roeder, 2002).

Bridge deflection limits were put in place to ensure human comfort. However, these deflection limits are exclusively based on subjective human perceptions instead of empirical data. The bridge industry has undergone significant changes with materials that are more robust, better construction methods, superior analysis methods, and different live loading. Even so, defection limits have not changed, and bridge engineers still use these outdated limits to limit bridge vibrations indirectly.

2.2 Human Response to Vibration

Human perception is complicated and cannot be quantified by a single parameter. Human responses to vibrations are both psychological and physiological (Gaunt, 1981). In 1902 Mallock, investigated complaints of unpleasant vibration and discovered that acceleration was the leading cause of user discomfort. In 1931, Reiher and Meister investigated the relationship between human sensitivity and vibration. Reiher and Meister subjected human subjects to sinusoidal movement in the vertical and horizontal direction for about ten minutes. From this study, six human perception categories were created: (1) imperceptible, (2) slightly perceptible, (3) distinctly perceptible, (4) strongly perceptible, (5) unpleasant, and very (6) disturbing (See Figure 2.1).

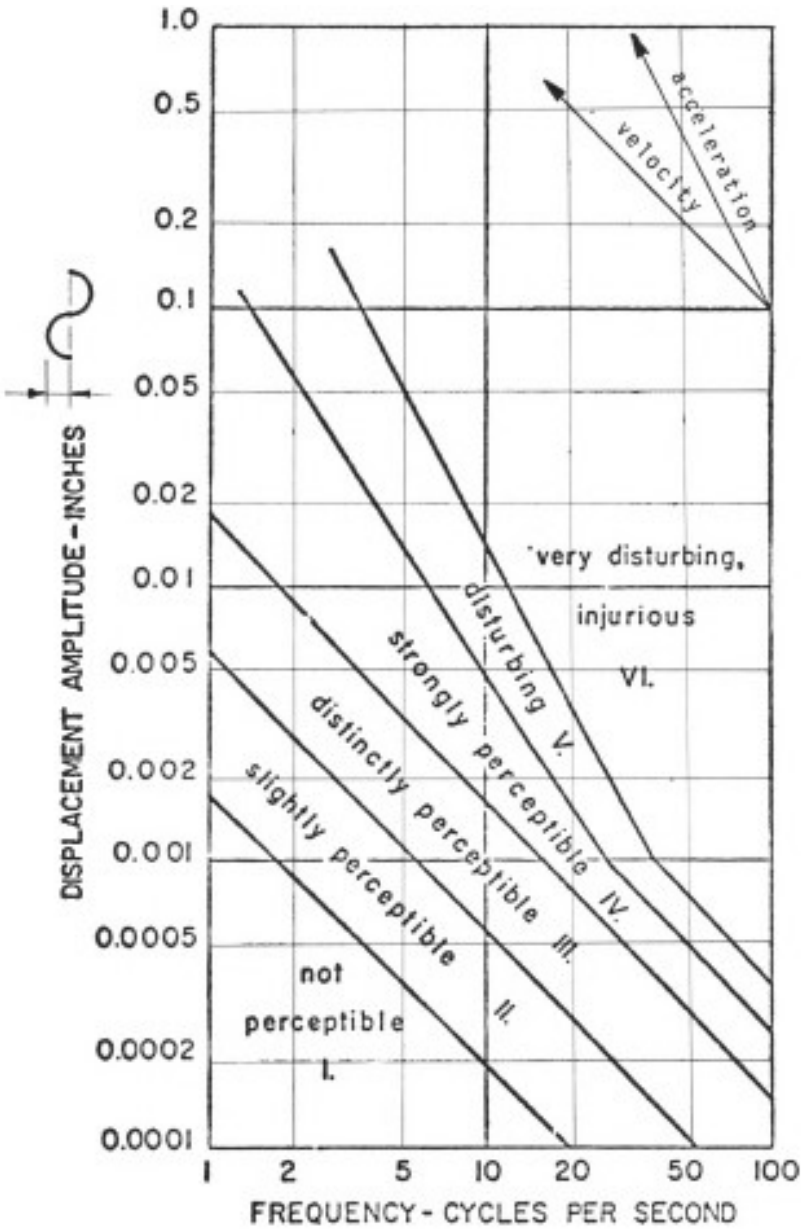

Figure 2.1: The Six Human Tolerance Levels

(Reiher and Meister, 1931)

In 1948, Goldman analyzed several different studies and surmised the data into three tolerance curves relating amplitude and frequency: perceptible, unpleasant, and intolerable (See Figure 2.2).

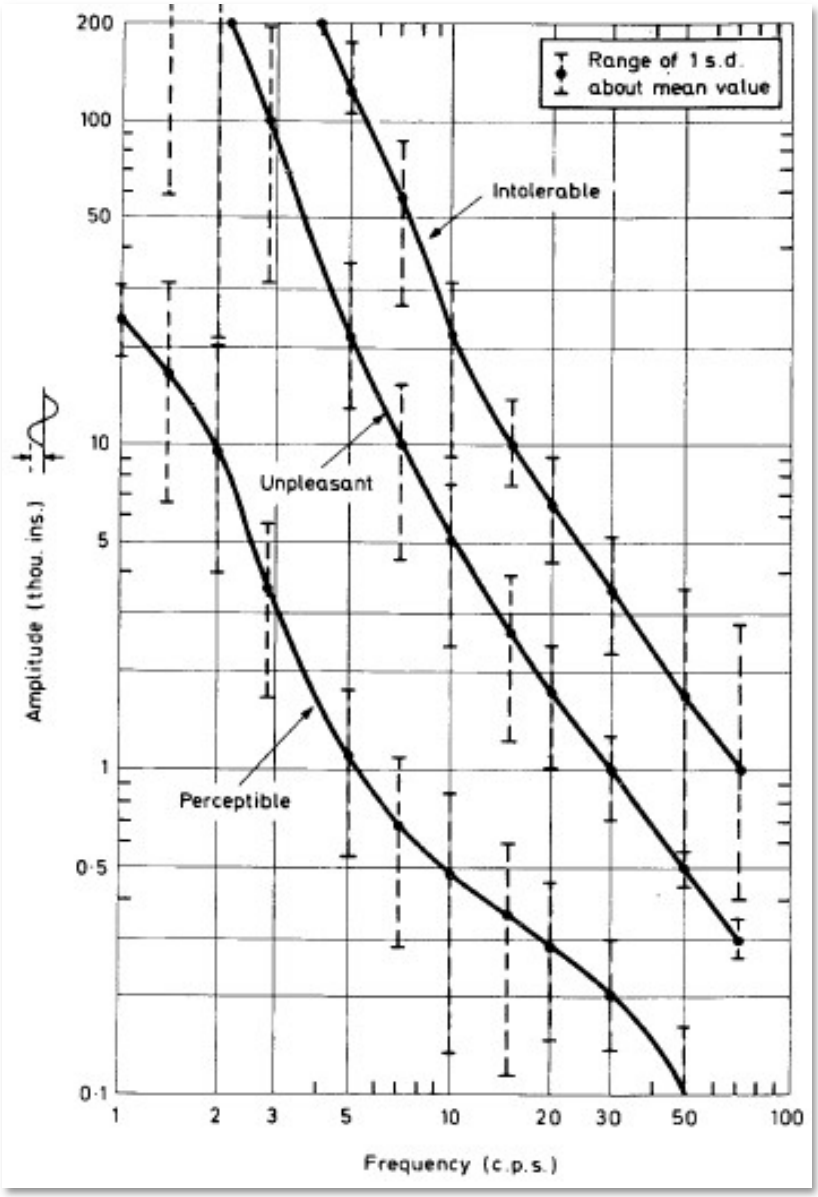

Figure 2.2: Tolerance Levels of Human Reaction to Vibration Amplitude vs. Frequency (Goldman, 1948)

Furthermore, he set the minimum acceleration for perceptible vibrations at 0.0025g and the minimum acceleration for human discomfort at 0.046g. In the same year, Janeway constructed a similar graph based on the riding comfort of users in vehicles (See Figure 2.3).

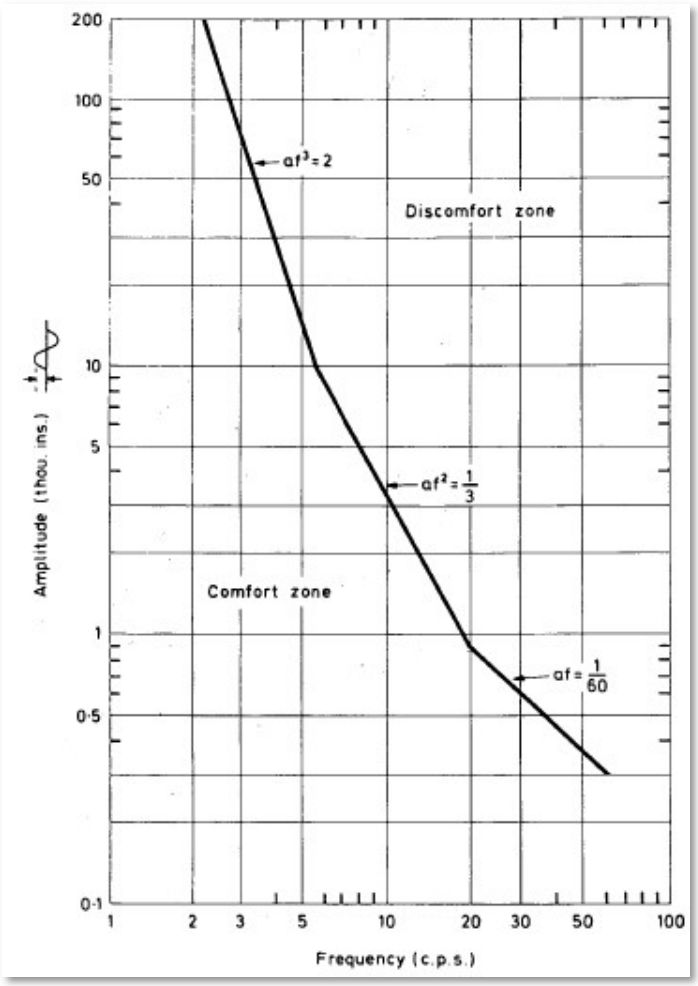

Figure 2.3: Vertical Vibration Limits for Automobile Passenger Comfort

(Janeway, 1948)

In 1957 Oehler, tested fifteen bridges of three types: simply supported, continuous, and cantilever. From his findings, it was concluded that cantilever bridges are most susceptible to vibration and that bridges with lower fundamental frequency are more susceptible to vibrations. In 1964, Wright and Green investigated fifty-two highway bridges and graphed their data using the Reiher and Meister scale, which was later adopted by the Canadian code (See Figure 2.4).

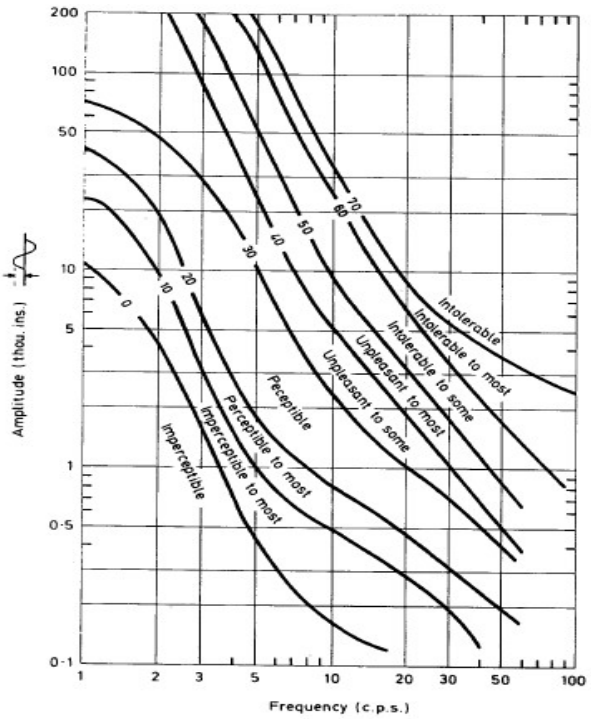

Figure 2.4: Contours of Equal Sensitivity to Vibration

(Wright and Green, 1964)

In 1971, Wright and Walker proposed an acceleration limit of 100 in/s^2 (See Table 2.2).

Human Response	Peak Acceleration, 100 in/s^2	
	Transient	Sustained
Imperceptible	5	0.5
Perceptible to Some	10	1
Perceptible to Most	20	2
Perceptible	50	5
Unpleasant to Few	100	10
Unpleasant to Some	200	20
Unpleasant to Most	500	50
Intolerable to Some	1000	100
Intolerable to Most	2000	200

Table 2.2: Peak Acceleration for Human Response to Harmonic Vertical Vibration

(Wright and Walker, 1971)

The peak transient peak vibration can be calculated from the following equations:

$$\delta_s = 0.05 \times L \times \frac{\propto}{(V + 0.3 \times f_s \times L) \times f_s}$$

where,

δ_s = Static Deflection

α_s = Transient Peak Acceleration

L = Span Length

V = Vehicle Speed

f_s = Natural Frequency

$$f_s = \frac{\pi}{2 \times L^2} \sqrt{\frac{E_b I_b}{m}}$$

where,

$E_b I_b$ = Flexural Rigidity of Girder Section

M = Mass of Girder Section

Wright and Walker attributed human perception to vibration to peak acceleration and the dynamic component of deflection. A separate test was conducted on different span types to determine the peak acceleration values in relation to human response limits (See Figure 2.5).

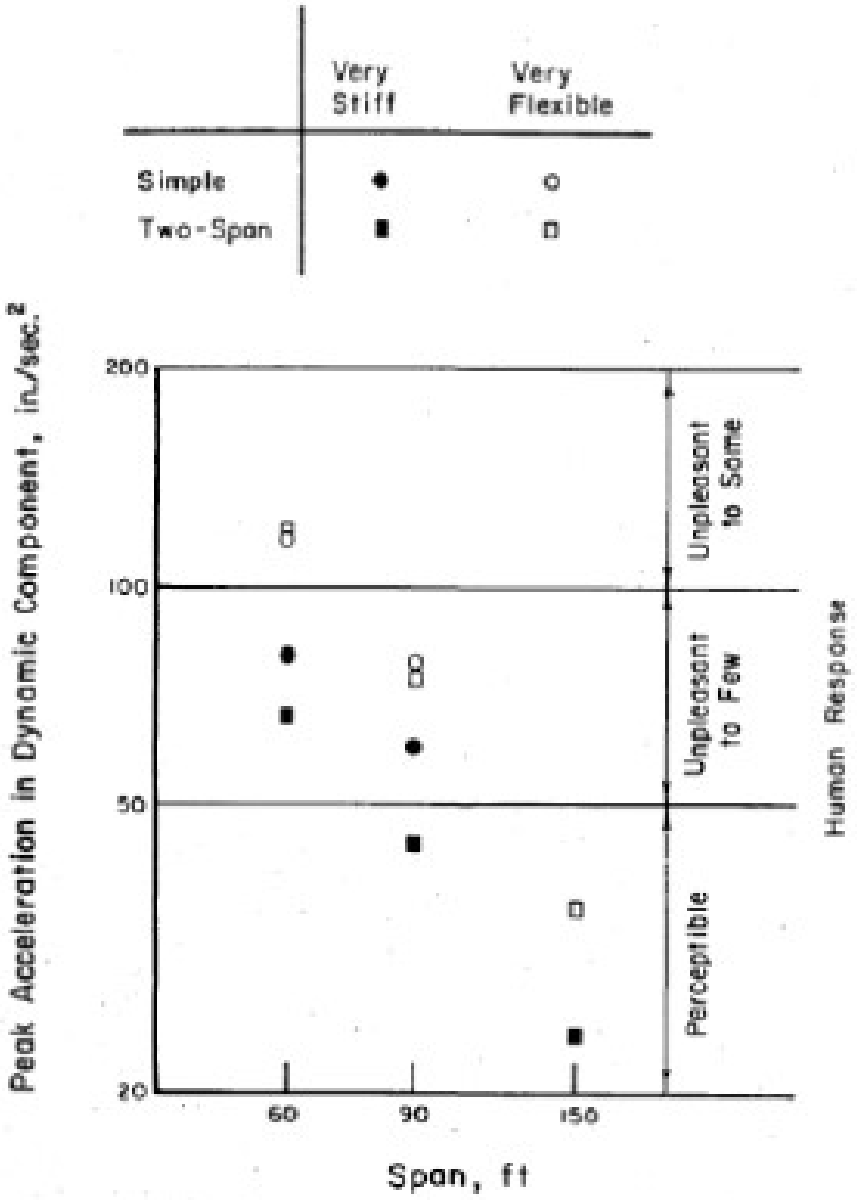

Figure 2.5: Human response to Flexibility of Girders

(Wright and Walker, 1971)

In 1977, ASSHTO revised its bridge specification based on Wright and Walker's findings, which allowed designers to exceed live load deflection limits if the maximum acceleration did not exceed 100 in/s^2. In 1978, Irwin conducted a lavatory test with human subjects to gather responses to everyday usage and storm conditions (See Figure 2.6)

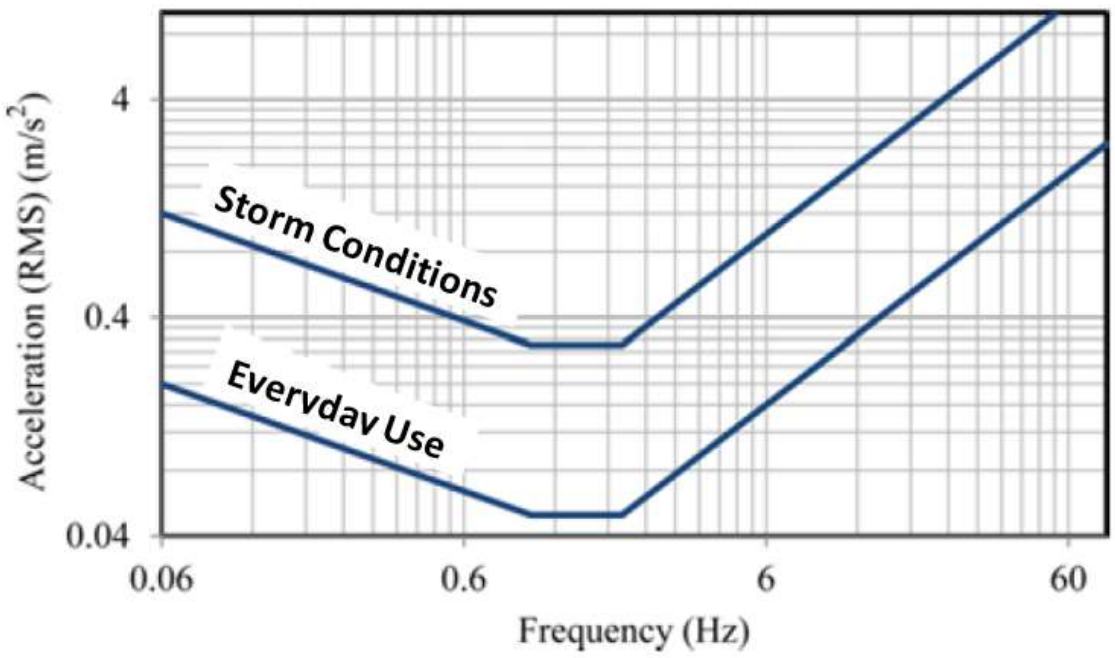

Figure 2.6: Maximum Magnitudes of Vertical Accelerations of Bridges

(Irwin, 1978)

In 1984, Billing and Green defined the following acceleration responses: slightly perceptible (0.015g ≤ 0.025g), distinctly perceptible (≥ 0.052), and strongly perceptible (≥0.076g). In 1997, the International Organization of Standards (ISO 2631-1) established six human reaction levels for public transportation ranging from “not uncomfortable” to “extremely uncomfortable” with acceleration readings between 0.315 m/s^2 to 2 m/s^2. Visibly, the human perception of vibration is very subjective and cannot be measured directly. Multiple studies have used deflection, frequency, and accelerations to quantify the human perception of vibration. However, research quantitively shows that acceleration influences the human perception of vibration the most.

2.3 Deflection and Vibration Codes for Bridges

Many counties have guidelines and regulations to control bridge vibrations based on deflection and acceleration limits.

2.3.1 AASHTO LRFD and Korean Code

In 1996, span-to-depth ratios (L/D) were added to the code ranging from 1/40 to 1/10 depending on the superstructure type and deflection limits, L/800 for vehicular bridges, and L/1000 for pedestrian bridges (AASHTO, 1996). To determine deflection limits, all lanes must be loaded. These specifications are present in the current AASHTO LRFD specification as optional limits and the Korean Code (MLTM, 2010).

2.3.2 Canadian Standards

The Canadian Standards use Wright and Green (1964) work relating natural frequency and max superstructure deflection to quantify user comfort. To compute live load deflection, one truck must be placed in the center lane with dynamic allowance and without a lane loaded factor (See Figure 2.7).

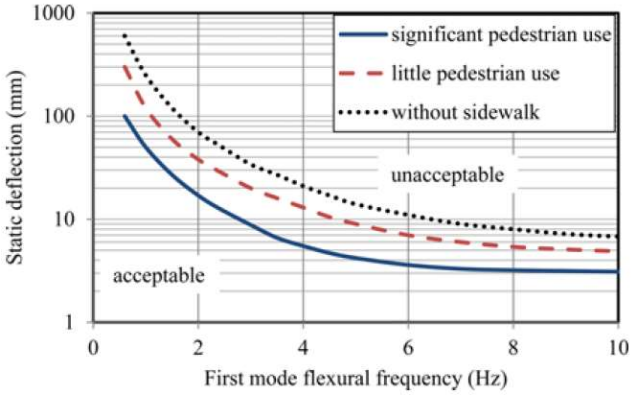

Figure 2.7: First Flexural Frequency versus Static Deflection

(Canadian Standards, 1990)

2.3.3 Australian Codes

The Australian Codes (Austroads, 1996) use the first mode flexural frequency (Hz) and static deflection (mm) to quantify human perceptibility to vibration (See Figure 2.8).

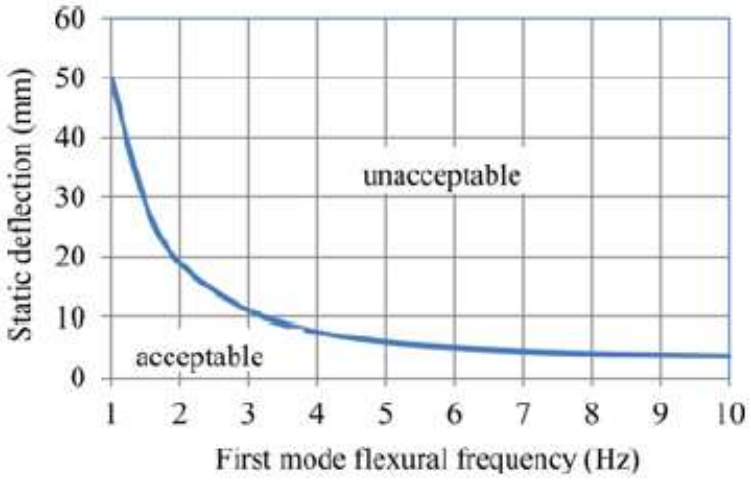

Figure 2.8: First Flexural Frequency versus Static Deflection

(Australian Codes, 1992)

2.3.4 European Codes

The European Codes do not use deflection or frequency limits to control bridge vibrations. A "vibration factor" is used when factoring live loads to account for added stresses caused by vibrations (Wu, 2003).

2.3.5 British Standards

The British Standards use natural frequency to limit the vertical acceleration of footbridges and cycle track bridges. The following equation is used (BS 5400):

$$0.5\sqrt{f_0}\ \ \frac{m}{s^2}$$

where,

$F_0 \leq$ Hz

In short, most agencies are using acceleration and frequency limits to control vibration. Meanwhile, ASSHTO LRFD is using a deflection limit based on span length only. Research shows that deflection limits are inferior to acceleration and frequency limits when controlling vibration. Nonetheless, ASSHTO's deflection limits have remained untouched due to simplicity. Hung X. Le and Eui-Seung Hwang did a comparative analysis of multiple codes (See Figure 2.9). Their analysis further suggests that frequency-based limits are more rational than span-length limits. The Wright-Walker Criteria and the Canadian Code seem most rational in satisfying human perceptions to bridge vibrations.

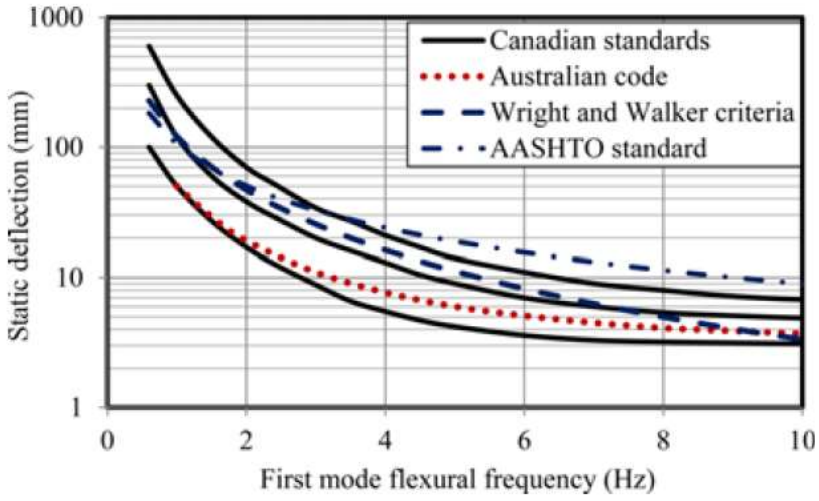

Figure 2.9: Comparison of Canadian Standards, Australian Code, Wright-Walker Criteria and AASHTO Deflection Limit

(Hung X. Le and Eui-Seung Hwang, 2016)

CHAPTER 3. GRILLAGE ANALYSIS METHOD

This chapter briefly describes the three-dimensional dynamic modeling program created by Ming Liu (1996). The program models bridge-road-vehicle systems with the grillage method to capture both static and dynamic interactions.

3.1 Slab-on-Girder Bridge

The grillage bridge model is represented by an assembly of one-dimensional beams. These beams are subjected to perpendicular loads along the plane of the assembly. Unlike a plane frame, this assembly incorporates the beam's torsional stiffness. For a slab-on-girder bridge, the girders span longitudinally between the abutments with a thin slab spanning transversely along the top of the girders (See Figure 3.1). Since the slab has only a fraction of the flexural bending stiffness of the girders, the slab flexes in the transverse direction with a lot more curvature than in the longitudinal direction. The slab behaves similarly to a large number of transverse spanning planks. Generally, it is only in the immediate area of the concentrated loads where longitudinal moments and torques in the slab are comparable to the magnitudes of the transverse moments.

Developing a suitable grillage system for a slab-on-girder bridge is best achieved by considering the structural behavior of the specific bridge rather than a set of rules. Normally longitudinal grillage members are placed along the centerlines of the bridge girders, and the bridge slab is divided into equivalent transverse beams. The number of the equivalent transverse beams should be as large as possible. It is recommended that at least seven equivalent transverse

beams represent the slab. The spacing of the equivalent transverse beams should be less than 1.5 times that of the longitudinal grillage members (West, 1973).

3.1.1 Longitudinal Elements

Cross-sectional properties of longitudinal grillage members can be calculated similarly to composite T beams (See Figure 3.2). Flexural bending moments of inertia are calculated about the centroids of the cross-sections, ignoring the different levels of the centroids of interior and exterior members. If the bridge's girder spacing is greater than 1/6 of the effective bridge span, or if the edge cantilever exceeds 1/12 of the effective bridge span, shear lag will significantly reduce the effective width of the slab acting as a flange to each girder. In this case, the effective width of the slab should be the minimum of 1/4 of the effective bridge span, the spacing of bridge girders, or 12 times the slab thickness (AASHTO, 1992). However, it is often convenient to make the girder spacing the effective width of the slab. When the slab is subjected to torques, the girders behave as beams subjected to longitudinal torques. Nevertheless, the slab resists the torques in both directions. Thus, the torsional constant J_T of the longitudinal grillage member is:

$$J_T = J_g + J_{slab} \tag{3.1}$$

where,

J_g = torsional constant of the girder

J_{slab} = torsional constant of the equivalent transverse beam, in which

$$J_{slab} = \frac{bd^3}{6} \tag{3.2}$$

Where b and d are the width and thickness of the equivalent transverse beam, respectively.

The torsional constant of the girder, J_g, depends on the cross-sectional shape of the girder. For shapes without reentrances such as triangle, rectangle, circle, and ellipse Saint-Venant (1797-1886) derived an approximate expression given as follows:

$$J_g = \frac{A^4}{40 I_p} \tag{3.3}$$

where,

A = cross-sectional area

I_p = polar moment of inertia of the cross-section

Moreover, for a rectangular cross-section, Eq. (3.3) becomes:

$$J_{gr} = \frac{3b^3 d^3}{10(b^2+d^2)} \tag{3.4}$$

Where b and d are the width and height of the cross-section, respectively. If b ≥5d, Eq. (3.4) is reduced to:

$$J_{gtr} = \frac{bd^3}{3} \tag{3.5}$$

For shapes with reentrance such as I and L shapes, J, can be calculated by separating the cross-section into several pieces of rectangles, thus adding the torsional constants of these separated rectangles.

3.1.2 Transverse Elements

The cross-section properties of equivalent transverse beams can be calculated similarly to slabs.

Thus, the flexural bending moment of inertia I_b is:

$$I_b = \frac{bd^3}{12} \tag{3.6}$$

Where b and d are the width and thickness of the equivalent transverse beam, respectively.

The torsional constant, J_b, is:

$$J_b = \frac{bd^3}{12} \tag{3.7}$$

3.1.3 Stiffness Matrix

In reference to the local coordinate system as shown in Figure 3.3, the local stiffness matrix [K_L], considering the combination of flexural and torsional effects of a beam element with three DOFs at each end, is:

$$[K_L] = \frac{EI}{L^3}\begin{bmatrix} \frac{JGL^2}{EI} & 0 & 0 & -\frac{JGL^2}{EI} & 0 & 0 \\ 0 & 4L^2 & 6L & 0 & 2L^2 & -6L \\ 0 & 6L & 12 & 0 & 6L & -12 \\ \frac{-JGL^2}{EI} & 0 & 0 & \frac{JGL^2}{EI} & 0 & 0 \\ 0 & 2L^2 & 6L & 0 & 4L^2 & -6L \\ 0 & -6L & -12 & 0 & -6L & 12 \end{bmatrix} \tag{3.8}$$

where

L= Length

I= Flexural Bending Moment of Inertia

J= Torsional Constant

E= Modulus of Elasticity

G = Modulus of Rigidity

Subsequently, the global stiffness matrix for the grillage system can be obtained from an assembly of local stiffness matrices.

3.1.4 Mass Matrix

Similarly, the local consistent mass matrix [M_L] can be obtained as follows:

$$[M_L] = \frac{\bar{m}L}{420}\begin{bmatrix} \frac{140I_0}{A} & 0 & 0 & \frac{70I_0}{A} & 0 & 0 \\ 0 & 4L^2 & 22L & 0 & -3L^2 & 13L \\ 0 & 22L & 156 & 0 & -13L & 54 \\ \frac{70I_0}{A} & 0 & 0 & \frac{140I_0}{A} & 0 & 0 \\ 0 & -3L^2 & -13L & 0 & 4L^2 & -22L \\ 0 & 13L & 54 & 0 & -22L & 156 \end{bmatrix} \quad (3.9)$$

where

$\bar{m}$ = mass per unit length of beam element;

I_0 = polar mass moment of inertia; and

A = cross sectional area

Alternatively, the local mass matrix can be obtained from the lumped mass method. The lumped mass matrix [M_{lump}] may be expressed as:

$$\left[M_{lump}\right] = \frac{\bar{m}L}{2}\begin{bmatrix} \frac{I_0}{A} & 0 & 0 & 0 & 0 & 0 \\ 0 & 0 & 0 & 0 & 0 & 0 \\ 0 & 0 & 1 & 0 & 0 & 0 \\ 0 & 0 & 0 & \frac{I_0}{A} & 0 & 0 \\ 0 & 0 & 0 & 0 & 0 & 0 \\ 0 & 0 & 0 & 0 & 0 & 1 \end{bmatrix} \tag{3.10}$$

Similarly, the global mass matrix for the grillage system can be obtained from an assembly of local mass matrices.

3.1.5 Transformation Matrix

Since the local coordinate system does not always coincident with the global coordinate system, the transformation of coordinates is essential to assemble local matrices into global matrices. The transformation matrix may be expressed as:

$$[T] = \begin{bmatrix} \cos\theta & \sin\theta & 0 & 0 & 0 & 0 \\ -\sin\theta & \cos\theta & 0 & 0 & 0 & 0 \\ 0 & 0 & 1 & 0 & 0 & 0 \\ 0 & 0 & 0 & \cos\theta & \sin\theta & 0 \\ 0 & 0 & 0 & -\sin\theta & \cos\theta & 0 \\ 0 & 0 & 0 & 0 & 0 & 1 \end{bmatrix} \tag{3.11}$$

where

θ= rotation between the local and global coordinate system

3.1.6 Damping Matrix

The damping matrix for a grillage system, [C], is proportional to the global mass and stiffness matrices (Cough and Penzien 1975). [C] may generally be of the form:

$$[C] = [M] \sum_i a_i ([M]^{-1}[K])^i \quad (3.12)$$

where,

[M] = global mass matrix

[K] = global stiffness matrix

a_i = arbitrary proportionality factors, $-\infty < i < \infty$

To determine the arbitrary proportionality factors a_1, the modal damping ratio ξ_n for any specified mode n must be written as:

$$\xi = \frac{1}{2\omega_n} \sum_i a_i \omega^{2i} \quad (3.13)$$

where,

ω_n= natural frequency associated with any specified mode n.

In general, Eq. (3.13) can be written in matrix notation as

$$\{\xi\} = \frac{1}{2}[Q]\{a\} \quad (3.14)$$

where,

[Q] = square matrix containing different powers of natural frequencies.

The solution of Eq. (3.14) gives the arbitrary proportionality factors {a} as:

$$\{a\} = 2[Q]^{-1}\{\xi\} \tag{3.15}$$

The modal damping ratio { ξ } must be assigned in advance to get the factors {a}. Fortunately, the modal damping ratio { ξ } can be estimated from laboratory results or field-testing of existing structures. Although experimental modal damping ratios vary greatly, it is often conservative in assigning a value of 0.01 to 0.02 for steel structures and 0.03 to 0.05 for reinforced concrete structures, corresponding to the first natural frequencies of the structure. Damping ratios for higher modes are assumed to increase in proportion to higher natural frequencies.

3.1.7 Equivalent Nodal Loads

The grillage model deals with nodal forces and displacements of a grillage system. Therefore, wheel loads must be transferred into equivalent nodal forces when the wheel positions do not coincide with the grillage nodes. Conversely, stresses and displacements at any point on the bridge should be obtained from the nodal displacements through the same wheel load transformation. Jaeger and Bakht (1982) recommended that wheel loads can be distributed linearly in the longitudinal direction without taking into account any moments and nonlinearity in the transverse direction with bending moments (See Figure 3.4). The relevant wheel load transformation is given as follows:

$$P_1 = \frac{Pbd^2(2c+S)}{LS^3} T_1 = -\frac{Pbcd^2}{LS^2} \tag{3.16}$$

$$P_2 = \frac{Pad^2(2c+S)}{LS^3} T_2 = -\frac{Pacd^2}{LS^2} \tag{3.17}$$

$$P_3 = \frac{Pbc^2(2d+S)}{LS^3} T_3 = \frac{Pbc^2 d}{LS^2} \quad (3.18)$$

$$P_4 = \frac{Pa^{\ 2}(2d+S)}{LS^3} T_4 = \frac{Pa^{\ 2} d}{LS^2} \quad (3.19)$$

where,

P = applied wheel load

L = spacing between the relevant longitudinal grillage members

S = spacing between the relevant equivalent transverse beams

Chen (1994) simply assumed that wheel load distribution is in proportion to the tributary area without taking into account any moments, m, both longitudinal and transverse directions. Thus,

$$P_1 = \frac{Pbd}{LS} \quad (3.20)$$

$$P_2 = \frac{Pad}{LS} \quad (3.21)$$

$$P_3 = \frac{Pbc}{LS} \quad (3.22)$$

$$P_4 = \frac{Pac}{LS} \quad (3.23)$$

In general, wheel load transformation should be dependent on the structural behavior of the bridge slab. It is believed that the path of wheel load transmission is as follows: slab (equivalent transverse beams) ➔ girders ➔ abutments. Hence, wheel loads are first transferred from the equivalent transverse beams to the longitudinal grillage members, assuming each equivalent transverse beam has two fixed ends acting on the longitudinal grillage members. Thus,

$$PP_1 = \frac{Pd^2(2c+S)}{S^3} \qquad TP_1 = -\frac{Pcd^2}{S^2} \qquad MP_1 = -\frac{Pcd^2}{S^2}tg\theta \tag{3.24}$$

$$PP_2 = \frac{Pc^2(2d+S)}{S^3} \qquad TP_2 = \frac{Pc^2d}{S^2} \qquad MP_2 = -\frac{Pc^2d}{S^2}tg\theta \tag{3.25}$$

where,

θ= bridge skew angle

Afterward, the concentrated loads PP_i, TP_i, and MP_i (where i =1 and 2) are transferred into the equivalent nodal forces as below (William and Paul 1987).

$$P_1 = \frac{Pd^2(2c+S)}{S^3}(2\xi^3 - 3\xi^2 + 1) + \frac{6Pcd^2}{LS^2}(\xi^2 - \xi)tg\theta \tag{3.26a}$$

$$M_1 = -\frac{Pd^2(2c+S)L}{S^3}(\xi^3 - 2\xi^2 + \xi) - \frac{Pcd^2}{S^2}(3\xi^2 - 4\xi + 1)tg\theta \tag{3.26b}$$

$$T_1 = -\frac{Pcd^2}{S^2}(1 - \xi) \tag{3.26c}$$

$$P_2 = \frac{Pd^2(2c+S)}{S^3}(-2\xi^3 + 3\xi^2) - \frac{6Pcd^2}{LS^2}(\xi^2 - \xi)tg\theta \tag{3.27a}$$

$$M_2 = -\frac{Pd^2(2c+S)L}{S^3}(\xi^3 - \xi^2) - \frac{Pcd^2}{S^2}(3\xi^2 - 2)tg\theta \tag{3.27b}$$

$$T_2 = -\frac{Pcd^2}{S^2}\xi \tag{3.27c}$$

$$P_3 = \frac{Pc^2(2d+S)}{S^3}(2\xi^3 - 3\xi^2 + 1) + \frac{6Pc^2d}{LS^2}(\xi^2 - \xi)tg\theta \tag{3.28a}$$

$$M_3 = -\frac{Pc^2(2d+S)L}{S^3}(\xi^3 - 2\xi^2 + \xi) - \frac{Pc^2d}{S^2}(3\xi^2 - 4\xi + 1)tg\theta \tag{3.28b}$$

$$T_3 = -\frac{Pc^2d}{S^2}(1 - \xi) \tag{3.29c}$$

$$P_4 = \frac{Pc^2(2d+S)}{S^3}(-2\xi^3 + 3\xi^2) - \frac{6Pc^2d}{LS^2}(\xi^2 - \xi)tg\theta \tag{3.30a}$$

$$M_4 = -\frac{Pc^2(2d+S)L}{S^3}(\xi^3 - \xi^2) - \frac{Pc^2d}{S^2}(3\xi^2 - 2)tg\theta \tag{3.30b}$$

$$T_4 = -\frac{Pc^2 d}{S^2}\xi \tag{3.30c}$$

where

$$\xi = \frac{a}{L}$$

3.1.8 Dynamic Equations

The dynamic equations of a bridge subjected to wheel loads can easily be established from the global mass [M] and stiffness [K] matrices as well as damping [C] matrix that is

$$[M]\{\ddot{\delta}\} + [C]\{\dot{\delta}\} + [K]\{\delta] = \{P\} \tag{3.30}$$

where,

{P} = equivalent nodal force vector

$\{\delta\}$ = nodal displacement vector

$\{\dot{\delta}\}$ = nodal velocity vector

$\{\ddot{\delta}\}$ = nodal acceleration vector

Moreover, the static equations of a bridge may simply be expressed as:

[K]{δ} = {P} (3.31)

3.1.9 Strains and Displacements

Once the nodal displacements are obtained from Eq. (3.30) and Eq. (3.31), the displacements a_1 any points on the bridge, u, can be derived from the beam bending displacement function as following:

$$\upsilon = N_1\upsilon_0 + N_2\theta_0 + N_3\upsilon_L + N_4\theta_L \quad (3.32)$$

$$N_1 = 1 - 3\xi^2 + 2\xi^3$$

$$N_2 = L(\xi - 2\xi^2 + \xi^3)$$

$$N_3 = 3\xi^2 - 2\xi^3$$

$$N_4 = l(-\xi^2 + \xi^3)$$

υ_0, υ_L = vertical nodal displacements of the relevant longitudinal member;

θ_0, θ_L= rotational nodal displacements of the relevant longitudinal member.

Moreover, the strains a_1 any points on the bridge can be obtained from the derivatives of the displacement function. Considering the bending moments only, the strains are:

$$\varepsilon = N_1''\upsilon_0 + N_2''\theta_0 + N_3''\upsilon_L + N_4''\theta_L \quad (3.33)$$

where

$$N_1'' = \frac{1}{L^2}(-6 + 12\xi)$$

$$N_2'' = \frac{1}{L}(-4 + 6\xi)$$

$$N_3'' = \frac{1}{L^2}(-6 + 12\xi)$$

$$N_4'' = \frac{1}{L}(-2 + 6\xi)$$

3.2 Road Roughness Input

Road roughness usually refers to an uneven, impaired, or bumpy pavement on a bridge. The American Society of Testing and Materials (ASTM) defines road roughness as "the deviations of a pavement surface from a true planar surface with characteristic dimensions greater than 0.6 in." to distinguish road roughness from pavement texture. In the case of road roughness (elevation) profiles existing, they can be directly adopted. Otherwise, PSD will be used to generate road roughness profiles. The generations of road roughness profiles may be considered as stationary Gaussian random processes.

3.2.1 Generation of Single Road Roughness Profile

The stationary Gaussian random process X (t) can be considered as a simple periodic cosine function of time with amplitude α, circular frequency ω, and phase angle θ:

$$X(t) = \alpha\cos(\omega t - \theta) \tag{3.34}$$

or in discrete form

$$X(t) = \sum_{n=1}^{N} \alpha_n \cos(\omega_n t - \theta_n) \tag{3.35}$$

It is assumed that the phase angle θ_n is an independent random variable distributed uniformly in the range from 0 to 2π. Thus, the ensemble mean is:

$$E[X(t)] = \sum_{n=1}^{N} \alpha_n E[\cos(\omega_n t - \theta_n)] = 0 \tag{3.36}$$

Since,

$$E[\cos\theta_n] = \int_0^{2\pi} (\cos\theta_n)\left(\frac{1}{2\pi}\right) d\theta_n = 0 \quad (3.37)$$

The ensemble mean square is:

$$E[X^2(t)] = E\left[\sum_{n=1}^{N} \alpha_n \cos(\omega_n t - \theta_n) \sum_{m=1}^{M} \alpha_m \cos(\omega_m t - \theta_m)\right] = \sum_{n=1}^{N} \frac{1}{2}\alpha_n^2 \quad (3.38)$$

Eq. (3.37) and Eq. (3.38) demonstrate the stationary of the random process X (t).

Furthermore, the standard deviation, σ, for the stationary Gaussian random process X (t) may be defined as:

$$\sigma^2 = \int_{-\infty}^{\infty} S_{xx}(\omega) d\omega - m^2 \quad (3.39)$$

where

m = mean of random process X (t)

$S_{xx}(\omega)$ = PSD of random process X (t)

m and $S_{xx}(\omega)$ are statistical parameters used to describe road roughness conditions. Since the white-noise slope model is adopted in this thesis, m is defined as zero, i.e., m = 0. $S_{xx}(\omega)$ can be expressed by an exponential function (Dodds and Robson 1973):

$$S_{xx}(\gamma) = \alpha\gamma^{-n} \quad (3.40)$$

where

α = constant roughness coefficient: and

γ = special frequency or wavenumber, in which

$$\gamma = \frac{1}{\lambda} = \frac{1}{TV} = \frac{2\pi}{T} \cdot \frac{1}{2\pi V} = \frac{\omega}{2\pi V} \tag{3.41}$$

λ = wave length;

T = period; and

V = velocity.

Substituting m = 0 and discrediting Eq. (3.39), thus

$$\sigma^2 = 2\sum_{n=1}^{N} S_{xx}(\omega_n)\Delta\,\omega_n = E[X^2(t)] \tag{3.42}$$

Comparing Eq. (3.38) and Eq. (3.42) gives

$$\alpha_n = \sqrt{4S_{xx}(\omega_n)\Delta\omega_n} \tag{3.43}$$

Therefore, Eq. (3.35) becomes

$$X(t) = \sum_{n=1}^{N} \sqrt{4S_{xx}(\omega_n)\Delta\omega_n}\cos\,(\omega_n t - \theta_n) \tag{3.44}$$

Finally, substituting Eq. (3.41) into Eq. 3.44), the single road roughness profile can be generated randomly as:

$$X(\xi) = \sum_{n=1}^{N} \sqrt{4S_{xx}(\gamma_n)\Delta\gamma_n}\cos\,(2\pi\gamma_n\xi - \theta_n) \tag{3.45}$$

where

ξ = longitudinal distance, i.e. ξ = Vt;

$\Delta\gamma_n$ = bandwidth of the nth component, in which

$$\Delta\gamma_n = \frac{\gamma_{n+1}-\gamma_{n-1}}{2} \quad (3.46)$$

The number of components N in Eq. (3.45) should be large enough so that an exact value of the particular frequency (or wavenumber) γ within a frequency window Δ γ is insignificant. The particular frequency (or wavenumber) γ usually covers a range from 0.0033 to 1 cycle/ ft. (wavelengths from 1 to 300 ft. /cycle), with a Δ γ interval of 0.0033 cycle/ft. for low frequencies and 0.01 for higher frequencies (Sayers 1988). The typical single road roughness profile generated from PSD will be shown in Figure 3.5.

3.2.2 Generation of Two Correlated Road Roughness Profiles

For 3-D computer simulations, two correlated road roughness profiles ought to be developed instead of a single "bicycle model" road profile. In this case, three spectral densities are required: PSD for each profile and cross-spectral density. Furthermore, the road surface is assumed isotopic, which means any road roughness profiles in any directions have the same statistical properties. Thus,

$R_{xx} = R_{yy} = R_{nn}$ (3.47)

$$S_{xx}(\omega) = S_{yy}(\omega) = S_{nn}(\omega) \quad (3.48)$$

where

R_{xx} = autocorrelation function of the independent random process X (t);

R_{nn}= autocorrelation function of the independent random process N (t);

R_{yy} = autocorrelation function of the correlated random process Y (t);

$S_{xx}(\omega)$ = PSD function of X (t);

$S_{nn}(\omega)$ = PSD function of N (t);

$S_{yy}(\omega)$= PSD function of Y (t)

Therefore, the correlated random process Y (t) corresponding to the independent random processes X (t) and N (t) may be generated as follows:

$$Y(t) = \alpha X(t-\tau_0) + \beta N(t)$$

$$R_{yy}(\tau) = E[Y(t)Y(t+\tau)] \tag{3.49}$$

$$= E[\{\alpha X(t-\tau_0) + \beta N(t)\}\{\alpha X(t+\tau-\tau_0) + \beta N(t+\tau)\}] \tag{3.50}$$

$$= \alpha^2 R_{xx}(\tau) + \beta^2 R_{nn}(\tau)$$

where

τ_0 = time delay

$\alpha \cdot \beta$ = assumed parameters

Substituting Eq. (3.47) into Eq. (3.49), thus

$$\propto^2 + \beta^2 = 1 \tag{3.51}$$

Moreover, the correlation function of X (t) and Y (t) will be:

$$R_{xy}(\tau) = E[X(t)Y(t+\tau)]$$

$$= E[X(t)\{\alpha X(t+\tau-\tau_0) + \beta N(t+\tau)\}]$$

$$= \propto E[X(t)X(t+\tau-\tau_0)]$$

$$= \propto R_{xx}(\tau-\tau_0) \quad (3.52)$$

Taking the Fourier transform of Eq. (3.51) gives:

$$\frac{1}{2\pi}\int_{-\infty}^{\infty} R_{xy}(\tau)e^{-1\omega\tau}d\tau = \frac{\propto}{2\pi}\int_{-\infty}^{\infty} R_{xx}(\tau-\tau_0)e^{-1\omega\tau}d\tau = \frac{\propto}{2\pi}\int_{-\infty}^{\infty} R_{xx}(\tau')e^{-1\omega(\tau\prime-\tau_0)}d\,\tau' \quad (3.53)$$

where

T’ = τ- τ_0

By the definition of PSD, Eq. (3.53) becomes:

$$S_{xy}(\omega) = \alpha S_{xx}(\omega)\, e^{-1\omega\tau_0} \quad (3.54)$$

that is

$$\left|S_{xy}(\omega)\right| = \alpha S_{xx}(\omega) \quad (3.55)$$

Furthermore, by the definition of the coherence function $\gamma_{xy}(\omega)$

$$\gamma_{xy}^2(\omega) = \frac{\left|S_{xy}(\omega)\right|^2}{S_{xx}(\omega)S_{yy}(\omega)} \quad (3.56)$$

The assumed α may be derived from Eq. (3.48), Eq. (3.55) and Eq. (3.56).

$$\propto = \frac{|S_{xy}(\omega)|}{S_{xx}(\omega)} = \sqrt{\frac{|S_{xy}(\omega)|^2}{S_{xx}(\omega)S_{yy}(\omega)}} = \sqrt{\gamma_{xy}^2(\omega)} = \gamma_{xy}(\omega) \tag{3.57}$$

Combining Eq. (2.49), Eq. (2.51) and Eq. (2.57) gives

$$Y(t) = \gamma_{xy}(\omega)X(t) + \sqrt{t - \gamma_{xy}^2(\omega)N(t)} \tag{3.58}$$

For two correlated random processes X(t) and Y(t) with the spacing distance b on an isotopic surface as shown in Figure 3.6, the coherence function $\gamma_{xy}(\omega_n)$ can be expressed as:

$$\gamma_{xy}(\omega) = \frac{|S_{xy}(\omega)|}{S(\omega)} = \frac{\int_0^\infty R(\rho)cos\omega_n}{\int_0^\infty R(\xi)cos\omega_n \xi d\xi} \tag{3.59}$$

where

$$\rho = \sqrt{\xi^2 + b^2}$$

Clearly, $\gamma_{xy}(\omega)$ is equals to unity when b = 0, i.e., X (t) and Y (t) are the same random processes. $\gamma_{xy}(\omega)$ is equals to zero when b = ∞, i.e., X (t) and Y (t) are totally independent.

In practice, Eq. (3.58) can be written in discrete form as:

$$Y(t) = \sum_{n=1}^{N} \gamma_{xy}(\omega_n)\sqrt{4S_{xx}(\omega_n)\Delta\omega_n}\cos(\omega_n t - \phi_n) + \sum_{n=1}^{N}\sqrt{1-\gamma_{xy}^2(\omega_n)}\sqrt{4S_{xx}(\omega_n)\Delta\omega_n}\cos(\omega_n t - \varphi_n) \quad (3.60)$$

where

ϕ_n, φ_n =independent random phases distributed uniformly between 0 to 2 π.

Typical two correlated road roughness profiles randomly generated from PSD and coherence function are shown in Figure 2.7.

3.2.3 Measurement of Road Roughness Profiles

Manual methods and high-speed profiling systems are used to measure road roughness profiles. The most apparent manual method is with a surveyor's rod and level. Although difficult and time-consuming, this manual method is straightforward and contains no surprising sources of error. The accuracy of this method is primarily determined by the precision of level instruments, proficiency of surveyors, and sampling interval between measurements. The sampling interval usually covers a range from 10 to 20 inches, in which higher intervals have higher priorities for saving time and labor. Other manual profiling methods, such as TRRL Beam and Dipstick., which have been developed for providing greater efficiency and eliminating manual errors of data processing, were reported by Sayers (1988). The original high-speed profiling systems were mechanical profiling systems mounted on moving vehicles. More recently, mechanical profiling systems have been replaced by digital analysis, noncontact, and computer control systems using ultrasound, laser beams, or optical images. More information concerning these commercial high-speed profiling systems was also reported by Sayers (1988).

Measurements must be converted to the International Roughness Index (IRI) to classify road conditions. The IRI is defined as a transportable scale to be independent on profiling systems but highly correlated with PSD and subjective opinions concerning road conditions.

3.3 Vehicle Model

The five-axle semi tractor-trailer is considered in the grillage analysis. This truck is assumed to be composed of three components: tire, suspension, and truck body. Five rigid masses are used to represent the tractor, semi-trailer, and three tire-axle sets, respectively. The tractor and semi-trailer are each assigned three DOFs, corresponding to the vertical displacement, pitching rotation about the transverse axis, and twisting rotation about the longitudinal axis. The tire-axle sets are each provided with two DOFs related to the vertical and twisting rotational movements. The tractor and semi-trailer are interconnected at the pivot point. Therefore, the independent DOF of this truck is eleven, although the total DOF is twelve. Because of the complexity of tire-suspension mechanical properties, some assumptions are made to simplify the vehicle model. These assumptions are (1) truck bodies, and tire-axle sets are rigid; (2) mass centers of the tractor and semi-trailer are assumed to be at the same level of the pivot point; (3) all of the vehicle components move with the same constant speed in the longitudinal direction; (4) each tire contacts the bridge at a single point and (5) only vertical interaction forces between the bridge and vehicle are considered, i.e., the horizontal friction forces are ignored.

3.3.1 Dynamic Properties of Vehicle Components

The five-axle semi tractor-trailer is assumed to be equipped with multi-leaf spring suspensions. In essence, multi-leaf spring suspensions are the non-linear devices that dissipate energy during each cycle of oscillation. The suspension frequency of oscillation usually occurs in a range from

O to 15 Hz. Fancher (1980) measured suspension characteristics, and showed that force-deflection relationships of suspensions are independent of suspension frequencies of oscillation, but are dependent on the amplitudes of suspension motions and nominal applied loads. The equation for the force-deflection relationship representing a leaf spring suspension is suggested as following:

$$SF_i = SF_{ENVi} + (SF_{i-1} - SF_{ENVi})e^{|\delta_i - \delta_{i-1}|/\beta} \quad (3.61)$$

SF_i = suspension force at the current time step;

SF_{i-1} = suspension force at the last time step;

δ_i = suspension deflection at the current time step;

δ_{i-1} = suspension deflection at the last time step;

SF_{ENVi} = suspension force corresponding to the upper and lower boundaries of the envelope of the measured spring suspension characteristics at the deflection δ_i

β = input parameter used for describing the rate at which the suspension force within a hysteresis loop approaches the outer boundary of the envelope.

In this equation, SF_{ENVi} and β have different values for the front, middle, and rear tire-axle sets, corresponding to the force-deflection diagrams shown in Figures 3.8-3.10.Eq. (3.61) is easy to install in time integration methods, but it requires iterations to find the forces and deflections at the current time.

The mechanical properties of tires are supposed to be linear, ignoring the effect of tire damping. The spring constant of tires is assigned as 5,000 lb. / in / tire (Hwang 1990).

The truck bodies are modeled as masses subjected to rigid body motions. The vertical displacements, pitching, and twisting rotations are accounted for masses and mass moments of inertia of the truck bodies. The mass moments of inertia of truck bodies can be obtained from a simple model as below.

Assumed the trapezoidal and uniform weight distributions in the x-x and y-y directions, respectively (see Figure. 3.7), the truck mass moment of inertia in the x-x direction, I_{xx}, can be expressed in terms of the constant mass density of truck (ρ) as:

$$I_{xx} = \frac{\rho B^3 L(p+q)}{24} \tag{3.62}$$

Similarly, the truck mass moment of inertia in the y-y direction, I_{yy}, is:

$$I_{yy} = \frac{\rho B L^3 p^2}{36} + \frac{4pq+q^2}{p+q} \tag{3.63}$$

where

B = width of the truck body;

L = length of truck body;

p and q = assumed parameters.

From geometric properties of trapezoid shape, volume V and relationship between p and q are:

$$V = \frac{p+q}{2}(1+2r)(a+b)B \tag{3.64}$$

$$q = \frac{(r+2)a+(r-1)b}{(r-1)a+(r+2)b} \cdot p \tag{3.65}$$

where

a = distance between the mass center and front axle;

b = distance between the mass center and rear axle;

r =$\frac{c}{a+b}$;

c = distance between the truck body edges and axles.

Furthermore, the total weight of the truck body, W, is

$$W = \frac{\rho}{2}(1+2r)(p+q)(a+b)B \tag{3.66}$$

From Eq. (3.65) and Eq. (3.66), Eq. (3.62) and Eq. (3.63) becomes:

$$I_{xx} = \frac{WB^2}{12} \tag{3.67}$$

$$I_{yy} = \frac{W}{6}(4(r^2+r+1)ab + (2r^2+2r-1)(a^2+b^2)) \tag{3.68}$$

Therefore, the truck mass moments of inertia depend on the truck's physical dimensions and total weight.

3.3.2 Dynamic Equations of Motion for Vehicle Model

The 3-D vehicle model and its free body diagrams are shown in Figures 3.8-3.9. Twelve equilibrium equations can be obtained from vertical, pitching and twisting rotation movements:

$$m_f \ddot{z}_f + TF_{fr} + TF_{fl} - SF_{fr} - SF_{fl} = 0 \quad (3.69)$$

$$m_m \ddot{z}_m + TF_{mr} + TF_{ml} - SF_{mr} - SF_{ml} = 0 \quad (3.70)$$

$$m_r \ddot{z}_r + TF_{rr} + TF_{rl} - SF_{rr} - SF_{rl} = 0 \quad (3.71)$$

$$I_f \ddot{\propto}_f - \left(TF_{fr} - TF_{fl}\right)\left(\frac{WD}{2}\right) + \left(SF_{fr} - SF_{fl}\right)\left(\frac{SD}{2}\right) = 0 \quad (3.72)$$

$$I_m \ddot{\propto}_m - \left(TF_{mr} - TF_{ml}\right)\left(\frac{WD}{2}\right) + \left(SF_{mr} - SF_{ml}\right)\left(\frac{SD}{2}\right) = 0 \quad (3.73)$$

$$I_r \ddot{\propto}_r - \left(TF_{rr} - TF_{rl}\right)\left(\frac{WD}{2}\right) + \left(SF_{rr} - SF_{rl}\right)\left(\frac{SD}{2}\right) = 0 \quad (3.74)$$

$$m_T \ddot{z}_T + SF_{fr} + SF_{fl} + SF_{mr} + SF_{ml} + P_j = 0 \quad (3.75)$$

$$m_R \ddot{z}_R + SF_{rr} + SF_{rl} - P_j = 0 \quad (3.76)$$

$$I_{T\theta} \ddot{\theta}_T + a_{fc} D_{fm}\left(SF_{fr} + SF_{fl}\right) - \left(1 - a_{pc}\right) D_{fm}\left(SF_{mr} + SF_{ml}\right)\left(a_{fp} - a_{fc}\right) D_{fm} P_j = 0 \quad (3.77)$$

$$I_R \ddot{\theta}_R - \left(1 - a_{pc}\right) D_{pr}\left(SF_{rr} + SF_{rl}\right) - a_{pc} D_{pr} P_j = 0 \quad (3.78)$$

$$I_{T\propto} \ddot{\propto}_T + \frac{SD}{2}\left(SF_{fl} + SF_{ml} - SF_{fr} - SF_{mr}\right) = 0 \quad (3.79)$$

$$I_{R\propto} \ddot{\propto}_R + \frac{SD}{2}\left(SF_{rl} - SF_{rr}\right) = 0 \quad (3.80)$$

where

z_f, z_m, z_r = vertical displacements of the front middle and rear tire-axle sets;

α_f, α_m, α_r = twisting rotations of the front, middle and rear tire-axle sets;

z_T, z_R = vertical displacements of the mass centers of the tractor and semi-trailer,

θ_T, θ_R= pitching rotations of the mass centers of the tractor and semi-trailer;

α_T, α_R = twisting rotations for the mass centers of the tractor and semi-trailer;

m_r, m_m, m_r = masses for the front, middle and rear tire-axle sets;

I_r, I_m, I_r = mass moments of inertia subjected to the twisting rotations of the front, middle and rear tire-axle sets;

m_T, m_R = masses of the tractor and semi-trailer,

$I_{T\theta}$, $I_{R\theta}$ = mass moments of inertia subjected to the pitching rotations of the tractor and semi-trailer;

$I_{T\alpha}$, $I_{R\alpha}$ = mass moments of inertia subjected to the twisting rotations of the tractor and semi-trailer;

TF_{ij}, SF_{ij} = tire, and suspension forces, in which i = f, m, and r stand for the front middle and rear tire-axle sets, respectively; and j = r and 1 stand for the right and left side of the truck body, respectively;

P_j = connection force at the pivot point;

WD = distance between the right and left tires;

SD = distance between the right and left suspensions;

D_{fm} = distance between the front and middle tire-axle sets;

D_{pr} = distance between the pivot point and rear tire-set;

$a_{fc} = \frac{D_{fc}}{D_{fm}}$, in which D_{fc} is the distance between the front tire-axle set and mass center of the tractor;

$a_{fp} = \frac{D_{fp}}{D_{fm}}$, in which D_{fp} is the distance between the front tire-axle set and pivot point; and

$a_{pc} = \frac{D_{pc}}{D_{pr}}$, in which D_{pc} is the distance between the pivot point and mass center of the semi-trailer.

Assumed the tractor and semi-trailer as rigid bodies, seven geometric equations can be derived as follows:

$$z_T = \left(\frac{1}{2} - a_{fc}\right) z_{fsr} + a_{fc} z_{msr} + \frac{z_{fsl}}{2} \tag{3.81}$$

$$\theta_T = -\frac{z_{msr}-z_{fsr}}{D_{fm}} \tag{3.82}$$

$$\propto_T = -\frac{z_{fsl}-z_{fsr}}{SD} \tag{3.83}$$

$$z_R = (1-a_{Pc})z_p + \frac{a_{pc}}{2}z_{rsr} + \frac{a_{pc}}{2}z_{rsl} \tag{3.84}$$

$$\theta_R = -\frac{z_{rsr}+z_{rsl}-2z_p}{2(D_{pr})} \tag{3.85}$$

$$\propto_R = -\frac{z_{rsl}-z_{rsr}}{SD} \tag{3.86}$$

$$z_{trs} - z_{msr} - z_{fsl} + z_{msl} = 0 \tag{3.87}$$

where

$$z_p = \left(\frac{1}{2} - a_{fp}\right) z_{fsr} + a_{fp} z_{msr} + \frac{z_{fsl}}{2} \tag{3.88}$$

$$z_{fsr} = z_f - \propto_f \frac{SD}{2} \tag{3.89}$$

$$z_{fsl} = z_f + \propto_f \frac{SD}{2} \tag{3.90}$$

$$z_{msr} = z_m - \propto_m \frac{SD}{2} \tag{3.91}$$

$$z_{msl} = z_m + \propto_m \frac{SD}{2} \tag{3.92}$$

$$z_{rsr} = z_r - \propto_r \frac{SD}{2} \tag{3.93}$$

$$z_{rsl} = z_r + \propto_r \frac{SD}{2} \tag{3.94}$$

Substituting Eq. (3.81-3.94) into Eq. (3.69-3.80), the equations are expressed as 7 x 7 matrix as following:

$$[A] * [\ddot{Z}] = [B] \tag{3.95}$$

where

$$[A]=\begin{bmatrix} \frac{I_{T\theta}}{D_{fm}} & -\frac{I_{T\theta}}{D_{fm}} & 0 & 0 & 0 & 0 & -(a_{fc}-a_{fp})D_{fm} \\ \frac{I_{R\theta}}{D_{pr}}\left(\frac{1}{2}-a_{fp}\right) & \frac{I_{R\theta}}{D_{pr}}a_{fp} & -\frac{I_{R\theta}}{2D_{pr}} & \frac{I_{R\theta}}{2D_{pr}} & 0 & -\frac{I_{R\theta}}{2D_{pr}} & a_{pc}D_{pr} \\ \frac{I_{T\alpha}}{SD} & 0 & 0 & -\frac{I_{T\alpha}}{SD} & 0 & 0 & 0 \\ 0 & 0 & \frac{I_{R\alpha}}{SD} & 0 & 0 & -\frac{I_{R\alpha}}{SD} & 0 \\ m_T\left(\frac{1}{2}-a_{fc}\right) & m_T a_{fc} & 0 & \frac{m_T}{2} & 0 & 0 & -1 \\ m_R\left(\frac{1-a_{pc}}{2}-a_{fp}(1-a_{pc})\right) & m_R a_{fp}(1-a_{pc}) & m_R\frac{a_{pc}}{2} & m_R\frac{(1-a_{pc})}{2} & 0 & m_R\frac{a_{pc}}{2} & 1 \\ 1 & -1 & 0 & -1 & 1 & 0 & 0 \end{bmatrix}$$

$$[B]=\begin{bmatrix} -(1-a_{fc})D_{fm}(SF_{fl}+SF_{ml})+a_{fc}D_{fm}(SF_{fr}+SF_{fr}) \\ -(1-a_{pc})D_{pr}(SF_{rr}+SF_{rl}) \\ \frac{SD}{2}(SF_{fr}+SF_{mr}-SF_{fl}-SF_{ml}) \\ \frac{SD}{2}(SF_{rr}-SF_{rl}) \\ (SF_{fr}+SF_{mr}+SF_{fl}+SF_{ml}) \\ SF_{rr}+SF_{rl} \\ 0 \end{bmatrix}$$

$$\{\ddot{Z}\}=\begin{Bmatrix} \ddot{z}_{fsr} \\ \ddot{z}_{msr} \\ \ddot{z}_{rsr} \\ \ddot{z}_{fsl} \\ \ddot{z}_{msl} \\ \ddot{z}_{rsl} \\ P_j \end{Bmatrix}$$

The suspension forces SF_{ij} can be calculated from Eq. (2.61) and the tire forces TF_{ij} are calculated as follows:

$$TF_{ij} = TK_{ij}\,(Z_{ij} + x_{ij} - zb_{ij}) \qquad (3.96)$$

where

TK_{ij} = elastic spring constant of tire ij

x_{ij} = road roughness (elevation) at tire ij

zb_{ij} = bridge deflection at tire ij

z_{ij} = vertical displacement at tire ij

$$z_{fr} = z_f - \propto_f \frac{WD}{2} \tag{3.97}$$

$$z_{fl} = z_f + \propto_f \frac{WD}{2} \tag{3.98}$$

$$z_{mr} = z_m - \propto_m \frac{WD}{2} \tag{3.99}$$

$$z_{ml} = z_m + \propto_m \frac{WD}{2} \tag{3.100}$$

$$z_{rr} = z_r - \propto_r \frac{WD}{2} \tag{3.101}$$

$$z_{rl} = z_r + \propto_r \frac{WD}{2} \tag{3.102}$$

3.4 Computer Simulation Program

The computer simulation program has been developed on the SUN Workstation. The main program procedures include matrix generation and decomposition, eigenvalue and eigenvector extraction, and systematic transient response. The Newmark-β method is used to integrate dynamic equations of the bridge under nonlinear and non-periodic wheel loads.

3.4.1 Algorithm

Bridge stiffness and mass matrix are generated from Eq. (3.8) and Eq. (3.9). Bridge natural frequencies and normal modes are obtained by extracting eigenvalues and eigenvectors from free dynamic equations of the bridge. The Eigen problems are solved by the Jacobi Method,

which is an iterative procedure that can approach the eigenvalues using a finite number of steps (Al-Khafaji 1986). The dynamic equations of bridge and vehicle in Eq. (3.30) and Eq. (3.95) are integrated by the Newmark-β Method. Iterations are required to obtain the wheel loads and suspension forces in Eq. (3.61). The iterations continue until the differences between the computed and assumed wheel loads and suspension forces are less than the desired tolerance, which is taken as 0.01.

3.4.2 Newmark-β method

The Newmark-β method, as the best-known direct numerical integration procedure, is mentioned in this section. Based on the linear acceleration method, the forward integrations of velocities and displacements are

$$\dot{\delta}_{t+\Delta t} = \dot{\delta}_t + [(1+\alpha)\ddot{\delta}_t + \alpha\ddot{\delta}_{t+\Delta t}]\Delta t \tag{3.103}$$

$$\delta_{t+\Delta t} = \delta_t + \dot{\delta}_t\Delta t + [\left(\frac{1}{2} - \beta\right)\ddot{\delta}_t + \beta\ddot{\delta}_{t+\Delta t}]\Delta t^2 \tag{3.104}$$

where

α, β = weighing factors

To capture the dynamic behavior of the bridge with reasonable accuracy, the interval between successive time increments is taken as 0.001. This time increment is very important for the convergent of the Newmark-β method, and it must less than 1/20f, where f is the highest natural frequency of the bridge, which ranges from 5 to 20 Hz for the slab-on-girder bridges.

The flowchart of the computer program is shown in Figure 3.10. The simulation starts when the front axle of the truck enters the bridge and stops when the rear axle leaves the bridge. At each time step, the wheel positions are located using truck configurations, truck speed, and time increments. The initial conditions of the current time step are the same as the computed results of the previous time step. The assumed wheel loads are transferred into the nodal loads in the grillage mesh, considering the applied forces, bending, and torsional moments. When the first contact happens between the tire and the bridge, bridge stiffness and mass matrix are generated, and the bridge natural frequencies and normal modes are obtained by solving for eigenvalues and eigenvectors. The Eigen problems are solved by the Jacobi Method, which is an iterative procedure that can approach the eigenvalues using a finite number of steps. Using the grillage nodal accelerations, the grillage nodal velocities and displacements are integrated by the Newmark-β Method. The bridge displacements at each wheel position are calculated from the four adjacent nodal displacements, using displacement shape function as following:

$$\upsilon = N_1\upsilon_0 + N_2\theta_0 + N_3\upsilon_L + N_4\theta_L \tag{3.105}$$

where

$\upsilon =$ displacements at any point on the bridge

$N_1 = 1 - 3\xi^2 + 2\xi^3$

$N_2 = L(\xi - 2\xi^2 + \xi^3)$

$N_3 = 3\xi^2 + 2\xi^3$

$N_4 = L(-\xi + \xi^3)$

The new wheel loads are computed from the resulting girder-deck displacements at the wheel positions and the road roughness profile. If the difference between the new and assumed wheel loads is less than the designated tolerance, the program will continue to the next time step. Otherwise, the program will go back to the beginning of the current time step, using the new wheel loads as the assumed wheel loads. Once the iteration converges, the girder deflections at given locations can be calculated using Eq. (3.104). Similarly, strains and stresses can be obtained at any point in any girder.

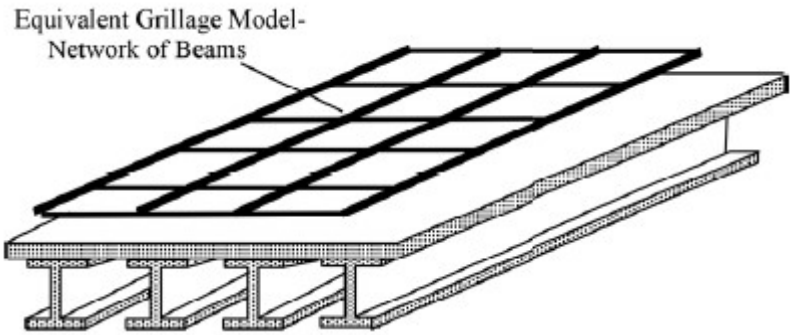

Figure 3.1: Grillage System for Slab-on-Girder Bridge

(Liu, 1996)

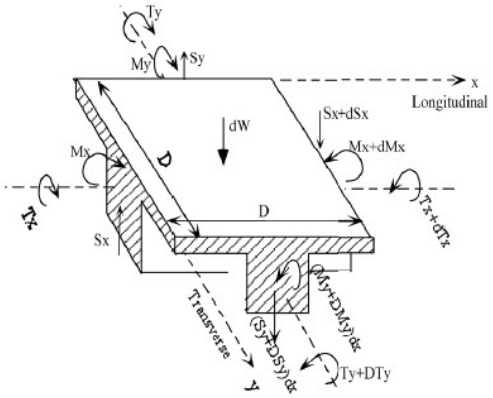

Figure 3.2: Cross Sectional Properties of Grillage Member

(Liu, 1996)

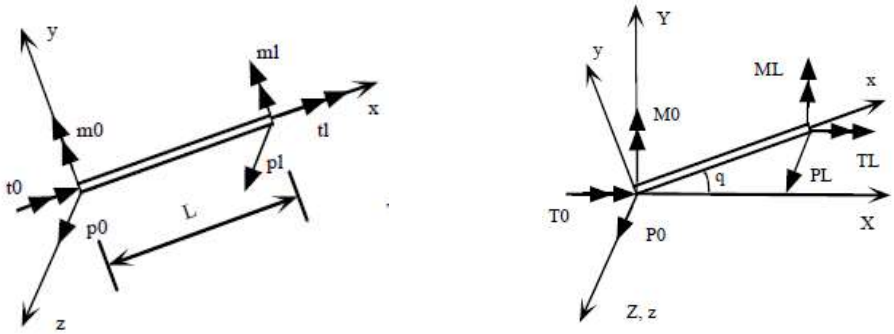

(a) Local Coordinates (b) Global Coordinates

Figure 3.3 Local and Global Coordinate System

(Liu, 1996)

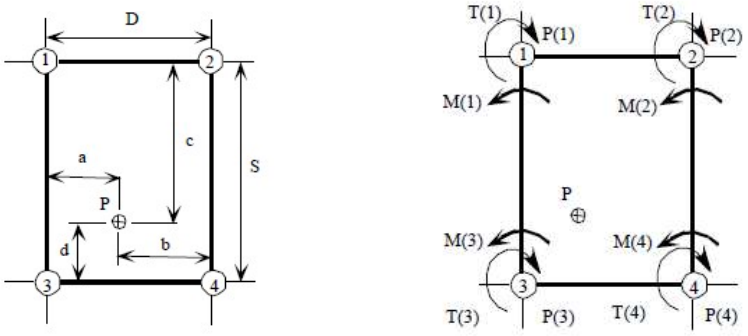

(a) Equivalent Nodal Loads (b) Wheel Load Position

Figure 3.4 Wheel Load Transformation

(Liu, 1996)

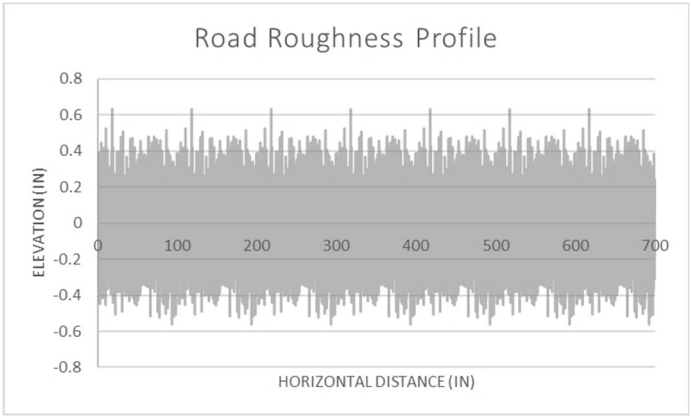

Figure 3.5: Randomly Generated Single Road Roughness Profile

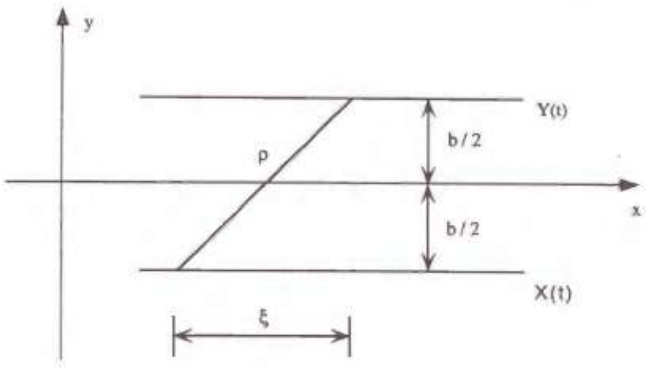

Figure 3.6: Road Parameters on an Isotopic Surface

(Liu, 1996)

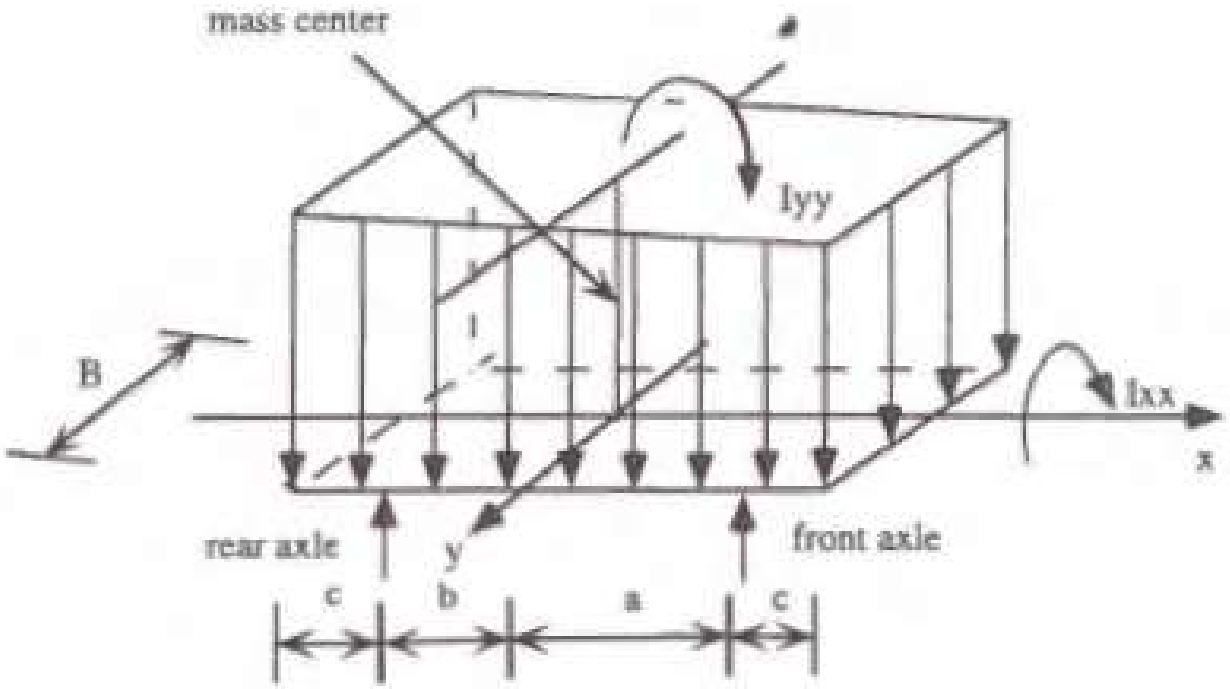

(a) Tractor

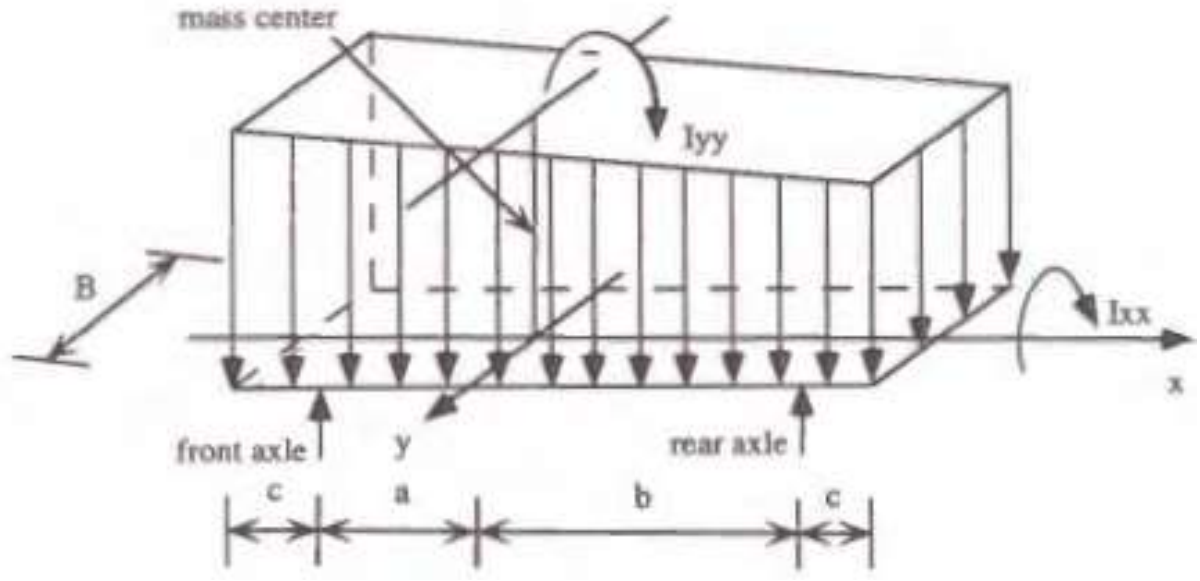

(b) Semi-Trailer

Figure 3.7: Truck Mass Distribution

(Liu, 1996)

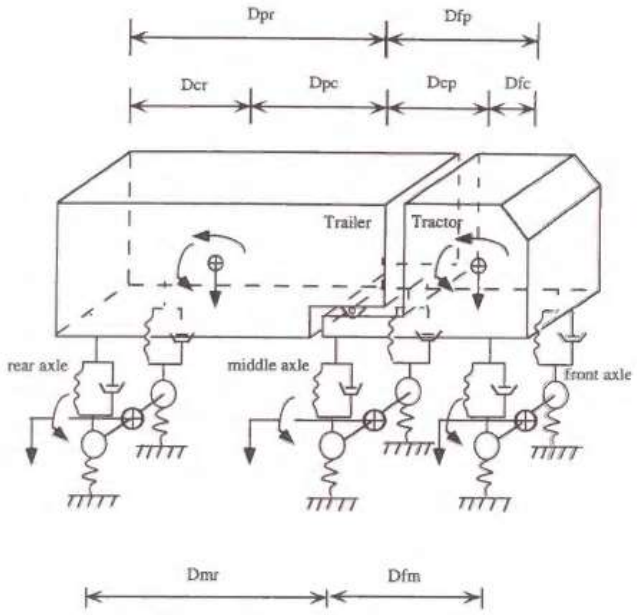

Figure 3.8: 3-D Vehicle Model

(Liu, 1996)

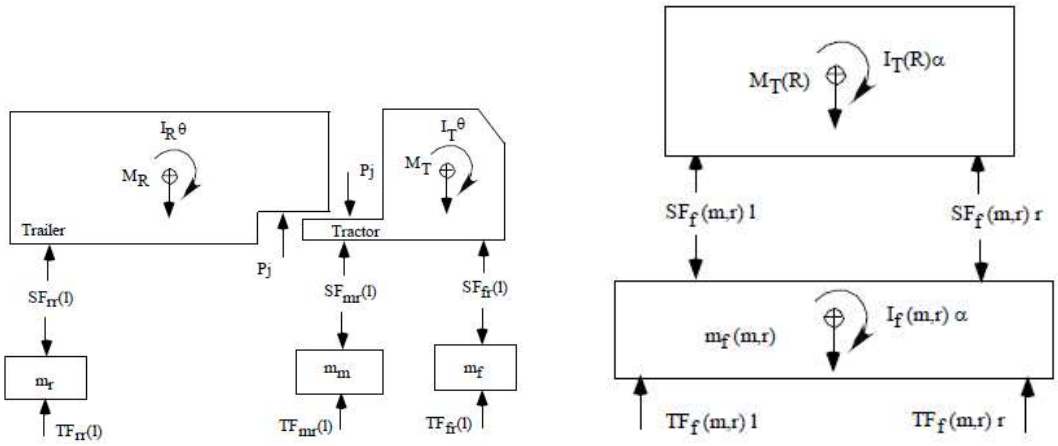

(a) Longitudinal Side View (b) Transverse Side View

Figure 3.9: Free Cody Diagram of Vehicle Model

(Liu, 1996)

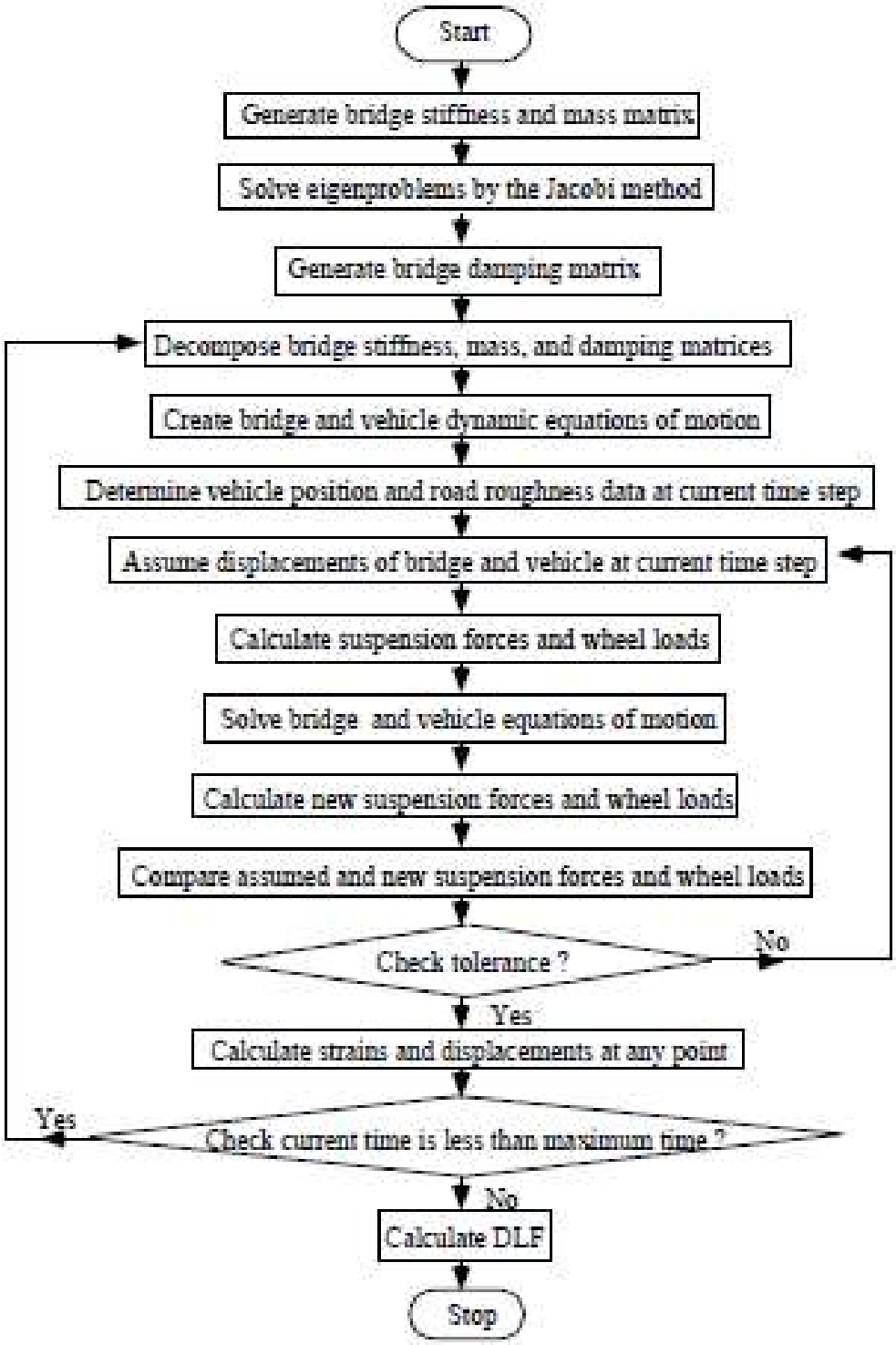

Figure 3.10: Flowchart of Computer Simulation Program

(Liu, 1996)

Chapter 4 Model Validation

4.1 Introduction

Validation can be defined as the cognitive process of establishing proof. Accurately analyzing and modeling a structure depends upon the chosen mathematical process and material properties. Models are not perfect, but 'validation' allows us to evaluate systems under circumstances that cannot be performed otherwise. In this study, one bridge will be calibrated with field data, and a similar approach will be applied to the remaining bridges.

4.2 Bridge Site

The original purpose of this analysis was to investigate the east fascia girder (B8) of the bridge, I-287 NB OVER US 202-206 (1815-154). NJDOT discovered that the east fascia girder was sagging up to 0.75 in., out of plum, and had collision scrapes. It was hypothesized that the girder was sagging due to its large overhang (60") and collision damage. The sagging girder has since been stabilized, but still requires interim inspections (monitoring) and further investigation.

4.3 Data Collection

The RIME performed sensor installation on Bridge 1815-154 on 10/16/2018 and 10/17/2018. The plan view sketch of the bridge is shown in Figure 4.1. The sensors were installed according to the plan view sketch shown in Figure 4.2. In total, there were eight long-term sensors and twenty short-term sensors installed, as shown in Table 4.1. The short-term sensors were removed after diagnostic load testing. The exact location of each sensor is shown in Figure 4.2. The detailed location of each sensor is shown in Figures 4.3 to 4.6.

Location Girder	North pier	Mid-span	South pier
B8 Bottom Flange	Tiltmeter	A1196 B1002	Tiltmeter
B9 Bottom Flange	Tiltmeter	A1197 B1001	Tiltmeter

Location Girder	¼ span	Mid-span	¾ span
B8 Web	B3680	B3683	B2060
B8 Bottom Flange	B2492	B3231 B3678 A3008	B2044
B9 Web	B2048	B2489	B3682
B9 Bottom Flange	B3219	B3227 B3689 A2125	B3238
B11 Bottom Flange	-	B2054 A3010	-
B14 Bottom Flange	-	B2485 A2124	-

Table 4.1: Identification of Sensors

4.3.1 I-287 Plan View Sketches

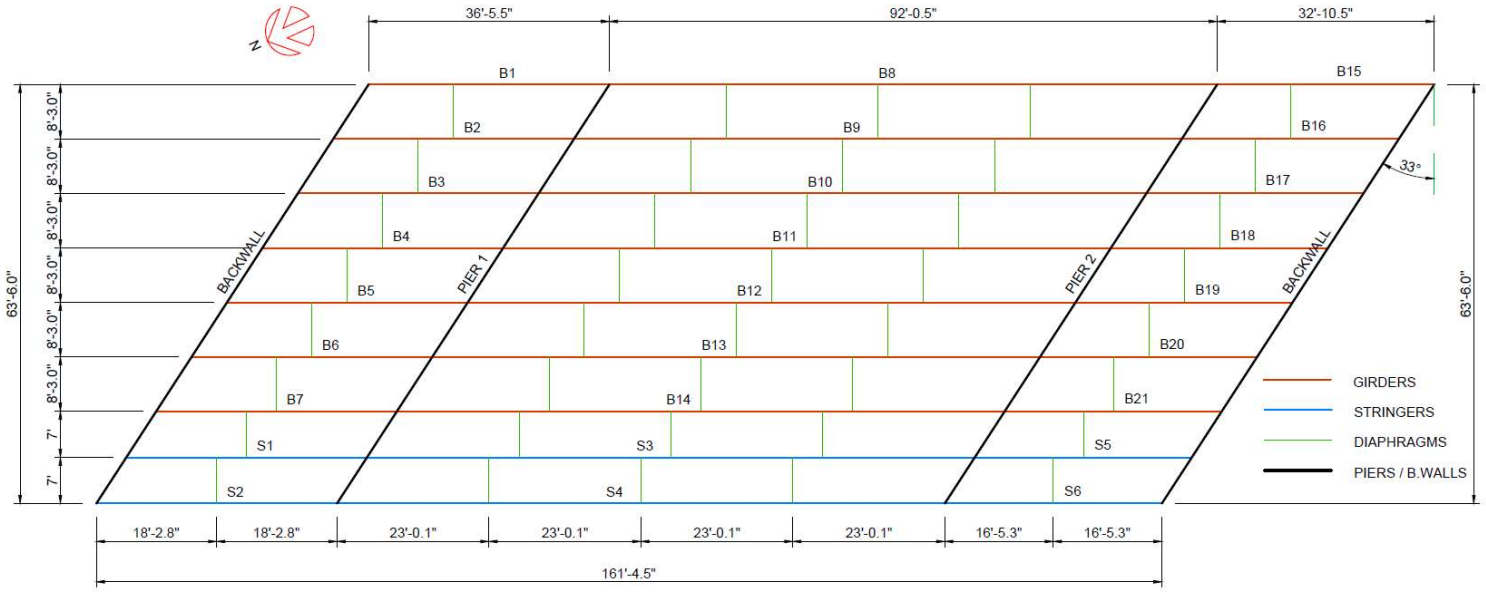

Figure 4.1: Bridge Plan View

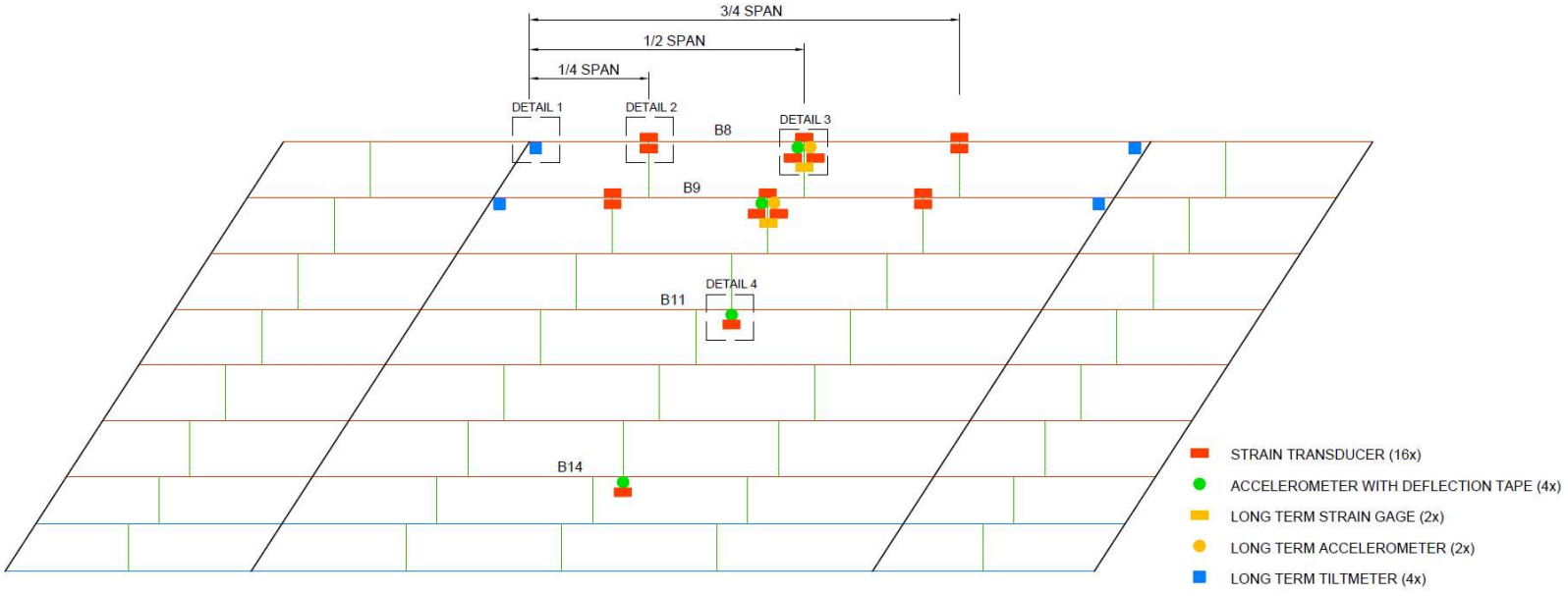

Figure 4.2: Installation Plan of Long-Term and Short-Term Sensor

4.3.2 I-287 Senor Details

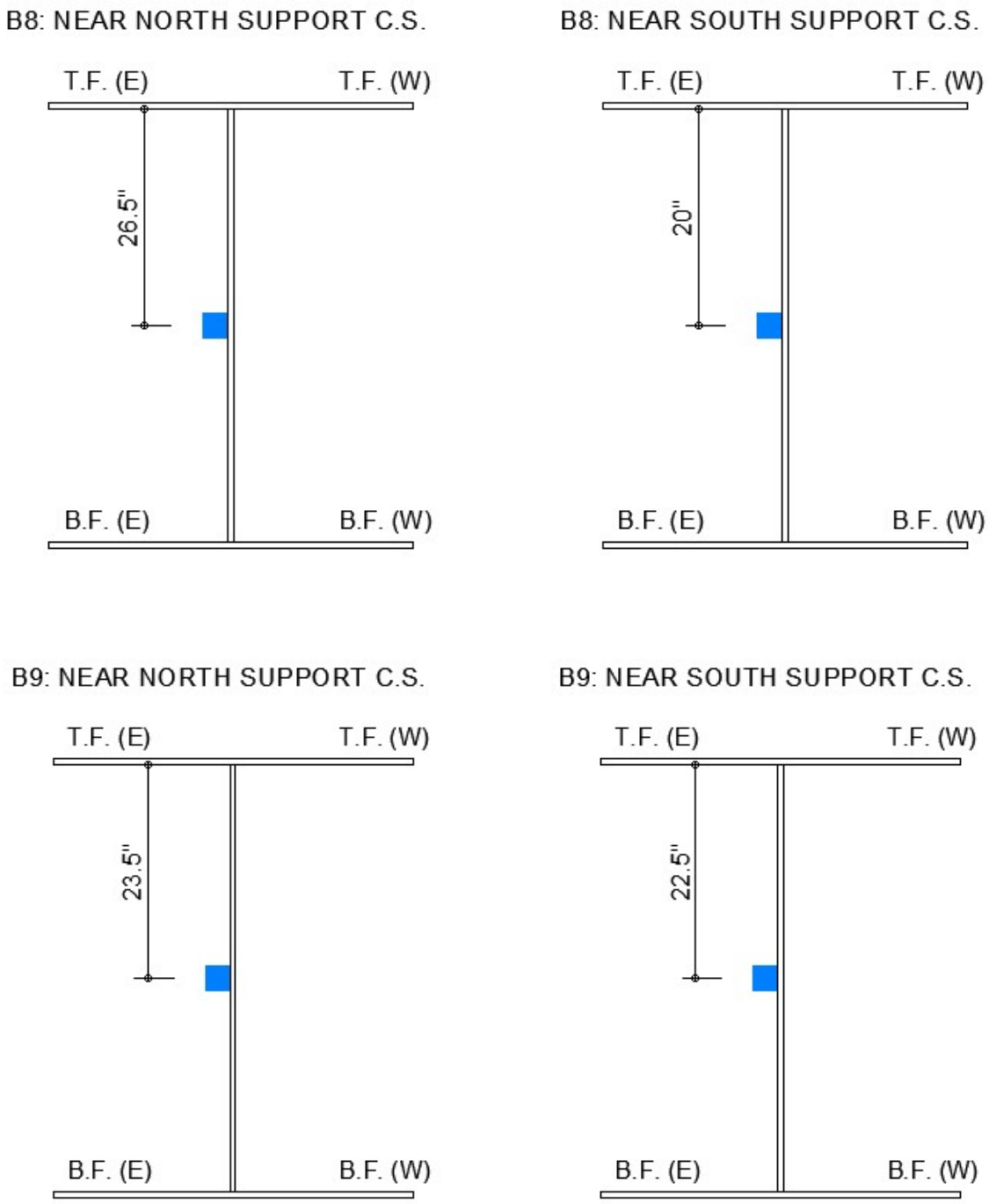

Figure 4.3: Detail 1- Location of Long-Term Tilt Meter near Support

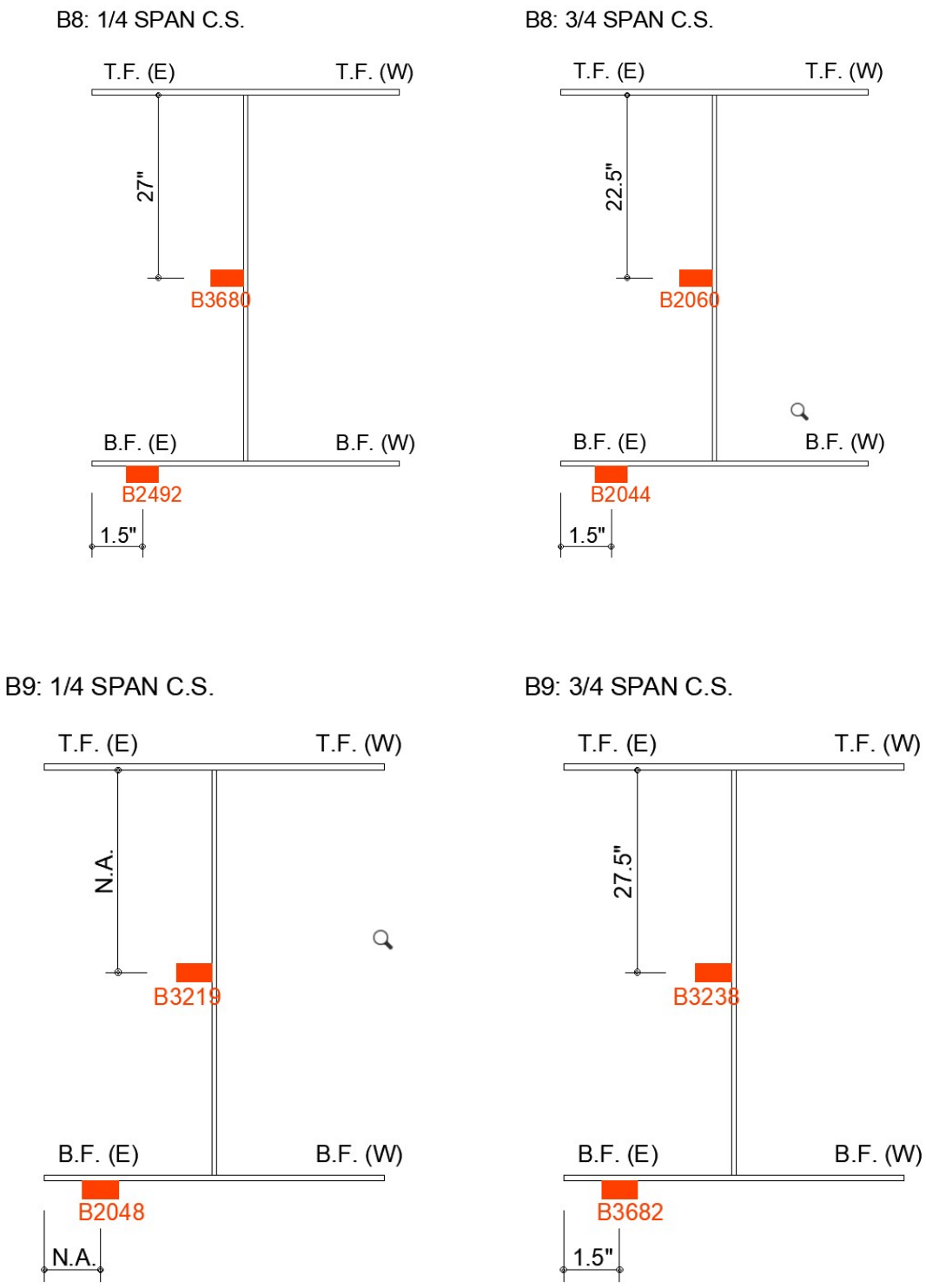

Figure 4.4: Detail 2- Location of Strain Transducer at 1/4 Span and 3/4 Span

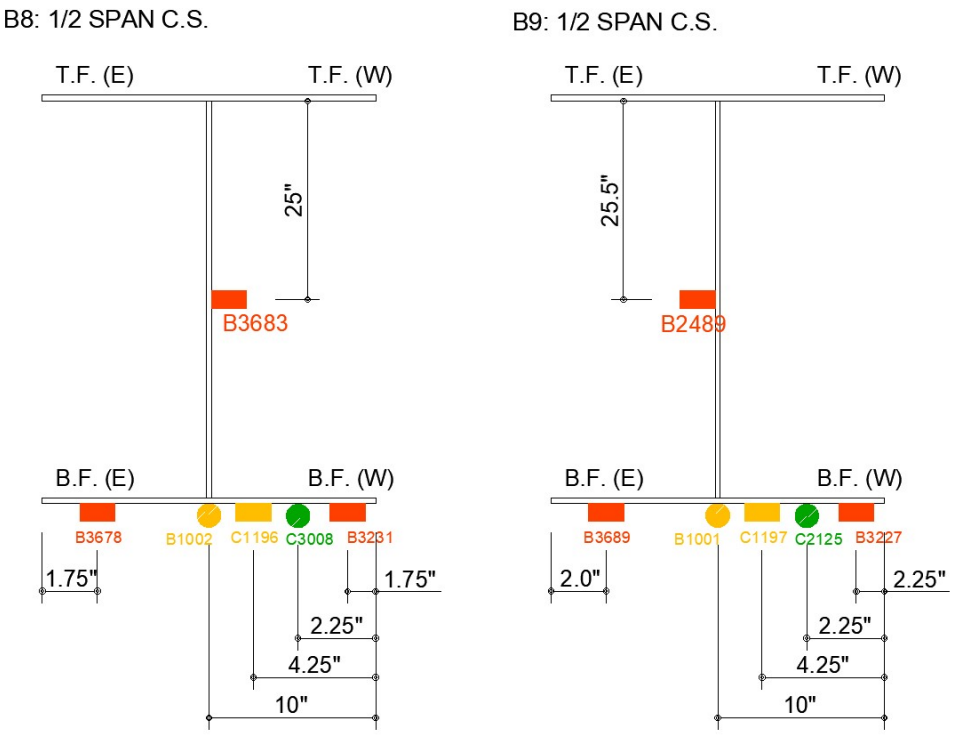

Figure 4.5.: Detail 3- Short-Term and Long-Term Sensors at Midspan

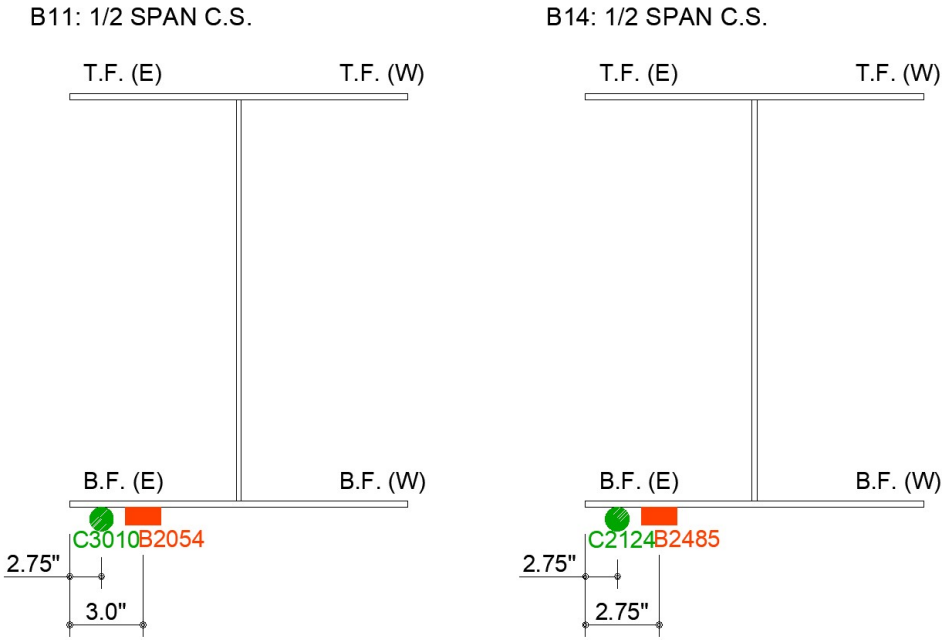

Figure 4.6: Detail 4-Short-Term Sensors at Midspan

Figure 4.7 shows the installation and setup for each type of sensor. All of the long-term sensors were covered with galvanized compounds, and their cables were led to the abutment from the inner side of the girder.

Short-Term Strain Sensor at The Bottom Flange

Short-Term Strain Sensor at The Middle Section

Short-Term Accelerometer Sensor and Deflection Tape

Long-Term Strain Gage (Poisson Gage)

Long-Term Accelerometer (Left)
and Covered Poisson Gage (Right)

Long-Term Tilt Meter

Figure 4.7: Sensor Installation and Setup

4.4 Testing Vehicle

The configuration of the test truck is shown in Figure 4.8. To model the test truck in Grillage, the back two tires had to be separated into two axles with a meniscal spacing of 0.1 in. due to Grillage only being able to model 5-Axle trucks.

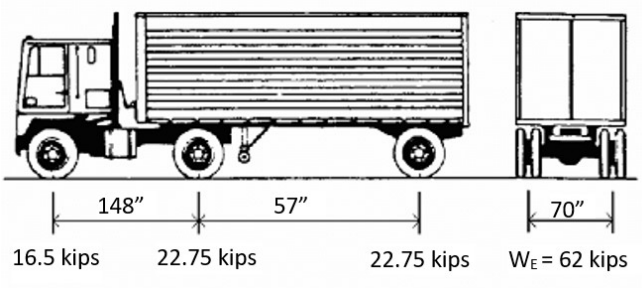

Figure 4.8: I-287 Test Truck

4.5 Diagnostic Testing

The diagnostic load testing was performed on 10/19/2018 to monitor the behavior of the sagging girder, and the calibration truck was designed to run in only path 1, path 2, and path 3 (See Figure 4.9).

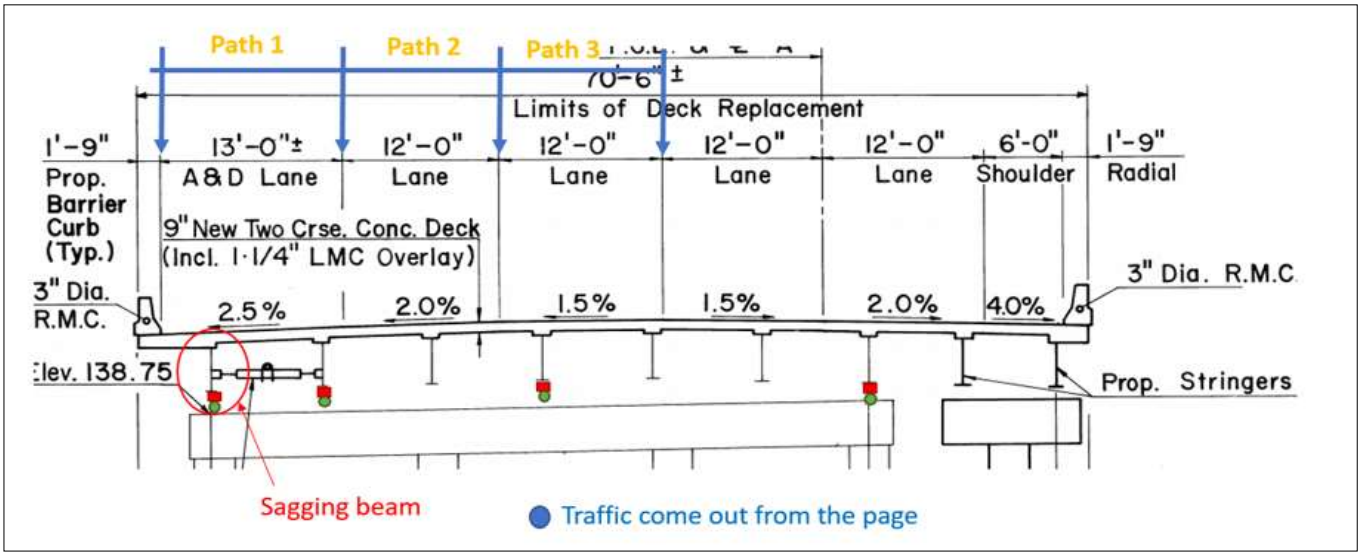

Figure 4.9: Diagnostic Load Testing Plan

Path No.	Speed	Run	Start Time	The time when the truck at mid-span (approximate)	LDV location
1	20	1_1	10:36	After 180 seconds	-
1	30	1_2	10:50-10:52	-	-
1	40	1_3	11:04	-	G1
1	20	1_4	11:20	-	G1
2	20	1_5	11:37	-	G2
2	40	1_6	11:50	-	G2
3	20	1_7	12:11	After 50seconds	G4
3	40	1_8	12:26	After 2 seconds	G4
1	20	1_9	12:41	After 95seconds	G1
1	20	1_10	12:57	-	G1

Table 4.2: Field Notes from Path 1 to Path 3

A typical short-term strain data is shown in Figure 4.10. The truck was running in path 1, sensor B3231, and sensor B3678 at the bottom flange captured the largest strain of 66 micro-strain.

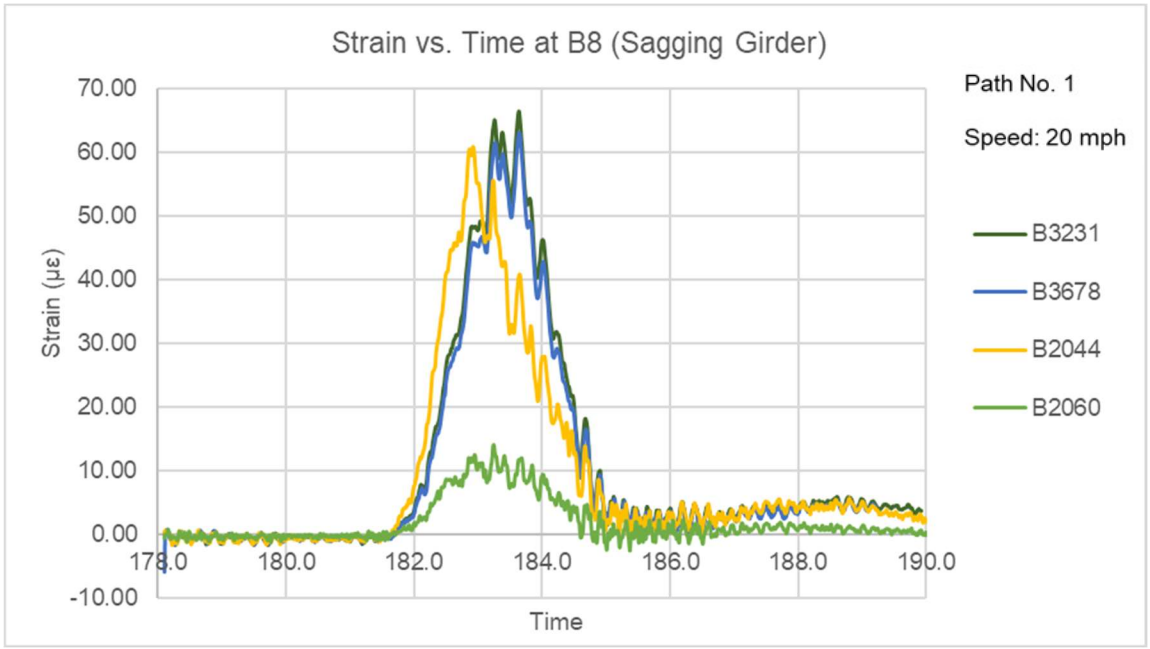

Figure 4.10: Typical Strain Data Results for Sagging Girder

The typical acceleration results are shown in Figure 4.11, where A3008 is the accelerometer at the sagging beam, and A2125 is the accelerometer at the adjacent beam.

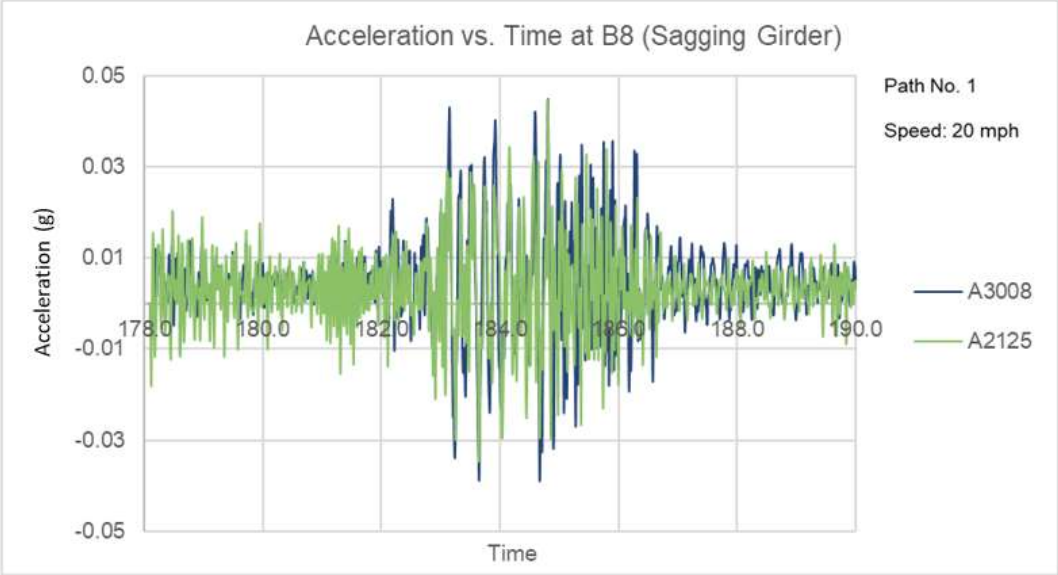

Figure 4.11: Typical Strain Data Results for Sagging Girder (B8)

The typical deflection results are shown in Figure 4.12. In the case 1_9, the LDV captured the maximum deflection of sagging girder with 5.3 centimeters (2.1 inches).

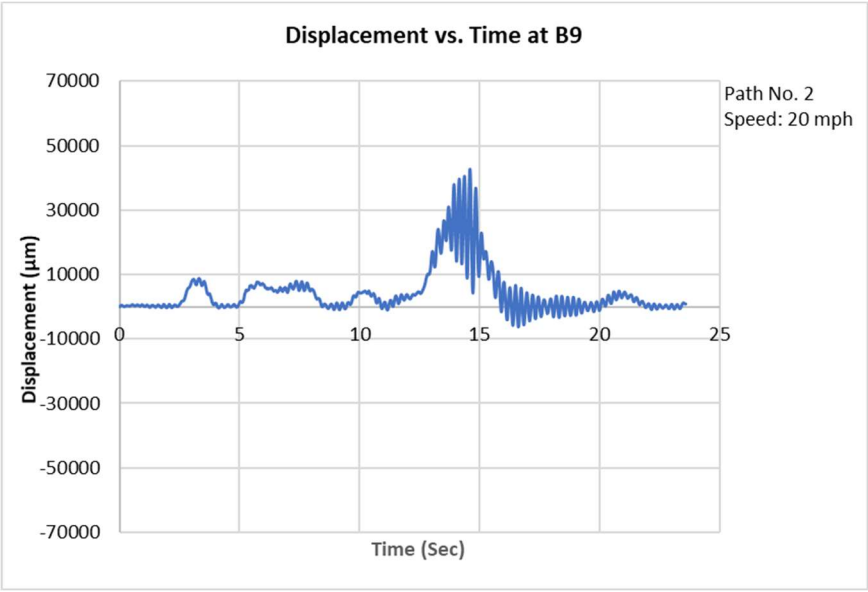

Figure 4.12: Typical deflection data from LDV

The strain values of the long-term sensors were compared with those of short-term sensors, as shown in Table 4.3. Two types of sensors were both installed at the bottom flange, and the maximum difference between them is 6.31 microstrain.

Path 2 (1_6)

	Short-term (με)			Long-term (με)
	B3231(exterior)	B3678(exterior)		B1002 (exterior)
11:51:04	46.77	44.14	11:50:55	46.26
	B3227(interior)	B3689(interior)		B1001 (interior)
	33.20	31.70		29.03

*There might be two truck, loads were superimposed

Path 2 (1_5)

	Short-term (με)			Long-term (με)
	B3231(exterior)	B3678(exterior)		B1002 (exterior)
11:36:59	35.06	37.53	11:36:50	33.40
	B3227(interior)	B3689(interior)		B1001 (interior)
	36.15	36.34		30.03

Table 4.3: Results Comparison between Long-Term and Short-Term Strain Sensors

Sensor Installation

Tilted Diaphragm under the Sagging Beam

Long-Term Sensor Operating System

Figure 4.13: Field Photos

4.6 Girder Cross-Sectional Properties (Plans)

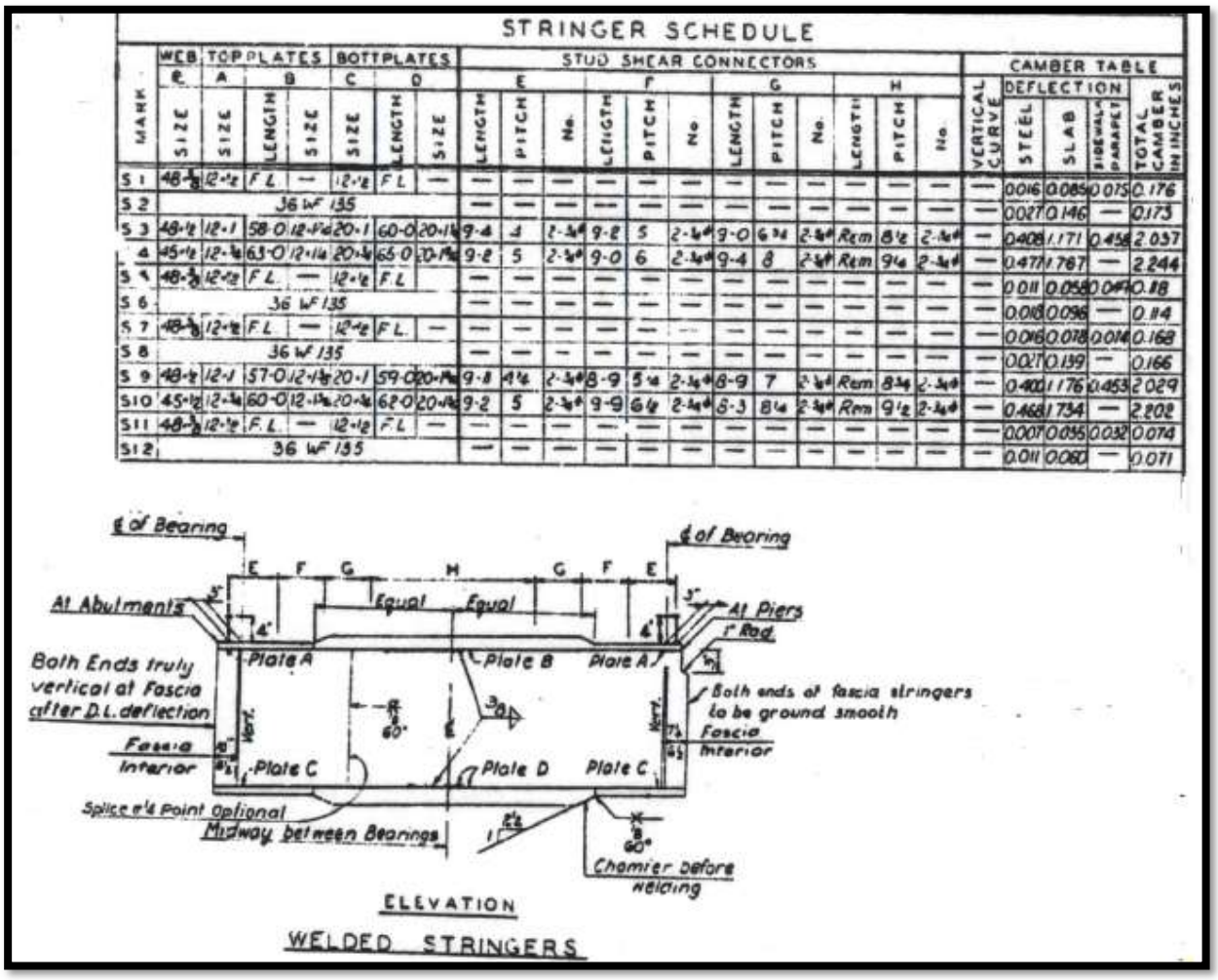

STRINGER SCHEDULE

MARK	WEB ℄ SIZE	TOP PLATES A SIZE	TOP PLATES B LENGTH	TOP PLATES B SIZE	BOTT PLATES C SIZE	BOTT PLATES D LENGTH	BOTT PLATES D SIZE	STUD SHEAR CONNECTORS E LENGTH	E PITCH	E No.	F LENGTH	F PITCH	F No.	G LENGTH	G PITCH	G No.	H LENGTH	H PITCH	H No.	VERTICAL CURVE	CAMBER TABLE DEFLECTION STEEL	DEFLECTION SLAB	DEFLECTION SIDEWALK PARAPET	TOTAL CAMBER IN INCHES
S1	48-½	12-½	F.L.	—	12-½	F.L.	—	—	—	—	—	—	—	—	—	—	—	—	—	—	0.016	0.085	0.075	0.176
S2	36 WF 135							—	—	—	—	—	—	—	—	—	—	—	—	—	0.027	0.146	—	0.173
S3	48-½	12-1	58-0	12-1⅝	20-1	60-0	20-1⅛	9-4	4	2-¾#	9-2	5	2-¾#	9-0	6¾	2-¾#	Rem	8½	2-¾#	—	0.408	1.171	0.458	2.037
4	45-½	12-¾	63-0	12-1⅛	20-¾	65-0	20-1⅝	9-2	5	2-¾#	9-0	6	2-¾#	9-4	8	2-¾#	Rem	9¼	2-¾#	—	0.477	1.767	—	2.244
S5	48-⅜	12-½	F.L.	—	12-½	F.L.		—	—	—	—	—	—	—	—	—	—	—	—	—	0.011	0.058	0.049	0.118
S6	36 WF 135							—	—	—	—	—	—	—	—	—	—	—	—	—	0.018	0.096	—	0.114
S7	48-⅜	12-½	F.L.	—	12-½	F.L.	—	—	—	—	—	—	—	—	—	—	—	—	—	—	0.016	0.078	0.074	0.168
S8	36 WF 135							—	—	—	—	—	—	—	—	—	—	—	—	—	0.027	0.139	—	0.166
S9	48-½	12-1	57-0	12-1⅜	20-1	59-0	20-1⅛	9-8	4¼	2-¾#	8-9	5¼	2-¾#	8-9	7	2-¾#	Rem	8¾	2-¾#	—	0.401	1.176	0.453	2.029
S10	45-½	12-¾	60-0	12-1⅜	20-¾	62-0	20-1⅛	9-2	5	2-¾#	9-9	6¼	2-¾#	8-3	8¼	2-¾#	Rem	9½	2-¾#	—	0.468	1.734	—	2.202
S11	48-⅜	12-½	F.L.	—	12-½	F.L.	—	—	—	—	—	—	—	—	—	—	—	—	—	—	0.007	0.035	0.032	0.074
S12	36 WF 135							—	—	—	—	—	—	—	—	—	—	—	—	—	0.011	0.060	—	0.071

Figure 4.14: Original Girders (B8-B14) Cross-Sectional Properties

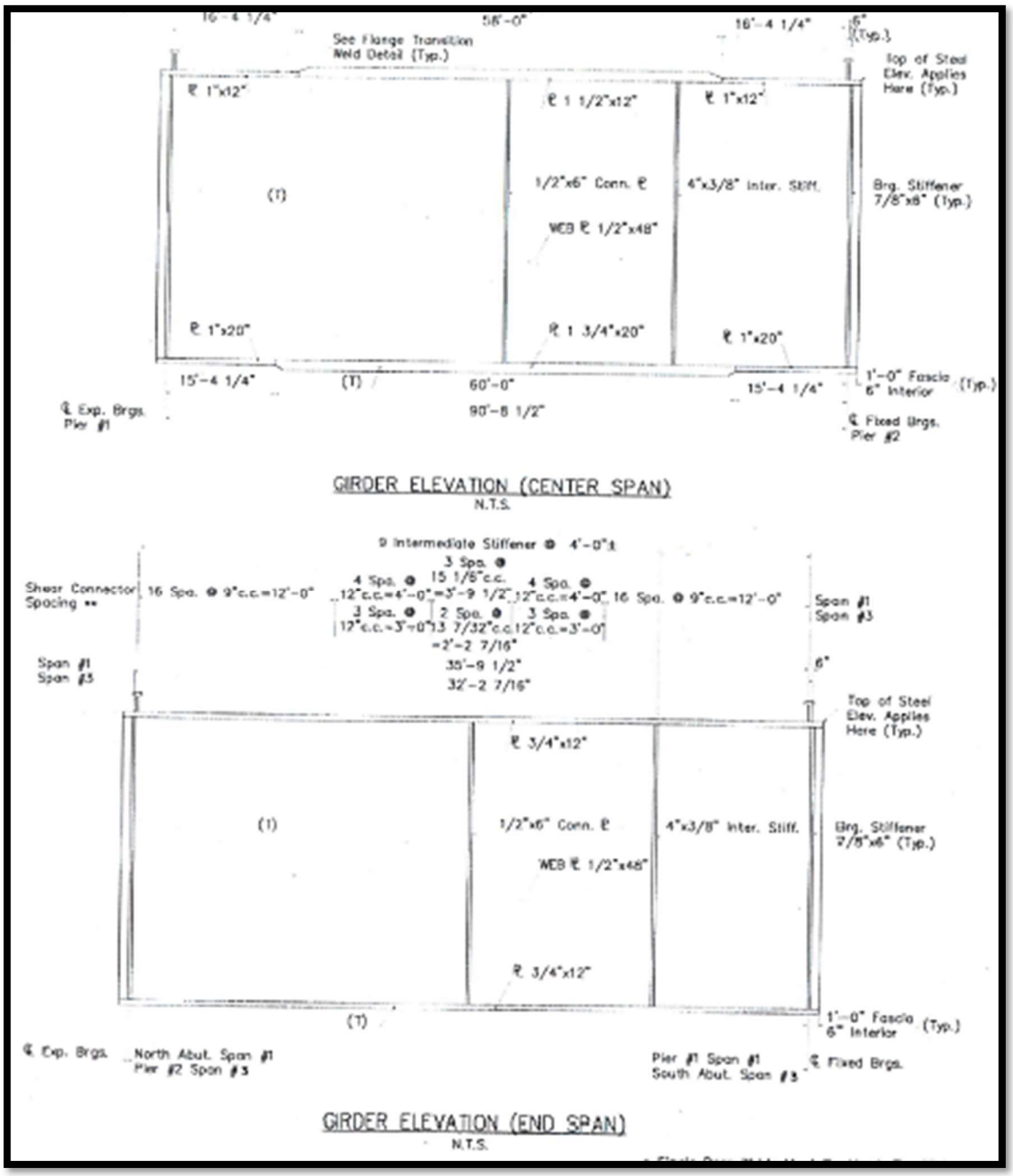

Figure 4.15: Widening Stringers (S3 & S4) Cross-Sectional Properties

4.7 I-287 Bridge Model

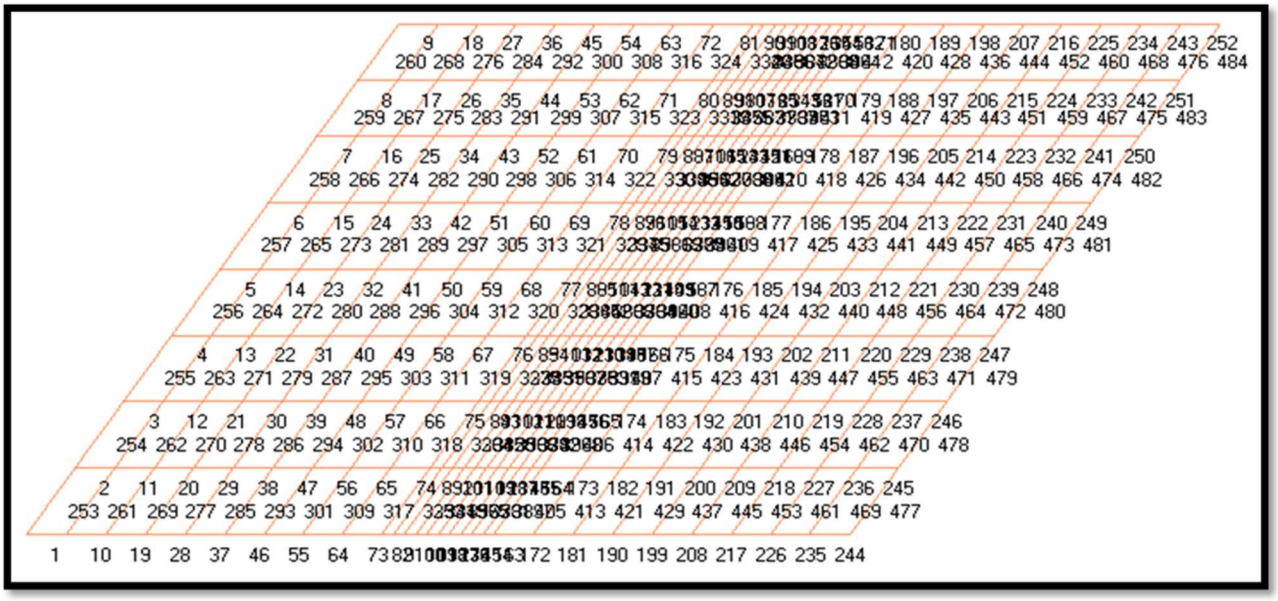

Figure 4.16: I-287 Grillage Output Grid

	Longitudinal Elements																										
99 in.	9	18	27	36	45	54	63	72	81	90	99	108	117	126	135	144	153	162	171	180	189	198	207	216	225	234	243	252	Exterior w/ Overhang
99 in.	8	17	26	35	44	53	62	71	80	89	98	107	116	125	134	143	152	161	170	179	188	197	206	215	224	233	242	251	
99 in.	7	16	25	34	43	52	61	70	79	88	97	106	115	124	133	142	151	160	169	178	187	196	205	214	223	232	241	250	
99 in.	6	15	24	33	42	51	60	69	78	87	96	105	114	123	132	141	150	159	168	177	186	195	204	213	222	231	240	249	
99 in.	5	14	23	32	41	50	59	68	77	86	95	104	113	122	131	140	149	158	167	176	185	194	203	212	221	230	239	248	
99 in.	4	13	22	31	40	49	58	67	76	85	94	103	112	121	130	139	148	157	166	175	184	193	202	211	220	229	238	247	
84 in.	3	12	21	30	39	48	57	66	75	84	93	102	111	120	129	138	147	156	165	174	183	192	201	210	219	228	237	246	
84 in.	2	11	20	29	38	47	56	65	74	83	92	101	110	119	128	137	146	155	164	173	182	191	200	209	218	227	236	245	
	1	10	19	28	37	46	55	64	73	82	91	100	109	118	127	136	145	154	163	172	181	190	199	208	217	226	235	244	Exterior w/ Overhang
	53 in.	53 in	53 in.	53 in.	53 in.	53 in.	53 in.	53 in.	53 in.	15 in.	15 in.	15 in.	15 in.	15 in.	15 in.	15 in.	15 in.	15 in.	15 in.	53 in.	53 in.	53 in.	53 in.	53 in.	53 in.	53 in.	53 in.	53.5 in.	
	Transverse Elements																												
99 in.	260	268	276	284	292	300	308	316	324	332	340	348	356	364	372	380	388	396	404	412	420	428	436	444	452	460	468	476	484
99 in.	259	267	275	283	291	299	307	315	323	331	339	347	355	363	371	379	387	395	403	411	419	427	435	443	451	459	467	475	483
99 in.	258	266	274	282	290	298	306	314	322	330	338	346	354	362	370	378	386	394	402	410	418	426	434	442	450	458	466	474	482
99 in.	257	265	273	281	289	297	305	313	321	329	337	345	353	361	369	377	385	393	401	409	417	425	433	441	449	457	465	473	481
99 in.	256	264	272	280	288	296	304	312	320	328	336	344	352	360	368	376	384	392	400	408	416	424	432	440	448	456	464	472	480
99 in.	255	263	271	279	287	295	303	311	319	327	335	343	351	359	367	375	383	391	399	407	415	423	431	439	447	455	463	471	479
84 in.	254	262	270	278	286	294	302	310	318	326	334	342	350	358	366	374	382	390	398	406	414	422	430	438	446	454	462	470	478
84 in.	253	261	269	277	285	293	301	309	317	325	333	341	349	357	365	373	381	389	397	405	413	421	429	437	445	453	461	469	477
		53 in.	53 in	53 in.	53 in.	53 in.	53 in.	53 in.	53 in.	53 in.	15 in.	15 in.	15 in.	15 in.	15 in.	15 in.	15 in.	15 in.	15 in.	15 in.	53 in.	53 in.	53 in.	53 in.	53 in.	53 in.	53 in.	53 in.	53.5 in.

Figure 4.17: I-287 Grillage Grid Properties

4.8 Model Assumptions/Idealizations

Several assumptions were used when calibrating the grillage model with the test data:

1. No information was taken in the field regarding the exact position of the test truck in the lane for each run. The truck was assumed to be located at the center of each lane. Additionally, the model started the truck movement approximately 100 inches behind the start of the bridge, to allow the vehicle's suspension system to develop its dynamic response fully.
2. Barriers increase the overall stiffness of the superstructure and play a role in reducing bridge deflections. For this model, the barrier mass and stiffness were linearly added to the exterior girder's mass and stiffness. This approach is reasonable considering the relatively wide girder spacing (8' -3"), any effects on the first interior girder would be negligible.
3. The overlay thickness was included as part of the deck's mass and stiffness. From a mass perspective, this assumption is valid. However, assuming the overlay is fully composite with the precast deck panels could be considered disputable. Based on preliminary model trial runs, there is some degree of composite action between the deck and overlay. Applying this assumption into the model increased the accuracy of the results, and will therefore remain.
4. To limit the amount of modeling required, only the test runs for Path 3 with girder B11 was used for calibration purposes. It was assumed that running the truck in the opposite direction would produce very similar results due to the symmetry of the structure.
5. Test run paths 1 and 2 were not used due to limitations of Grillage modeling large overhangs. The I-287 bridge has a large overhang (60"), which cannot be fully captured in Grillage and would result in the truck's left wheel being off the model for proper placement.
6. Limited details were provided for how the precast deck panels were connected to the girders. It was assumed shear stud pockets were provided and grouted during construction, effectively making the section composite. The model assumes a 100% composite action between the slab and girders.
7. The structure was assumed to have 2% damping.

   Randomly generated road roughness profiles were used.

4.9 Dynamic Model Validation

The experimental field data and grillage model produced very close strain measurements for girder B11 with the test truck running in Path 3, going 20 mph (See Figure 4.18). Limited field data was provided for the remaining parameters, but reasonable results were produced from Grillage for stress, deflection, velocity, and acceleration (See Figure 4.19).

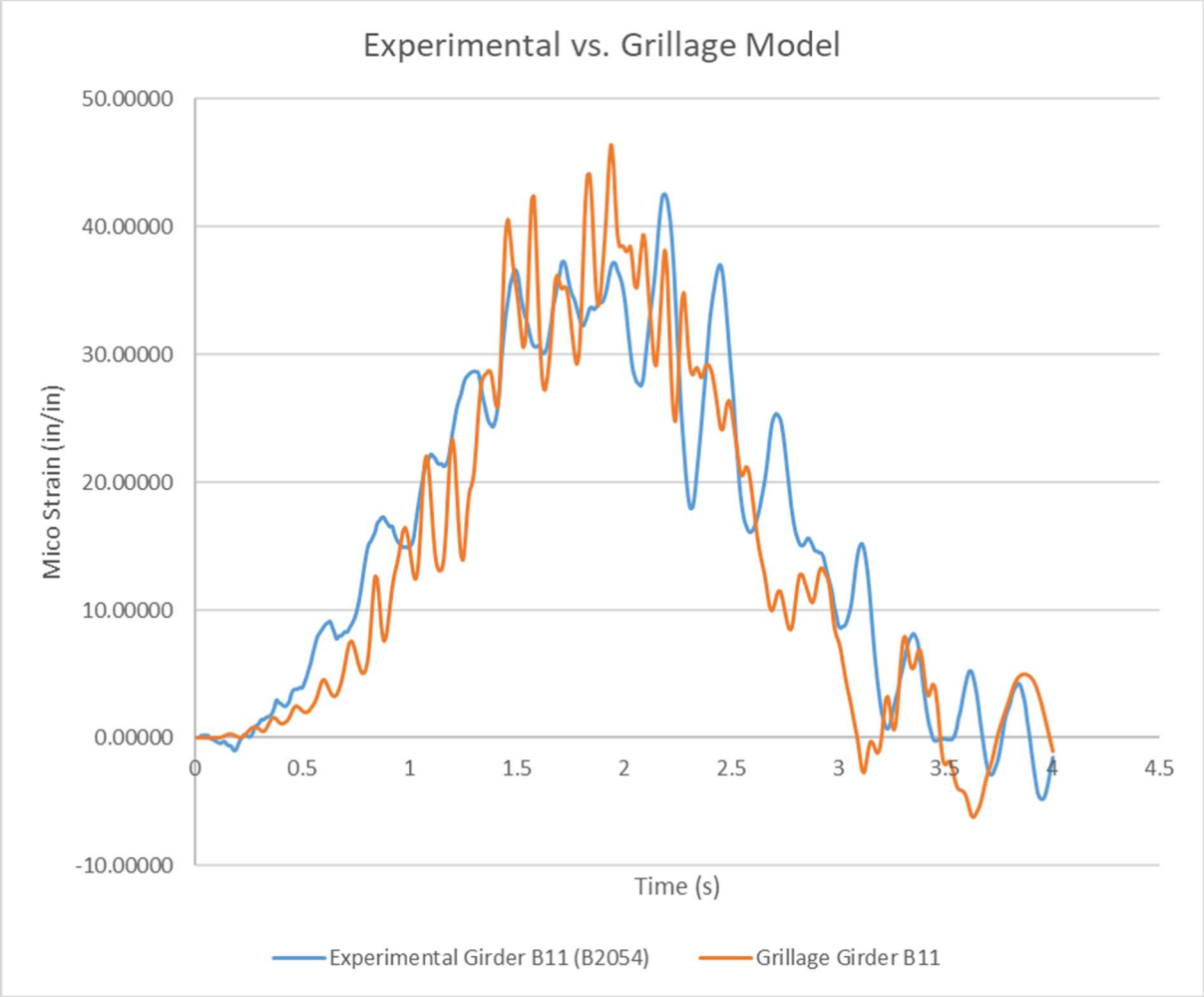

Figure 4.18: Experimental Strain vs. Grillage Model Strain

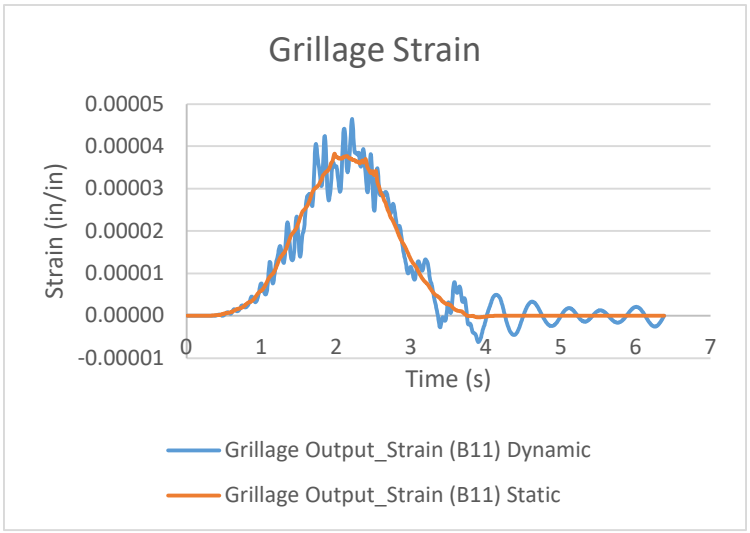

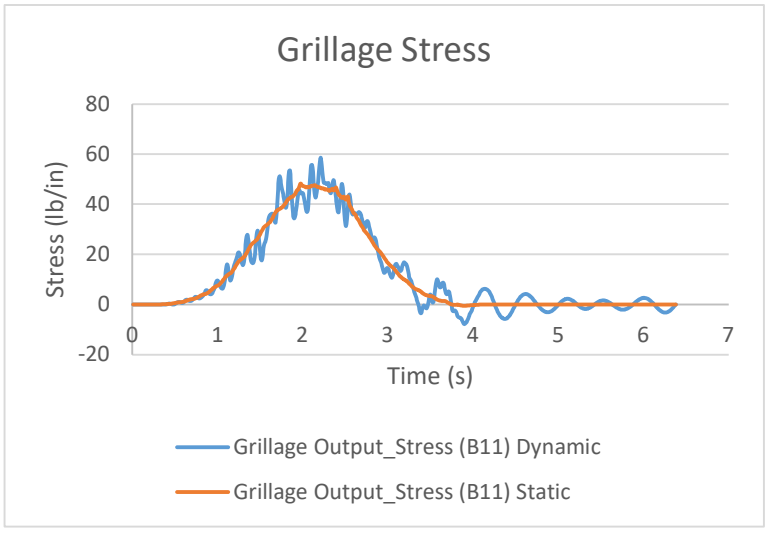

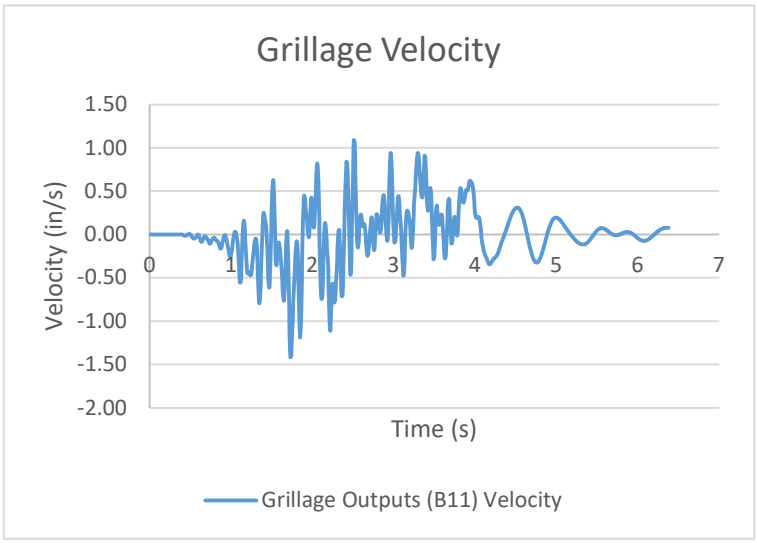

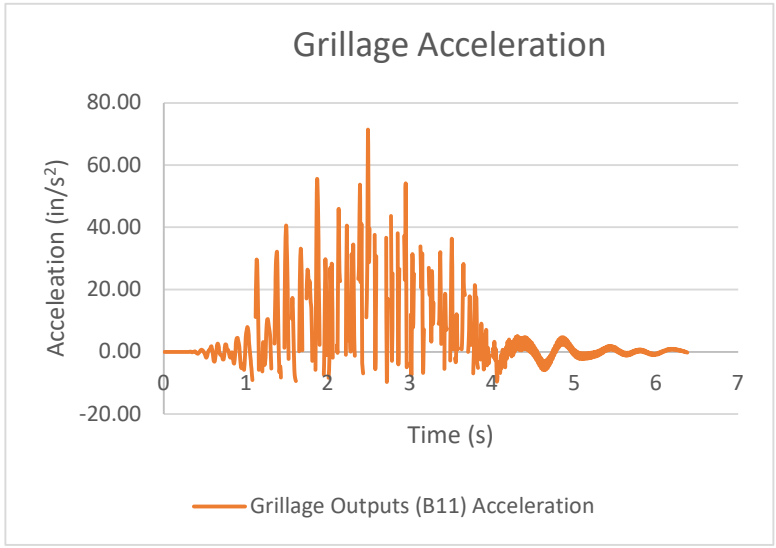

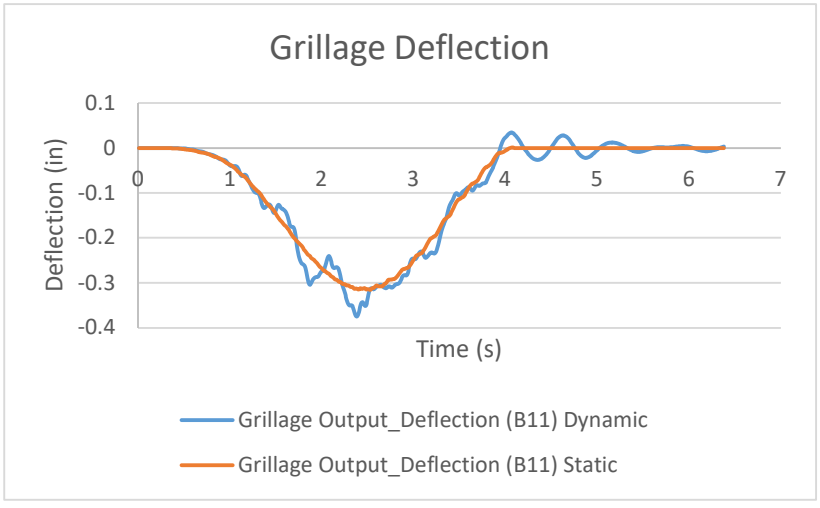

Figure 4.19: I-287 Grillage Calibrated Results

Chapter 5: Parametric Study

This chapter discusses the parametric study used to compare the AASHTO deflection limit to bridge acceleration responses. Five simply supposed steel bridges will be modified to see the impact on deflection and acceleration. Deck thickness, the density of concrete, and girder size will be investigated.

5.1 Bridges

All five bridges are located in New Jersey with various span lengths and superstructure designs. Since AASHTO's deflection limits are solely based on span length, span lengths will remain constant. Natural frequency plays a significant role in a bridge's vibration response, but it is very difficult to capture, especially in the design phase. Modifying the specified parameters will highlight possible limitations of the AASHTO deflection limit under different circumstances.

5.1.1 Roadway Data

Name	River Road (East) over Tributary to North Branch Raritan River (Clucas Brook)	Willow Grove Road over Pohatcong Creek	I-287 NB over US 202-206	NJ 18 NB over Wayside Road (CO. RT. 38)	I-295 SB Over US 1 & Ramps "A" (from I-295 NB to US 1 SB & I-295 SB) & "B" (from US 1 NB to I-295 NB)
Span Length	29	69	92	126	175
Span Width	32.5	32.8	70.5	48.4	61.4
Location	Bedminister Township Somerset County	Franklin Township Warren County	Bedminister Township Somerset County	Tinton Falls Borough Monmouth County	Lawrence Township Mercer County
Function Class	Rural (Local)	Rural (Local)	Urban-Principal Arterial (Interstate)	Urban-Principal Arterial (Other Freeway or Expressway)	Urban-Principal Arterial (Interstate)
ADT	500	565	42396	18565	44750
ADTT (%)	3	3	9	5	9
Year Build	2014	2000	1965	1979	1974

Table 5.1: Roadway Data of Bridges

5.1.2 Deflection and Vibration Data

Perceived deflection and vibration data were extracted from NJDOT bridge inspection reports for the selected structures. There are no criteria for categorizing bridge deflection and vibration beyond the bridge inspector's sensitivity. Below are the most recent recorded results for the selected structures.

Span Length	**Deflection and Vibration Remarks**
175 FT.	Noticeable with heavy trucks.
126 FT.	Moderate vibration under heavy trucks.
92 FT.	Vibration observed under heavy trucks and minor deflection.
69 FT.	Minor vibration under heavy trucks.
29 FT.	None noticed.

Table 5.2: Perceived Deflection and Vibration Data

5.1.3 Elevation Photos

29 FT Span

69 FT Span

92 FT Span

126 FT Span

175 FT Span

Figure 5.1: Bridge Elevation Views

5.1.4 Deck Cross Section Sketches

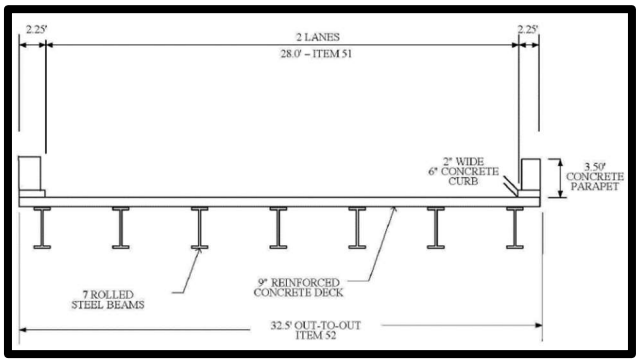

29 FT Span

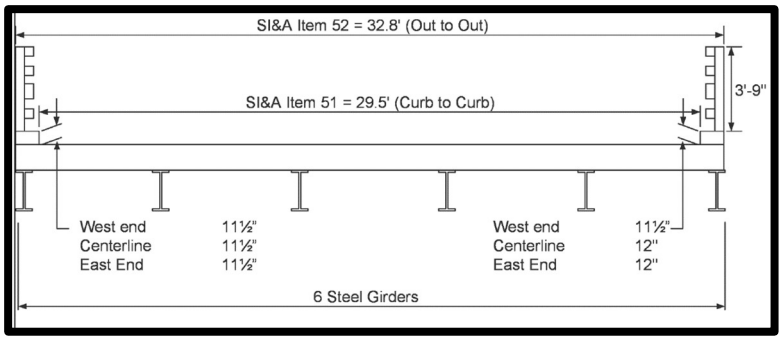

69 FT Span

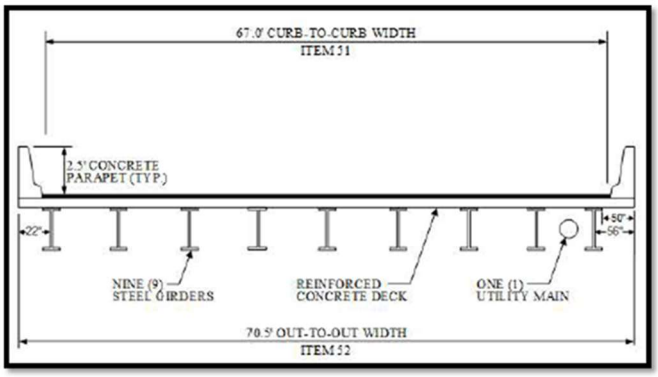

92 FT Span

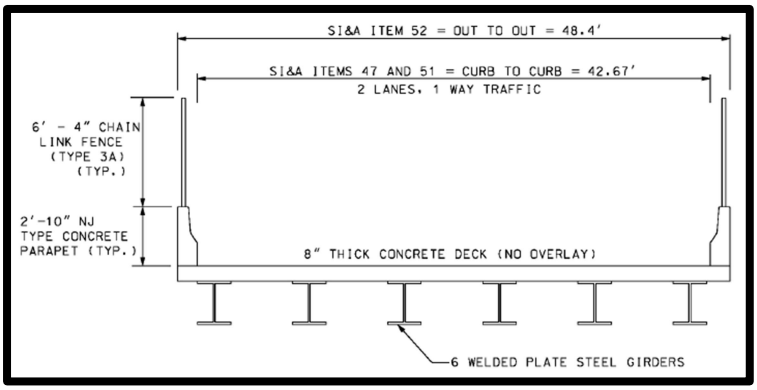

126 FT Span

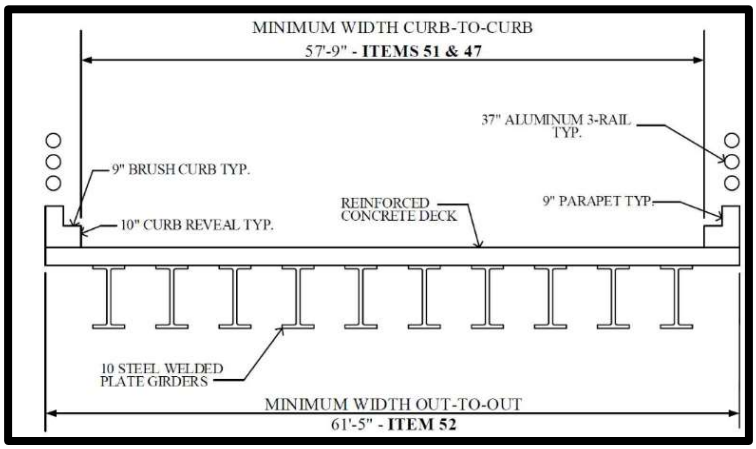

175 FT Span

Figure 5.2: Deck Cross Section Sketches

5.1.5 Grillage Models

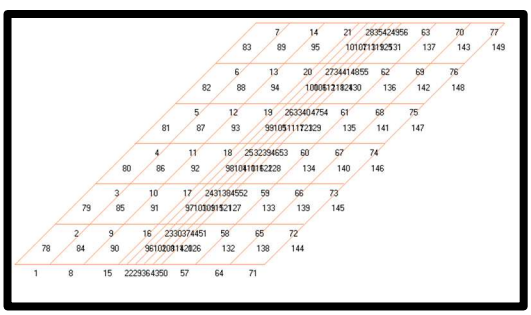

29 FT Span

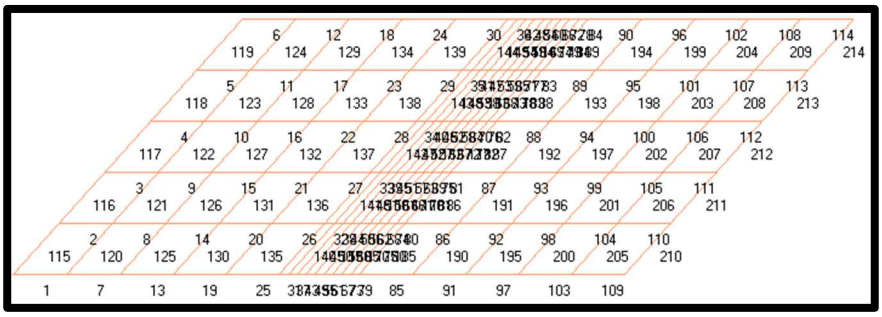

69 FT Span

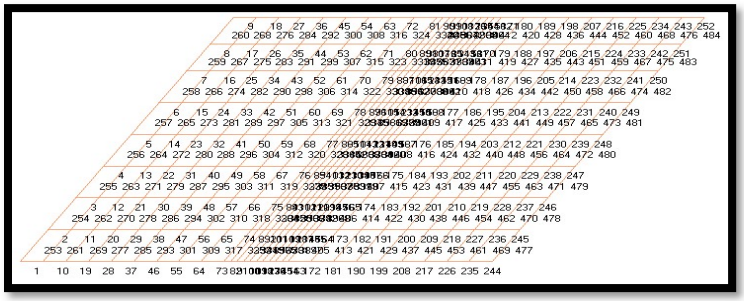

92 FT Span

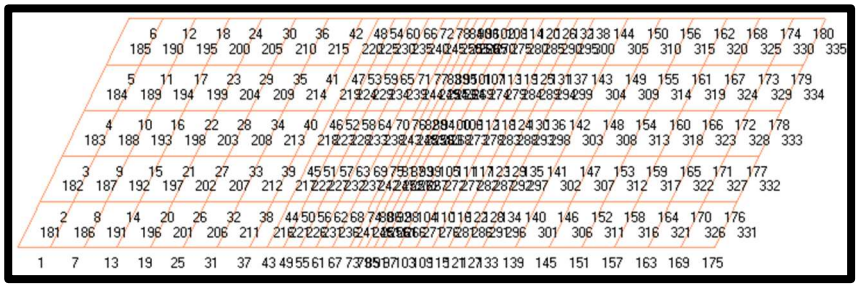

126 FT Span

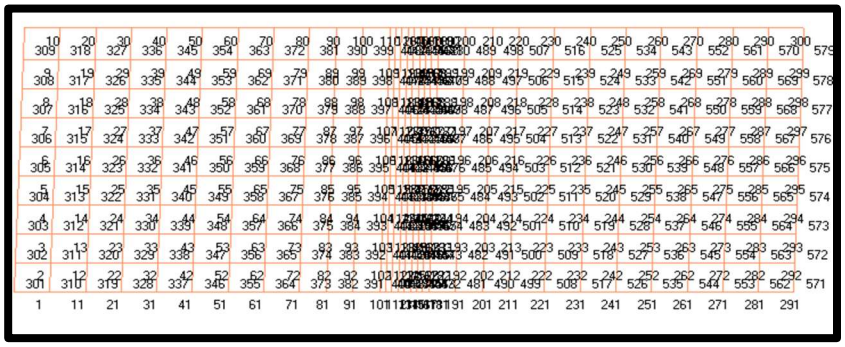

175 FT Span

Figure 5.3: Grillage Gird Models

5.2 Test Vehicle

The configuration of the test truck (HS20: V=14 ft.) is shown in Figure 5.4. To model the test truck in Grillage, the back two tires had to be separated into two axles with a meniscal spacing of 0.1 in. due to Grillage only being able to model 5-Axle trucks. This test truck was used throughout each test at a speed of 60 mph.

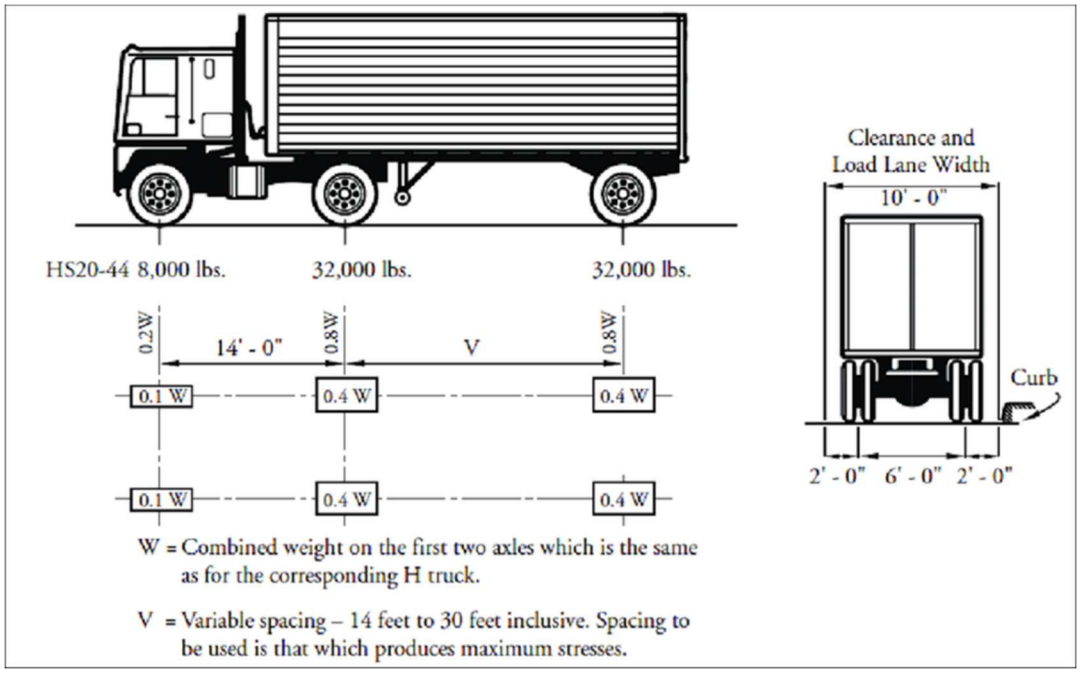

Figure 5.4: Grillage Test Vehicle (HS20)

5.3 Deck Thickness Data

Each bridge was modeled as designed (9 in. deck) and then remodeled with and an extra inch of the deck (10 in., 11 in., and 12 in.) to see the effects on deflection and acceleration. Continuously increasing the thickness of the deck limited deflection and acceleration. The shorter spans exhibited a greater decrease in deflection than the longer spans. All of the spans were under the 100 in/s^2 acceleration limit, except for the 29 ft. Span, most likely due to its low mass and natural frequency. Furthermore, the 29 ft. Span exhibited significantly less deflection due to one axle loading the structure at a time, which probably amplified the acceleration as well. Nevertheless, the 29 ft. Span did not have noticeable vibrations, which leads to the notion that extremely low deflection coupled with extremely high acceleration, do not result in "unpleasant" vibrations.

Deck Thickness Data (Deflection) Summary

	29 FT Span		69 FT Span		92 FT Span		126 FT Span		175 FT Span	
Deck Thickness (in.)	Max Deflection (in)	Max Deflection Change	Max Deflection (in)	Max Deflection Change	Max Deflection (in)	Max Deflection Change	Max Deflection (in)	Max Deflection Change	Max Deflection (in)	Max Deflection Change
9 in. (Original)	-0.023337	-	-0.159295	-	-0.0853	-	-0.158138	-	-0.184660	-
10 in.	-0.020647	-11.53%	-0.144320	-9.40%	-0.0790	-7.38%	-0.149825	-5.26%	-0.176271	-4.54%
11 in.	-0.018274	-21.70%	-0.130822	-17.87%	-0.0734	-13.94%	-0.141669	-10.41%	-0.169281	-8.33%
12 in.	-0.016190	-30.63%	-0.118838	-25.40%	-0.0683	-19.87%	-0.135312	-14.43%	-0.162531	-11.98%

Table 5.3: Deck Thickness (Deflection) Summary

Deck Thickness Data (Acceleration) Summary

	29 FT Span		69 FT Span		92 FT Span		126 FT Span		175 FT Span	
Deck Thickness (in.)	Absolute Max Acceleration (in/s^2)	Absolute Max Acceleration Change	Absolute Max Acceleration (in/s^2)	Absolute Max Acceleration Change	Absolute Max Acceleration (in/s^2)	Absolute Max Acceleration Change	Absolute Max Acceleration (in/s^2)	Absolute Max Acceleration Change	Absolute Max Acceleration (in/s^2)	Absolute Max Acceleration Change
9 in. (Original)	222.594098	-	65.149259	-	75.8598	-	63.529785	-	53.5184	
10 in.	204.913705	-7.94%	57.632376	-11.54%	73.4847	-3.13%	56.923330	-10.40%	50.7300	-5.21%
11 in.	200.649485	-9.86%	52.214275	-19.85%	65.9324	-13.09%	57.121820	-10.09%	45.1887	-15.56%
12 in.	180.779477	-18.79%	47.447600	-27.17%	59.7226	-21.27%	56.027167	-11.81%	42.4011	-20.77%

Table 5.4: Deck Thickness (Acceleration) Summary

AVERAGE		
Deck Thickness (in.)	**Max Deflection Change**	**Absolute Max Acceleration Change**
9 in. (Original)	-	-
10 in.	-7.62%	-7.64%
11 in.	-14.45%	-13.69%
12 in.	-20.46%	-19.96%

Table 5.5: Deck Thickness Average Change Summary

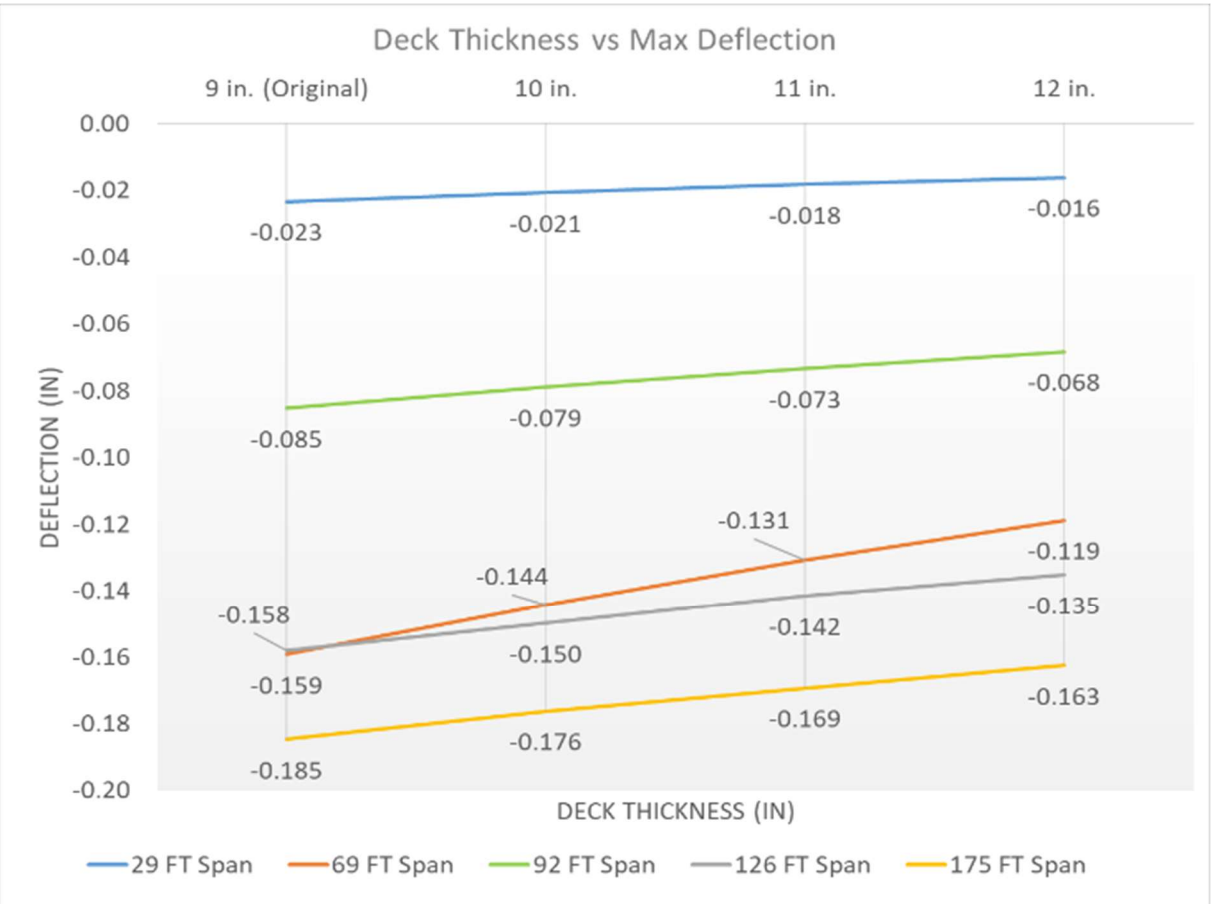

Figure 5.5: Deck Thickness vs. Max Deflection

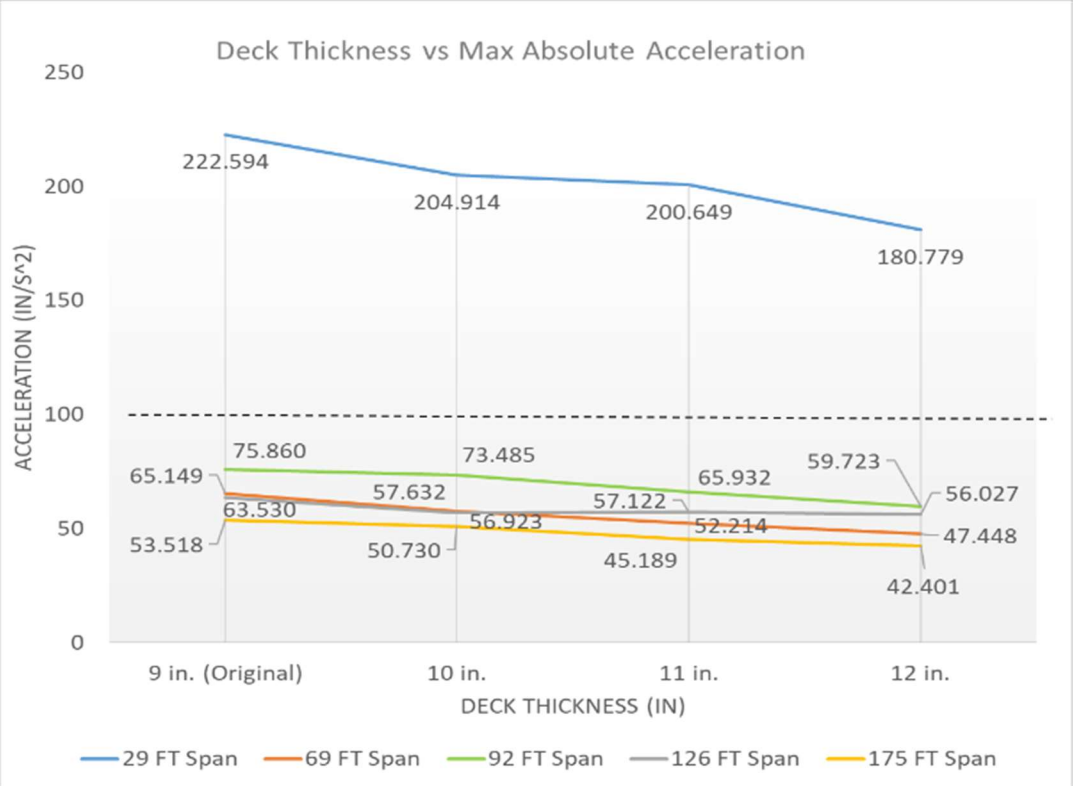

Figure 5.6: Deck Thickness vs. Absolute Max Acceleration

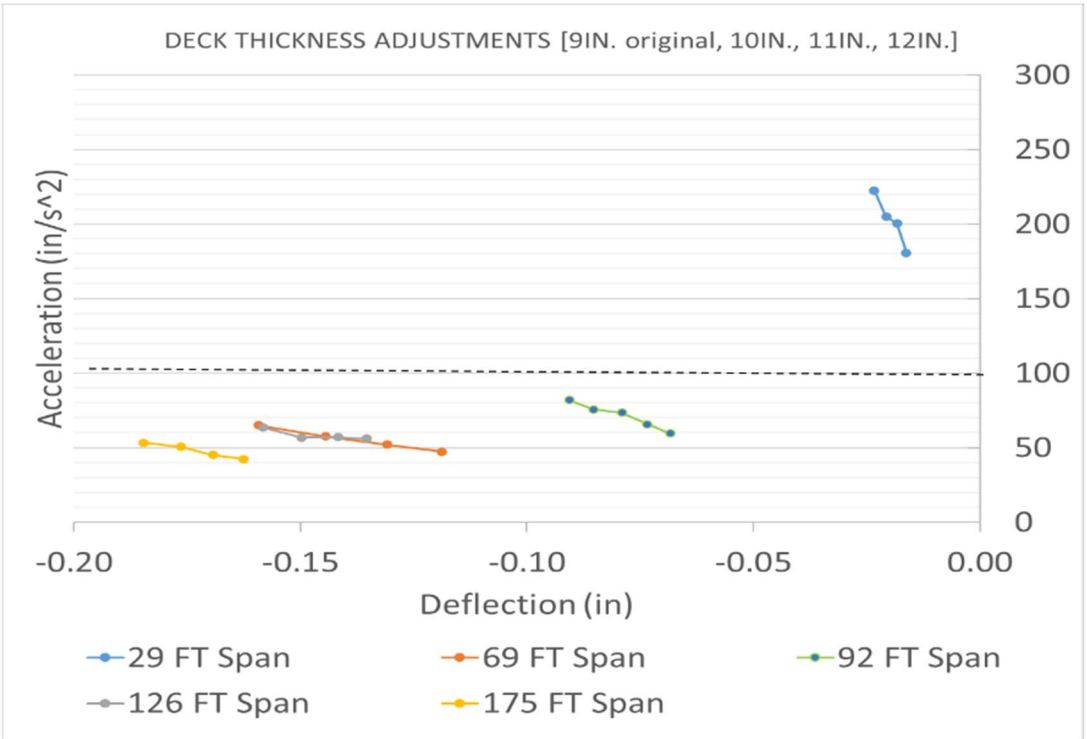

Figure 5.7: Deck Thickness: Deflection vs. Acceleration

5.4 Concrete Deck Density Data

Each bridge was modeled as designed (145 lb. /ft^3 concrete density) and then remodeled by increasing the concrete density by 20 lb. /ft^3 (165 lb./ft^3, 185 lb./ft^3, and 205 lb./ft^3). Increasing the density of the concrete deck had little to no effect on controlling deflection. However, increasing the density of the concrete deck did limit acceleration fairly well, especially for the 29 ft. Span.

Concrete Deck Density (Deflection) Summary

	29 FT Span		69 FT Span		92 FT Span		126 FT Span		175 FT Span	
Concrete Density (lb/ft^3)	Max Deflection (in)	Max Deflection Change	Max Deflection (in)	Max Deflection Change	Max Deflection (in)	Max Deflection Change	Max Deflection (in)	Max Deflection Change	Max Deflection (in)	Max Deflection Change
145 lb/ft^3	-0.023337	-	-0.159295	-	-0.090634	-	-0.158138	-	-0.184660	-
165 lb/ft^3	-0.023337	0.00%	-0.159305	0.01%	-0.083421	-7.96%	-0.160520	1.51%	-0.184461	-0.11%
185 lb/ft^3	-0.023337	0.00%	-0.158846	-0.28%	-0.082225	-9.28%	-0.160529	1.51%	-0.183962	-0.38%
205 lb/ft^3	-0.023337	0.00%	-0.158699	-0.37%	-0.083141	-8.27%	-0.159746	1.02%	-0.182552	-1.14%

Table 5.6: Concrete Deck Density (Deflection) Summary

Concrete Deck Density (Acceleration) Summary

	29 FT Span		69 FT Span		92 FT Span		126 FT Span		175 FT Span	
Concrete Density (lb/ft^3)	Absolute Max Acceleration (in/s^2)	Absolute Max Acceleration Change	Absolute Max Acceleration (in/s^2)	Absolute Max Acceleration Change	Absolute Max Acceleration (in/s^2)	Absolute Max Acceleration Change	Absolute Max Acceleration (in/s^2)	Absolute Max Acceleration Change	Absolute Max Acceleration (in/s^2)	Absolute Max Acceleration Change
145 lb/ft^3	222.594098	-	65.149259	-	82.030154	-	63.529785	-	53.518424	-
165 lb/ft^3	168.183531	-24.44%	61.082531	-6.24%	84.403061	2.89%	60.949163	-4.06%	50.274954	-6.06%
185 lb/ft^3	160.801861	-27.76%	55.678949	-14.54%	74.864978	-8.73%	55.967219	-11.90%	44.450627	-16.94%
205 lb/ft^3	149.837718	-32.69%	52.629418	-19.22%	63.991924	-21.99%	54.309859	-14.51%	41.699937	-22.08%

Table 5.7: Concrete Deck Density (Acceleration) Summary

AVERAGE		
Concrete Density (lb/ft^3)	**Max Deflection Change**	**Absolute Max Acceleration Change**
145 lb/ft^3	-	-
165 lb/ft^3	-1.31%	-7.58%
185 lb/ft^3	-1.69%	-15.98%
205 lb/ft^3	-1.75%	-22.10%

Table 5.8: Concrete Deck Density Average Change Summary

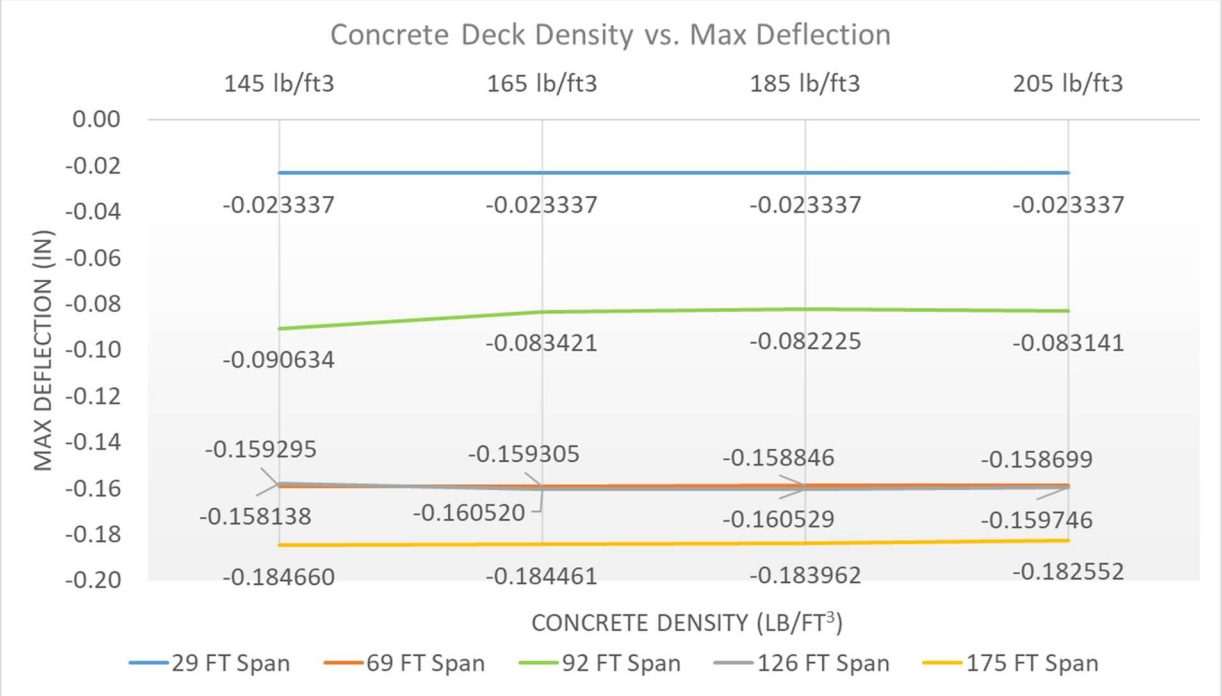

Figure 5.8: Concrete Deck Density vs. Max Deflection

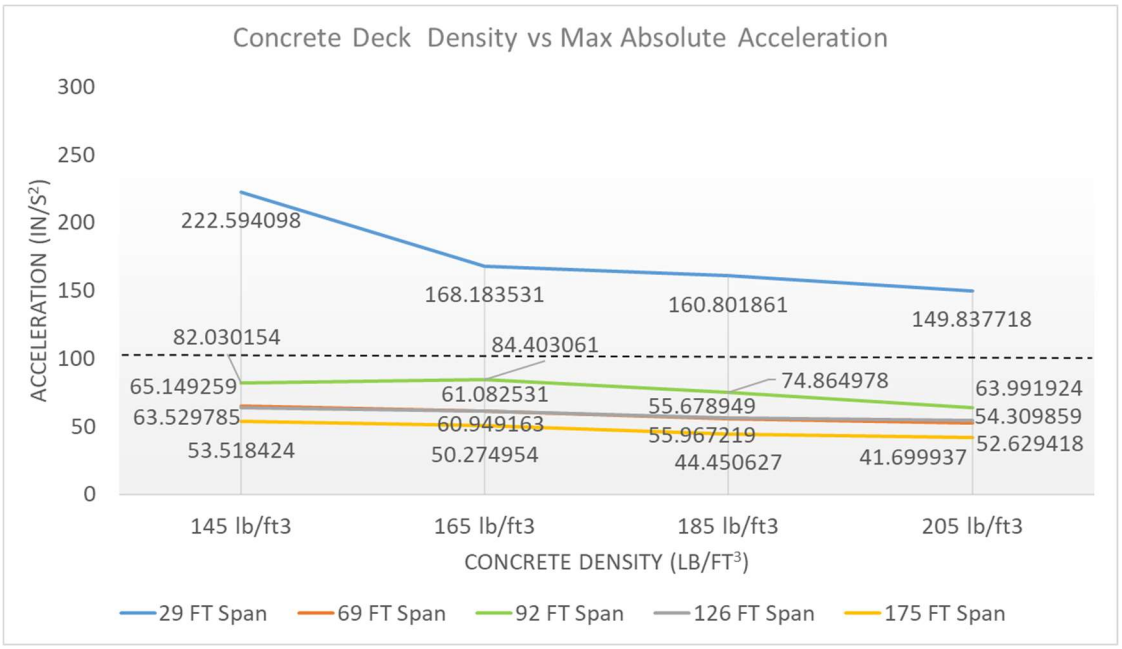

Figure 5.9: Concrete Deck Density vs. Absolute Max Acceleration

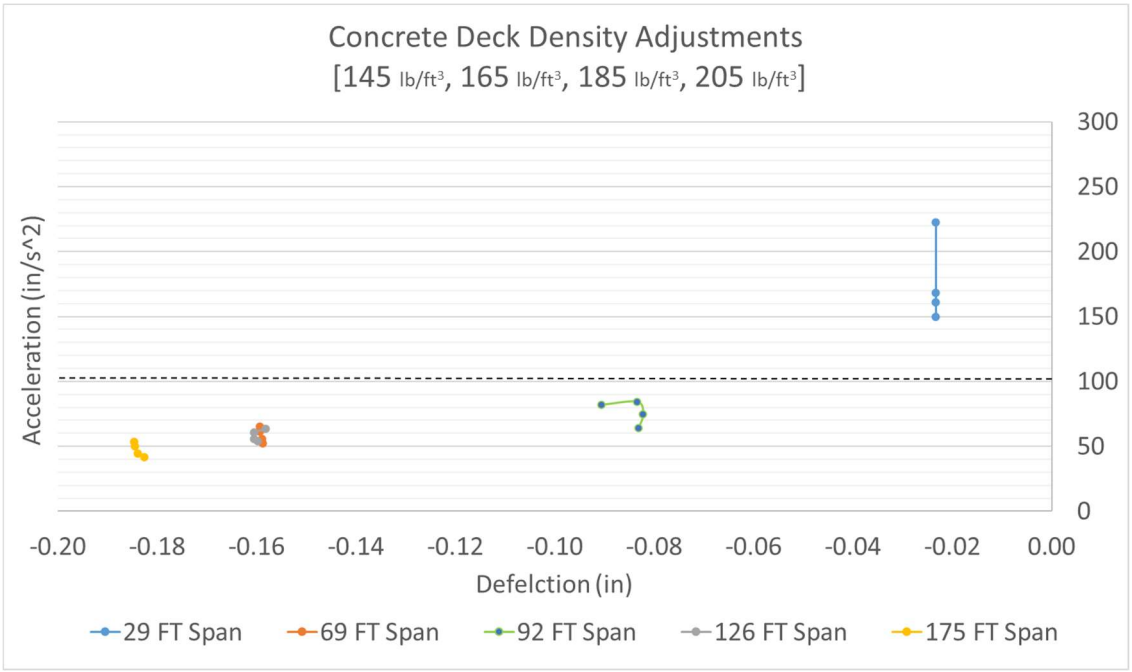

Figure 5.10: Concrete Deck Density: Deflection vs. Acceleration

5.5 Girder Size Data

Each bridge was modeled as designed and then remolded by decreasing and increasing the girder size by increments of 10% (-30%, 20%, -10%, +10%, +20%, and +30%). AASHTO uses the deflection limit L/800 and the span-to-depth ratio limit of 25 to control deflection directly, and indirectly control acceleration. All of the bridges were designed following these guidelines, except the 69 FT, which had a span to depth ratio of 33.81. Increasing the size of the girders limited deflection and acceleration, while decreasing the size of the girders increased deflection and acceleration. When the girders were under-designed deflection seemed to increase at an exponential rate, but seemed to linearly decrease when over-designed. Increasing the size of the greater controlled deflection better than increasing the deck thickness or concrete density. All of the bridges except the 29 ft. Span, was under the acceleration limit 100 in/s^2 even when under-designed by 30%. Furthermore, there was no direct correlation between span length, deflection, and acceleration.

Girder Size (Deflection) Summary

	29 FT Span		69 FT Span		92 FT Span		126 FT Span		175 FT Span	
Girder Size	Max Deflection (in)	Max Deflection Change	Max Deflection (in)	Max Deflection Change	Max Deflection (in)	Max Deflection Change	Max Deflection (in)	Max Deflection Change	Max Deflection (in)	Max Deflection Change
-30%	-0.049438	111.84%	-0.397048	149.25%	-0.296254	247.32%	-0.486420	207.59%	-0.625368	238.66%
-20%	-0.038386	64.49%	-0.279109	75.22%	-0.198305	132.49%	-0.317020	100.47%	-0.388999	110.66%
-10%	-0.029909	28.16%	-0.206798	29.82%	-0.147640	73.09%	-0.242208	53.16%	-0.252726	36.86%
Orignal	-0.023337	-	-0.159295	-	-0.085297	-	-0.158138	-	-0.184660	-
+10%	-0.018781	-19.52%	-0.128726	-19.19%	-0.085556	0.30%	-0.120080	-24.07%	-0.135756	-26.48%
+20%	-0.015270	-34.57%	-0.107878	-32.28%	-0.065828	-22.82%	-0.089574	-43.36%	-0.103115	-44.16%
+30%	-0.012129	-48.03%	-0.090405	-43.25%	-0.054338	-36.30%	-0.076083	-51.89%	-0.081267	-55.99%

Table 5.9: Girder Size (Deflection) Summary

Girder Size (Acceleration) Summary										
	29 FT Span		69 FT Span		92 FT Span		126 FT Span		175 FT Span	
Girder Size	Absolute Max Acceleration (in/s^2)	Absolute Max Acceleration Change	Absolute Max Acceleration (in/s^2)	Absolute Max Acceleration Change	Absolute Max Acceleration (in/s^2)	Absolute Max Acceleration Change	Absolute Max Acceleration (in/s^2)	Absolute Max Acceleration Change	Absolute Max Acceleration (in/s^2)	Absolute Max Acceleration Change
-30%	190.583114	-14.38%	95.883867	47.18%	81.200322	7.04%	65.676407	3.38%	63.888664	19.38%
-20%	175.745269	-21.05%	85.754997	31.63%	87.598496	15.47%	67.158932	5.71%	56.509635	5.59%
-10%	202.084600	-9.21%	70.614945	8.39%	83.052064	9.48%	60.374998	-4.97%	57.873453	8.14%
Orignal	222.594098	-	65.149259	-	75.859845	-	63.529785	-	53.518424	-
+10%	191.265395	-14.07%	68.185410	4.66%	79.403373	4.67%	65.034957	2.37%	43.000209	-19.65%
+20%	266.143306	19.56%	49.708610	-23.70%	62.524630	-17.58%	56.135994	-11.64%	35.312443	-34.02%
+30%	205.154814	-7.83%	56.296330	-13.59%	66.834917	-11.90%	51.878720	-18.34%	29.119502	-45.59%

Table 5.10: Girder Size (Acceleration) Summary

AVERAGE		
Girder Size	Max Deflection Change	Absolute Max Acceleration Change
-30%	190.93%	12.52%
-20%	96.66%	7.47%
-10%	44.22%	2.37%
Original	-	-
+10%	-17.79%	-4.41%
+20%	-35.44%	-13.47%
+30%	-47.09%	-19.45%

Table 5.11: Girder Size Average Change Summary

Span-to-Depth Ratios							
Bridges	-30%	-20%	-10%	Design	10%	20%	30%
29 FT Span	23.56	20.62	18.33	16.49	14.99	13.74	12.69
69 FT Span	48.30	42.27	37.57	33.81	30.74	28.18	26.01
92 FT Span	30.92	27.06	24.05	21.65	19.68	18.04	16.65
126 FT Span	32.73	28.64	25.45	22.91	20.83	19.09	17.62
175 FT Span	33.71	29.49	26.22	23.60	21.45	19.66	18.15

Table 5.12: Girder Size: Span-to-Depth Ratios

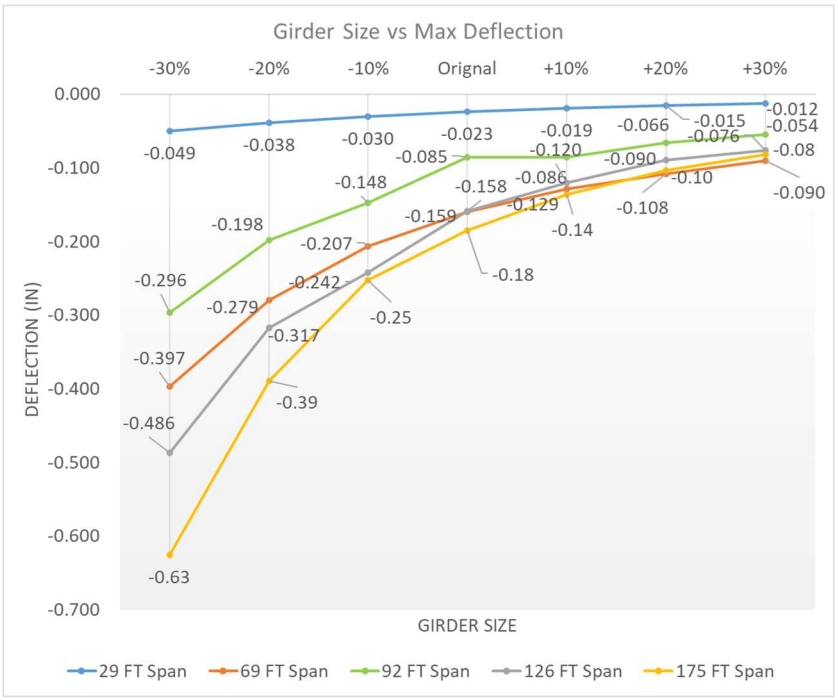

Figure 5.11: Girder Size vs. Max Deflection

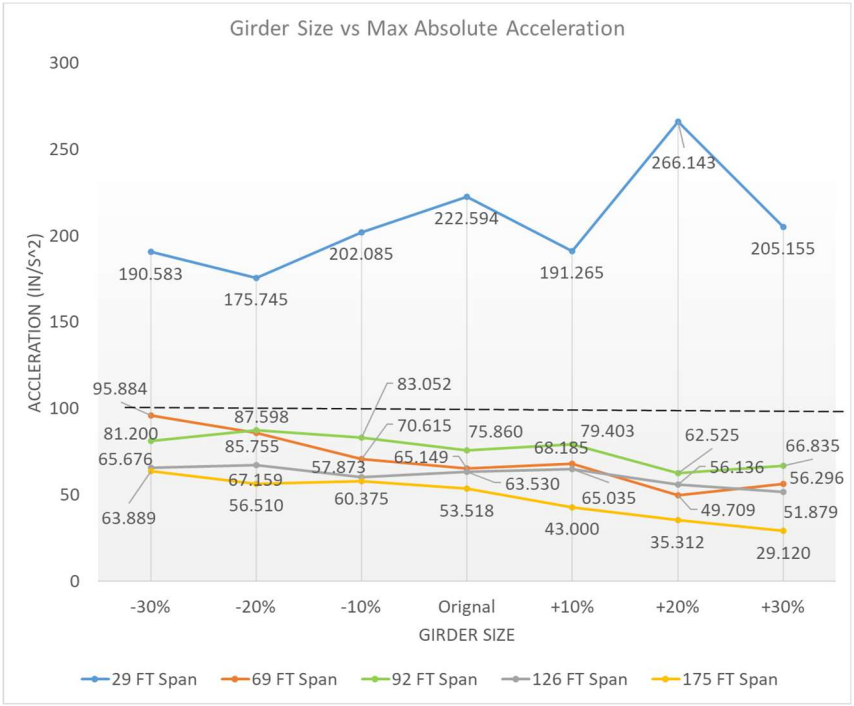

Figure 5.12: Girder Size vs. Absolute Max Acceleration

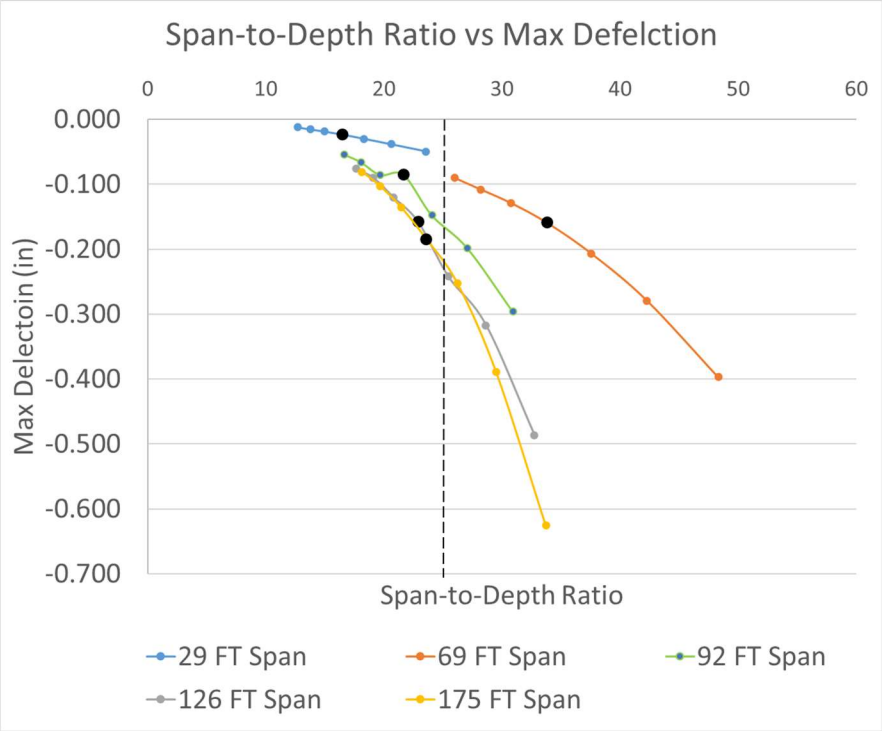

Figure 5.13: Span-to-Depth Ratio vs. Max Deflection

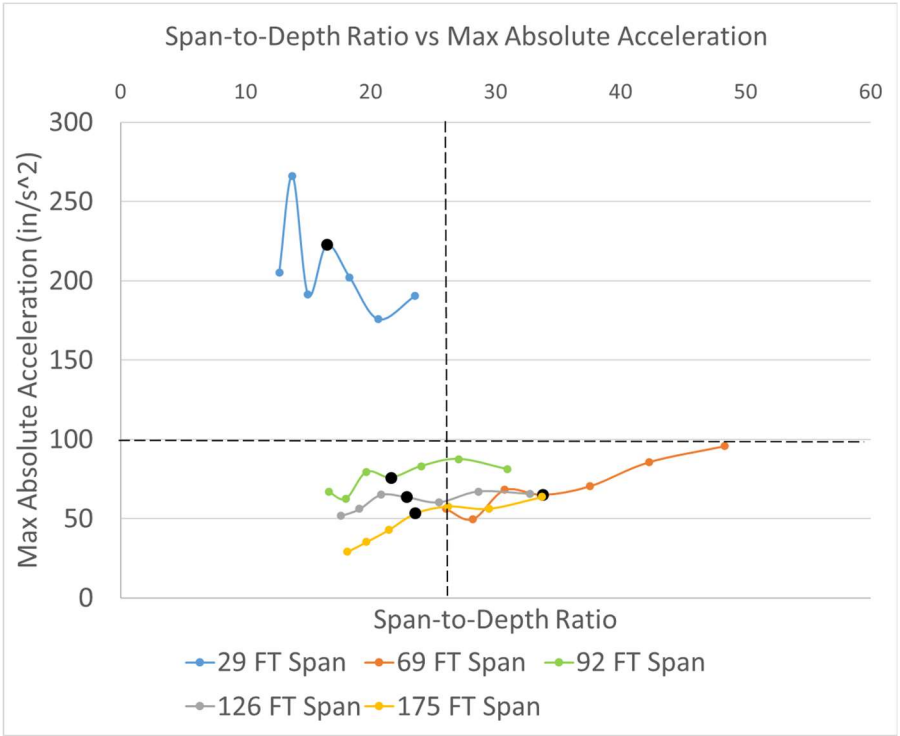

Figure 5.14: Span-to-Depth Ratio vs. Absolute Max Acceleration

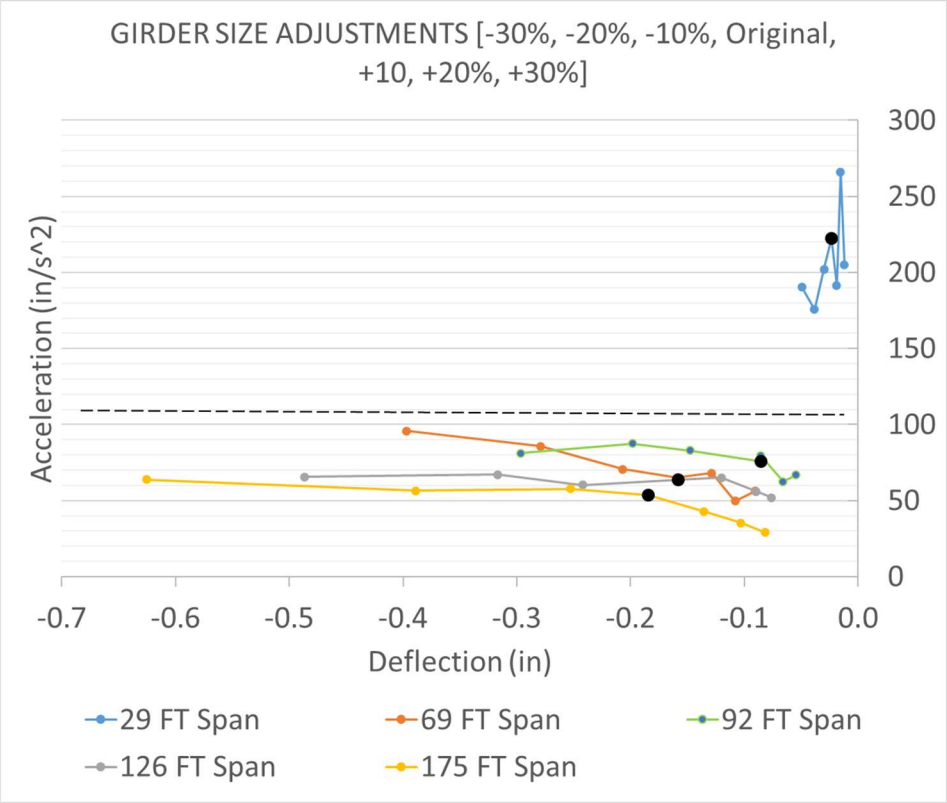

Figure 5.15: Girder Size: Deflection vs. Acceleration

CHAPTER 6. CONCLUSIONS AND RECOMMENDATIONS

6.1 Summary

The objective of this research was to investigate the relationship between deflection and acceleration for existing simply supported slab-on-girder bridges. Measured field data for one of the bridges was used to calibrate the bridge-road-vehicle model used in the grillage analysis. The girder spacings, span lengths, roadway widths, road roughness profiles, and vehicle models remained constant throughout the grillage analysis. Deck thickness, the density of the concrete deck, and girder sizes were adjusted. This analysis highlighted the relationship between deflection and acceleration under different conditions without interfering with the deflection limit L/800. The computed deflection and acceleration values were then compared with AASHTO's current deflection limit and span-to-depth ratio.

6.2 Conclusions

1. Simple-span steel bridges can be molded as a 3-D grillage system with accurate results.
2. Increasing the deck's concrete density, deck thickness, or girder size will limit acceleration.
3. Increasing the girder size by 10% is more effective at limiting deflection than adding an extra inch of the deck or increasing the concrete's density by 20 lb. /ft^3.
4. Increasing the deck's concrete density had virtually no effect on the deflection.
5. Extremely high acceleration coupled with extremely low deflection does not result in "unpleasant" vibrations.
6. As designed, all of the bridges were under 100 in/s^2, except the 29 ft. Span, but this bridge had undetectable vibrations due to its extremely low deflection.
7. Geographical location and ADT/ADTT should be considered when limiting acceleration.
8. AASHTO's deflection limit (L/800) and span-to-depth ratio limit (25) do seem to limit bridge vibrations indirectly. However, there was no strong correlation between span length and acceleration, meaning other design parameters are probably indirectly limiting acceleration as well.

6.3 Recommendations

1. Natural frequencies should be captured.
2. Calculate L/800 deflection values using AASHTO's criteria for each simulation.
3. Individual road roughness profiles should be incorporated.
4. Site-specific WIM data should be captured to prioritize the importance of vibration control.

REFERENCES

1. AASHTO, “Standard Specifications for Highway Bridges.” American Association State Highway and Transportation Officials, Washington, D.C.,2012.

2. AASHTO (1996). Load factor design: Bridge design specifications, 16th ed., American Association of State Highway and Transportation Officials, Washington, D.C.

3. AASHTO (2014). Load resistance and factor design: Bridge design specifications, 7th ed., American Association of State Highway and Transportation Officials, Washington, D.C.

4. Austroads (1996). Australian bridge design code, Austroads, Haymarket, NSW, Australia. Barker, M. G., and Barth, K. E. (2013). “Improved serviceability criteria for steel girder bridges.” J. Bridge Eng., Vol. 18, No. 7, pp. 673-677, DOI: 10.1061/(ASCE)BE.1943-5592.0000402.

5. Adams, R, “Comparison of Deflection and Vibration Limits for High-Performance Steel Bridges.” MS Dissertation, Graduate Program in Civil and Environmental Engineering, Rutgers University, 2013

6. Billing, J. R., and Green, R. (1984). Design provisions for dynamic loading of highway bridges, Transportation Research
7. Record 950. British Standard BS 5400-2 (2006). Steel, concrete and composite Bridges, Part-2: Specification for Loads.

8. Camara, A., Nguyen, K., Ruiz-Teran, A. M., and Stafford, P. J. (2014). “Serviceability limit state of vibrations in under-deck cable-stayed bridges accounting for vehicle-structure interaction.” Engineering Structures, Vol. 61, pp. 61-72, DOI: 10.1016/j.engstruct.2013.12.030.

9. Camara, A., and Ruiz-Teran, A. M. (2015). “Multi-mode traffic-induced vibrations in composite ladder-deck bridges under heavy moving vehicles.” Journal of Sound and Vibration, Vol. 355, pp. 264-283, DOI: 10.1016/j.jsv.2015.06.026.

10. Cantieni, R. (1983). Dynamic load tests on highway bridges in Switzerland, Report 211, Section Concrete Structures and Components, EMPA, CH-8600 Dubendorf, Switzerland.

11. CSA (1990). CSA. S6- 88 and commentary, Design of Highway Bridges, Canadian Standards Association, Rexdale, Ontario, Canada.

12. Darjani, S., Saadeghvaziri, M. A., and Aboobaker, N. (2010). “Serviceability considerations of high-performance steel bridges.” Structures Congress, ASCE, DOX: 10.1061/41130(369)69.

13. Fountain, R. S., and Thunman, C. E. (1987). “Deflection criteria for steel highway bridges.” Proceedings of the AISC National Engineering Conference in New Orleans.

14. Fuhrman, D. M., Rafiee-Dehkharghani, R., Lopez, M. M., Aref, A., and O’Connor, J. (2014). “Field performance of a new fiber-reinforced polymer deck.” Journal of Performance of Constructed Facilities, DOI: 10.1061/(ASCE)CF.1943-5509.0000656.

15. Gaunt, J. T., and Sutton, C. D. (1981). Highway bridge vibration studies, Joint Highway Research Project (Report No. JHRP–81-11), Purdue University & Indiana State Highway Commission.

16. Goldman, D. E. (1948). A review of subjective responses to vibratory motion of the human body in the frequency range 1 to 70 cycles per second, Naval Medical Research Institute National, Naval Medical Center. Bethesda, Maryland.

17. Hwang, E.-S. (1990). Dynamic loads for girder bridges, Thesis presented to the University of Michigan, Ann Arbor, Mich., in partial fulfillment of the requirements for the degree of Doctor of Philosophy.

18. Irwin, A. (1978). “Human response to dynamic motion of structures.” Structural Engineers, Vol. 56A, No. 9, pp. 237-44.

19. ISO 2631 (1997). Mechanical vibration and shock - Evaluation of human exposure to whole-body vibration. Part 1 General requirements, International Standard ISO-2631/1, Geneva, Switzerland.

20. Janeway, R. N. (1948). “Vehicle vibration limits to fit the passenger.” SAE Technical Paper 480061, SAE, New York, NY, DOI: 10.4271/480061.

21. Le, H. X., & Hwang, E. (2016). Investigation of deflection and vibration criteria for road bridges. KSCE Journal of Civil Engineering, 21(3), 829-837. https://doi.org/10.1007/s12205-016-0532-3

22. Lenzen, K. H. (1966). Vibration of steel joist-concrete slab floors, J. Am. Instit. Steel Construct. Eng., Vol. 3, No. 3, pp. 133-136.

23. Liu, M., “A Three-Dimensional Dynamic Model For Bridge-Road-Vehicle System.” MS Dissertation, Department of Civil and Environmental Engineering, Bradley University, 1996.

24. Mallock, H. R. A. (1902). Vibrations produced by the working of traffic on the central London railway, Board of Trade Report, Command Papers, n. 951.

25. MLTM (2010). Korean highway bridge design code, Korea Ministry of Land, Transportation and Maritime Affairs, Seoul, Korea.

26. Nassif, H., Liu, M., Su, D., and Gindy, M. (2011). “Vibration versus deflection control for High-performance Steel (HPS) girder bridges.” Transportation Research Record, No. 2251, pp. 24-33, DOI: 10.3141/2251-03.

27. Nassif, Hani H, and Ming Liu. “Analytical Modeling of Bridge-Road-Vehicle Dynamic Interaction System.” *Journal of Vibration and Control*, vol. 10, no. 2, 2004, pp. 215–241., doi:10.1177/1077546304033950.

28. Nguyen, Q. H. (2013). Dynamic interaction between trucks and bridges considering road roughness, Thesis presented to Kyung Hee University, in partial fulfillment of the requirements for the degree of master.

29. Oehler, L. T. (1970). Bridge vibration – summary of questionnaire to state highway departments, Highway Research Circular, Highway Research Board (No. 107).

30. Reiher, H. and Meister, F. J. (1931). “The effect of vibration on people.” Forschung im Ingenieurwesen, Vol. 2, No. II, pp. 381-386, DOI: 10.1007/BF02578773.

31. Roeder, C. W., Barth, K. B., and Bergman, A. (2002). Improved live load deflection criteria for steel bridges, Final Report NCHRP 20- 07/133, University of Washington, Seattle, WA.

32. Ruiz-Teran, A. M., and Aparicio, A. C. (2009). “Verification criteria of the SLS of vibrations for road bridges with slender prestressed concrete decks.” In International FIB Symposium, London (UK).

33. Wei, J., and Chen, B. (2007). “Estimation of dynamic response for highway CFST arch Bridges.” 5th International Conference on Arch Bridges, Madeira, Portugal.

34. Wright, D. T., and Green, R. (1964). Highway bridge vibration. Part II: Report No. 5 Ontario test programmed, Ontario Department of Highways and Queen’s University, Kingston, Ontario.

35. Wright, R. N., and Walker, W. H. (1971). Criteria for the deflection of steel bridges, Bulletin for the American Iron and Steel Institute, No. 19.

36. Wu, H. (2003). Influence of live-load deflections on superstructure performance of slab on steel stringer bridges, Ph.D. Dissertation, Department of Civil and Environmental Engineering, West Virginia University.